Doctoral Thesis

STABILITY ANALYSIS AND DEFORMATION CONTROL MEASURES OF UNDERGROUND STRUCTURES IN COMPLEX GEOLOGICAL CONDITIONS

複雑な地質条件における地下構造物の変形解析と対策工法に関する研究

March 2017

Graduate School of Science and Technology
Nagasaki University

Xiaoshan Wang

Acknowledgements

This thesis could not have been complete without the support of the kind people who have helped and encouraged me to accomplish my research.

First and foremost, I would like to express my deepest gratitude to my supervisor, Prof. **Yujiang Jiang**, who guided me throughout my writing of this thesis in Nagasaki University. He carefully read the whole draft and offered painstaking and precious criticism. His standards of academic excellence have made my revision and exciting and gratifying experience. I gratefully acknowledge my committee members, Prof. **Akihide Tada** and Prof. **Kiyoshi Omine**, for their valuable comments and suggestions to refine this thesis.

I am very thankful to Prof. **Shucai Li**, Prof. **Guangyue Wang**, Prof. **Shuchen Li**, Prof. **Jian Liu** and other professors in Shandong University, China, for their fundamental assistance and guidance in getting my postgraduate study. Also, I would like to express my sincere gratitude to Prof. **Bo Li** in Shaoxing University, China, who gave the good advice, support and encouragement on both academic and personal matters. I am also grateful to the Assistant Prof. **Satoshi Sugimoto** in the Geo-environmental Laboratory for his kind supports and help during my study and life in Japan.

I would like to thank all my friends in Nagasaki for their supports and encouragement during my study in Japan. My grateful thanks should be given to Dr. **Lei Yang**, Dr. **Yang Gao**, Dr. **Kangming Chen**, Dr. **Sha Lou**, Dr. **Richeng Liu**, Dr. **Yukihiro Higashi**, Dr. **Xiao Shi**, Dr. **Xuezhen Wu**, Dr. **Jianhua Wang**, Dr. **Qu Wang**, Dr. **Santos Chicas**, Dr. **Na Huang**, Dr. **Chen Wang**, Dr. **Xuepeng Zhang**, Miss. **Didi Wang**, Dr. **Junpei Ishida**, Mr. **Hao Huang**, Miss. **Ying Li**, Mr. **Han Xia**, Mr. **Kai Liu**, Miss. **Xuening Guo**, Dr. **Jian Zheng** and all others who helped make my stay in Japan a very pleasant one.

Finally, I am deeply grateful to my parents and my husband **Kongqin Yu** for their exceptional moral support on my study and I would like to thank my sisters for encouraging my study. I am grateful to all my families, whose exceptional support and understanding during my thesis work have been made me to complete the thesis successfully.

Xiaoshan Wang

Nagasaki October 2016

Abstract

Understanding the mechanical deformation behaviors of rock masses in complex geological conditions is important for the development and utilization of the deep underground engineering such as radioactive waste disposal facilities, power plants and petroleum reservoirs. The deformation and failure behaviors of underground structures are generally governed by the mechanical behaviors of surround rock masses. Soft rock masses and jointed rock masses are the two typical rocks that generally encountered in deep engineering. For tunnels constructed in those rocks, cracking and squeezing of host rock masses may occur caused by the excavation disturbance. On the other hand, for tunnels in operation, cracking and spalling of concrete lining may be induced by the acting of loosening pressure on lining concrete, especially for those degraded tunnel or under seismic loads. Hereby, this dissertation mainly investigates the stability of underground structures and the corresponding deformation control measures in complex geological conditions in construction and operation.

First of all, base friction tests were conducted to investigate the influence of dip angle of layered joints on the stability of circular openings in jointed rock masses and a series of numerical simulations utilizing an originally developed code based on distinct element method (DEM) were performed on the experiment-based and extended numerical models, respectively. The results show that the main propagation direction of newly generated cracks is approximately perpendicular to the joint dip angle. For the brittle host rock masses, the deformation around the underground openings is governed by the tensile failure of host rock masses. A decrease in joint dip angle gives rise to an increase of plastic failure zone in the host rock masses. The models with lower joint dip angles could generate a larger number of cracks. The maximum displacement observed at the left shoulder of openings is approximately 1.8 ~ 2 times of the minimum displacement at the right side wall of circular opening. The influences of the opening shape on the main propagation direction of newly generated cracks could be negligible. Due to the stress concentration at the sharp corner of square openings, a larger area of plastic zones is developed, which leads to obvious increment of displacements around the underground openings.

Secondly, a case study of the west section (WS) of Tawarazaka Tunnel was performed to investigate the mechanism of ground squeezing in soft jointed rock masses. The squeezing characteristics in the west section (WS) of Tawarazaka tunnel were discussed and the systematic analysis of the measurement convergences during tunneling was presented. Numerical modelling corresponding to the tunnel profile in the WS based on the finite difference method (FDM) was performed to investigate the main factors caused ground squeezing. The reasonable parameters which can well

reproduce the ground conditions in the WS were determined based on comparing the numerical analysis results with the in situ measurement convergences. The results showed that ground squeezing is prone to occurring in the WS, which mainly composed of Neogene mudstone, and the horizontal stress ratio K_0 was defined as a squeezing index in this section. It was also shown that the weak rocks with strongly developed slickenside also plays an important role in ground squeezing of WS. The results also revealed that the ground squeezing in the WS is mainly caused by the modulus of rocks, and the properties of bedding joints only have minor effect on the squeezing in this tunnel. Overburden has also a significant effect on the squeezing behaviors, and the convergence ratio λ tends to be stable once a limiting overburden of 100 m was exceeded.

Moreover, for tunnels in operation in complex geological conditions, the reinforcing effect of FRP grids embedded in Polymer Cement Mortar (PCM) shotcrete (FRP-PCM method) on tunnel linings surrounded by soft rocks were estimated, taking into accounts the loosening pressure acting on lining concrete. Laboratory direct shear test and bending test were carried out on the specimens reinforced with various grades of FRP grids to obtain the mechanical properties of bonding surfaces between PCM and concrete reinforced by FRP grids. The bending test results showed that the bearing capacity of reinforced beam by FRP grids subjected to bending loads was improved by around 40%. Numerical modeling of reinforced tunnels by FRP-PCM method was performed using the properties obtained from these laboratory tests to investigate the reinforcing performance of FRP-PCM method on degraded tunnel linings. Numerical models with different loosening pressures acting on tunnel lining, ground classes, lining deterioration degrees, and tunnel health degrees were considered and applicable conditions under which the application of FRP-PCM method could effectively reinforce tunnel linings were proposed.

The reinforcing effects of FRP-PCM method on lining concrete under seismic loads were also discussed. Numerical modelling based on the FEM method was performed to analyze the reinforcing effects of FRP-PCM method, quantitively, taking into accounts the influences of ground types, cavity positions and construction methods of tunnels, and those simulation results could provide valuable guidance for the reinforcing of underground structures.

Keywords: complex geological conditions, soft rock masses, jointed rock masses, deformation, based friction test, direct shear test, bending test, distinct element method, finite difference method, numerical modelling, degraded tunnel lining, seismic load

Contents

CHAPTER 1

Introduction

1.1 Research background and objectives

With the development of engineering constructions such as transportation, water conservancy and hydroelectric power, energy, etc., human activity space is increasingly expanded to the underground part of the globe where numerous underground engineering are involved. A large number of underground tunnels are being or have been constructed in these few decades. Deformation problem of rocks in complex geological conditions such as fractured rock masses or soft rock masses, has always been a threat to engineering safety for tunnels in construction and operation, especially when the tunnel crossing the high ground stress area, fault fracture zone, the problem is more prominent. In tunneling and mining operations, external loads and excavation disturbance could trigger the crack initiation, propagation and coalescence of microcracks in host rock masses, which may impact the mechanical behavior of rock masses, thereby affecting the long-term safety of underground structures (Cai et al., 1998; Cai et al., 2004; Martino et al., 2004; Wang et al., 2009). Besides, soft rocks have the basic engineering properties such as low uniaxial compressive strength, water softening, easy deformation and disturbance and etc., which seriously affect the tunnel construction and operation. These characteristics can lead to yielding, slabbing, raveling, and squeezing conditions. Another key factor is that the strength of many soft rocks formations is not constant and they may deteriorate when exposed in a tunnel.

In view of the above reason, the domestic and foreign scholars conducted a series of problems study to the complex geological formations, and a number of deformation control methods in both tunnel construction and operation have been proposed and used in practices.

To improve the understanding of deformation and failure mechanisms of host rock masses during excavation is essential in tunnel engineering. Timoshenko and Goodier (1951) investigated the distributions of radial, tangential and shear stresses at the boundary of underground opening subjected to biaxial stress conditions. Depending on the various lateral pressure coefficients, typical stress distributions around the circular and elliptical underground opening in homogeneous rock masses were deduced. Goodman and Shi (1985) proposed a blocky theory to evaluate the deformation of rock masses around underground openings. In the blocky theory, removability analysis was conducted on the rock blocks based on a precise characterization of discontinuities, underground opening shape, and width of underground opening. Laboratory test is an essential method to evaluate the deformation and failure processes caused by

excavation. Kulatilake et al. (2001) conducted the uniaxial compression tests on the artificial rock-like material with a circular opening in jointed rock masses, and classified the failure mode into three types as tensile failure, shear failure and mixed type failure. Sagong et al. (2011) also conducted a biaxial compression test in jointed rock masses with the joint dip angle of 30°, 45° and 60° to evaluate the deformation and failure around the underground opening, and found that propagation direction of tensile cracks is normal to the joint angle and the model with lower joint angle generates a larger number of tensile cracks. Several numerical studies have also been contributed to investigating the deformation and failure behaviors of an underground opening during excavation. Two of the most commonly adopted methods are continuum-based and discontinuum-based methods (Jing and Hudson, 2002). Among the continuum-based methods, the finite difference method (FDM) that uses a differential form of the governing partial differential equations is commonly utilized to investigate the deformation of rock masses during the excavation of underground openings (Lisjak et al., 2014). In this method, the joint elements were integrated into the continuum formation, and the calculation precision was seriously restricted by the increment of joint numbers (Hammah et al., 2008). The realistic failure process analysis (RFPA) code based on the finite element method (FEM) is commonly used to reproduce the failure process and investigate the deformation of quasi-brittle materials such as rock masses (Tang, 1997; Tang et al., 1998, 2000a, 2000b). The Young's modulus and uniaxial compressive strength were conformed to a Weibull distribution to characterize the nonlinear behaviors of deformation and failure of rock masses (Zhu, 2005). The RFPA code was applied to evaluate the deformation and failure process of rock masses around various types of underground openings, and it was found that the development of primary tensile cracks was governed by the lateral pressure coefficient (Zhu, 2005). Wang et al. (2009) also utilized this modeling technique to confirm the effects of anisotropy and heterogeneity on the deformation of rock masses around underground openings and found that the fracture initiation and propagation in rock masses are triggered by a combination of the weak plane and stress concentration caused by the transverse anisotropy. One of the most commonly used discontinuum-based approach is the discrete element method (DEM), in which the materials such as rock masses are treated as an assemblage of independent rigid or deformable blocks, or particles with certain particle friction and bond strength to reproduce the strength of intact and/or jointed rock masses (Cundall et al., 1992). Hao and Azzam (2005) investigated the plastic zone and deformation around underground opening in rock masses containing a fault utilizing the DEM, and found that the physical parameters of fault play an important role on the deformation of host rock masses. Solak (2009) performed a parametric study based on the DEM, taking into accounts various joint characteristics and in situ stresses to investigate the deformation behaviors of host rock masses around a circular opening, and a delimiting criteria to classify the ground behavior was established. Jiang et al. (2006) discussed the deformation behavior of rock masses around an underground opening from a fractal dimension perspective, and found that

the deformation increases with the increment of fractal dimension of rock joint distributions. An expanded distinct element method (EDEM) was later developed by Jiang et al. (2009) to investigate the cracking procedure in jointed rock masses, and it was found that the number of newly generated cracks increases with the increment of depth of underground opening and initial ground stress. The generation of new cracks in a few weak zones is significantly influenced by the positions of existing rock joints. Sagong et al. (2011) conducted numerical analysis based on particle flow code (PFC) to investigate the fracture and sliding behaviors of jointed rock masses around a circular opening, and found that the damage zones increase with the decrease of joint dip angle. A hybrid finite discrete element method (FDEM) code was developed by Lishjak et al. (2014) to simulate the fracturing and deformation process during tunnel excavation in brittle rock masses, which provided an explicit consideration of crack initiation, propagation and coalescence.

During the tunnel excavation, ground squeezing is generally encountered, especially for tunnels through soft rock masses or bedding jointed rock masses. Once the ground squeezing occurred, delay of the project and extra costs due to the remedial actions may be triggered. Therefore, understanding the squeezing characteristics of ground is a crucial engineering issue for the design and excavation of tunnels. Saari (1982) suggested using the intensity of the tangential strain of tunnel as a parameter to evaluate the squeezing degree of ground and proposed closed form solutions for some special cases by considering the squeezing phenomenon as an elasto-visco-plastic behavior of rocks. Tanimoto (1984) considered the ground as an elasto-plastic material following the strain-softening constitutive law to evaluate the degree of squeezing of rocks, and suggested that squeezing would occur when the rock is strained to its residual flow state. Aydan et al. (1993) took into account the experience gained in squeezing rocks of Japan, and found that squeezing occurs if the competence factor, which is the ratio of uniaxial compressive strength of intact rock to the overburden pressure, is less than 2.0. Kovári et al. (1996) suggested that low strength and high deformability of rocks as well as the presence of pore pressure of water could facilitate squeezing of ground, and found that the following rock types are specially prone to developing large pressures and deformations: altered gneiss, shale, phyllite, schist, clay, mudstone and tuff. Hoek et al. (2002a, b) proposed a semi-analytical method to estimate the potential tunnel squeezing and suggested that the ratio of rock mass uniaxial compressive strength to the in situ stress could be used as an indicator of tunnel ground squeezing. Hamidi et al. (2008) assessed the maximum radial displacement in determining the squeezing characteristics of the ground in Nasoud tunnel by utilizing the two-dimensional code of Fast Lagrangian Analysis of Continua (FLAC), and proposed some preventive measures to mitigate the potential of squeezing problems. Hoek et al. (2009) presented the case history of Yacambu´-Quibor tunnel that encountered severe squeezing problems during the construction to illustrate different mechanisms of the failure of support system, and found that these mechanisms are related to the sequence of installation of different support components. Barla (2009) discussed the recent

innovations in yield–control support systems applied to conventional tunneling in difficult ground conditions associated with squeezing, and some measures that have been applied to deal with the squeezing conditions encountered during the excavation in the Carboniferous formation were studied based on the case study of Saint Martin access adit along the Base Tunnel of the Lyon–Turin railway link. Jimenez et al. (2011) proposed a novel empirical method for predicting the squeezing characteristics in rock tunnels based on the application of the theory of linear classifiers to an extensive database of well-documented squeezing case histories from tunnels in the Himalayas and Himalayan foothills. This method allowed to calculate probabilities of squeezing for different combinations of tunnel depth and rock mass quality, and the analysis results showed that the probability of squeezing significantly increases with depth and is mainly effected by the quality of rock mass. Bilgin et al. (2012) studied the squeezing characteristics of ground in the Uluabat Tunnel based on the detailed Tunnel Boring Machine (TBM) performance analysis, and found that overburden, rock mass rating (RMR) values, the increase of machine thrust for a given tunnel length and time, the variation in the torque/thrust ratio could be utilized as a reliable basis to alert the practicing engineers to implement some mitigating measurements. Mezger et al. (2013) suggested that the frequently observed phenomenon of squeezing variability can be tracked back to different degrees of shearing, different schistosity orientations and the influence of nearby weaker or stronger zones. A simple empirical equation that can map the effect of shearing and schistosity reasonably well and provide reliable indications of squeezing intensity was also proposed.

Not only for tunnels in construction but also for the ones in operation were greatly affected by the complex geological conditions. Deformations or damages such as cracking and spalling occur frequently on tunnel linings, which caused by the degradation of concrete lining or external loads (e.g. earthquake, earth pressure and freezing pressure). Repairing and reinforcing existing tunnels have become a major part of civil engineering. Various types of methods have been developed to improve the integrity of lining concrete, typical ones of which are grouting reinforcement method, fiber reinforced shotcrete (FRS) method (De la Fuente et al., 2012; Chiaia et al., 2009; Chryssanthakis et al., 1997; Jeng et al., 2002; Franzén, 1992), carbon fiber sheet (CFS) method (Lee et al., 2002; Miyauch, 1997), steel board method (Kiriyama et al., 2005), and Fiber reinforcement plastic (FRP) method (Erki et al., 1993; Hensher, 2013; Asakura et al, 2003; Clarke et al., 1996). Comparing to other methods, FRP grids have several favorable properties such as high tensile strength, low weight, easy handling and application, immunity to corrosion, and minimal occupancy of space (Lau and Pam, 2010; Bournas et al., 2015). Past research has indicated that FRP grids bonded to the tensile side of flexural members can help increase the flexural capacity of reinforced concrete (RC) structures (Hensher, 2013). Therefore, in the past a few decades, FRP as a strengthening material for concrete structures has been increasingly utilized in engineering practices. To fully explore the potential of FRP reinforcement, the reinforcing effect of FRP grids has been extensively investigated. Chen et al. (2003)

and Yao et al. (2005) conducted single shear pull tests and used an anchorage strength model to estimate the effective bond length between FRP and concrete. Täljsten (1997) conducted double shear pull test on FRP reinforced concrete and the results showed that the strain limit of the concrete is the governing factor for the debonding failure. Pešić et al. (2003) predicted the load level at which FRP-plated concrete beams fail due to plate-end debonding based on finite element analysis. They found that the extent of strengthening is limited by the shear capacity of concrete beams. Investigations on flexural capacity of reinforced concrete by FRP have also been reported in literature. Toutanji et al. (2006) developed a moment deflection model to evaluate the load carrying capacity of RC beams. Several other studies showed that the beams strengthened by FRP would avoid the debonding failure when a carefully designed anchorage is applied, resulting in a good flexural performance in terms of strength and ductility (Ceroni, 2010; Esfahani et al., 2007; Chajes et al., 1994; Wang et al., 2006). Arduini et al. (1997) and Buyukozturk (1998) numerically studied the load-deflection behaviors as well as the failure mechanism from ductile to brittle of pre-cracked RC beams. Berg et al. (2006) and Nystrom et al. (2003) focused on the FRP reinforcement on concrete structures from the cost-effective perspective. It was reported that FRP reinforcements could be cost-effective, given the savings in construction time and their potential long-term durability and maintenance benefits in the engineering fields such as bridge decks.

1.2 Thesis structure

With the research background given above, the overall objects of this thesis is to analyze the deformation and stability of underground structures in complex geological conditions, such as soft rocks and jointed rock masses, and the corresponding method to control the deformations of underground structures was also proposed. The outline of this thesis is shown in Fig. 1.1.

Chapter 1 gives an introduction of the research background, the research objectives and contents as well as the structure arrangement of this thesis. Chapter 2 provides a general description of the principal concepts, deformations of underground structures that commonly encountered and the corresponding methods to control these deformations. These contents were used in or have close relations with the studies in the following chapters. In Chapter 3, the experimental and numerical researches on the crack propagation and deformation around underground structures are presented. The base friction tests were conducted to investigate the influences of joint dip angle on the stability of underground openings in highly jointed rock masses. A series of numerical simulations using the originally developed DEM code were performed based on the experiment-based and extended numerical models to investigate the influences of joint spacing, underground opening shape on the deformation of surrounding rocks. These results might provide valuable guidance for the constructions of underground openings in jointed rock masses. In chapter 4, a case study of the west section (WS) of

Tawarazaka Tunnel in Japan was performed to investigate the main factors that may have significant influences on the convergence of tunnel in soft bedding jointed rock masses. These factors can be selected as the indicators during tunnel construction in squeezing ground. The concise overview of the available data taking into accounts the geological condition, excavation and support methods was introduced. The correlations between the in situ measured convergences and the geological characteristics such as overburden, apparent young's modulus, and initial horizontal stress ratio and rock quantities were also discussed. A two-dimensional numerical analysis based on the geological distribution was performed to investigate the main factors inducing the squeezing of ground in the WS, and the effects of bedding joint properties, modulus of rocks and overburden H on tunnel deformations were quantitatively analysed. In chapter 5, an FRP-PCM method was proposed and its applicable condition on deformed tunnels caused by tunnel lining degradation was estimated experimentally and numerically. First, direct shear tests were performed to determine the mechanical properties of the interface between PCM and concrete, bonded with an FRP layer. Then two-point bending tests and their numerical simulations were conducted to investigate the effects of FRP-PCM method on the bearing capacity of concrete beams. At last, numerical simulations based on Finite Difference Method (FDM) were performed to systematically analyze the reinforcing effects of FRP-PCM method on degraded tunnel linings, taking into account the influences of ground class, loosening pressure, concrete strength, and deterioration degree of lining concrete. Favorable conditions of applying FRP-PCM method to degraded tunnel linings were investigated and discussed. In chapter 6, numerical simulations based on finite difference method (FDM) were performed to quantitatively analyze the reinforcing effects of FRP-PCM method on tunnel linings under seismic load, taking into accounts the influences of cavity position and construction method, and those analytic results could provide valuable guidance for the reinforcing of underground structures. Finally, major conclusions and some discussions of this thesis are provided in Chapter 7.

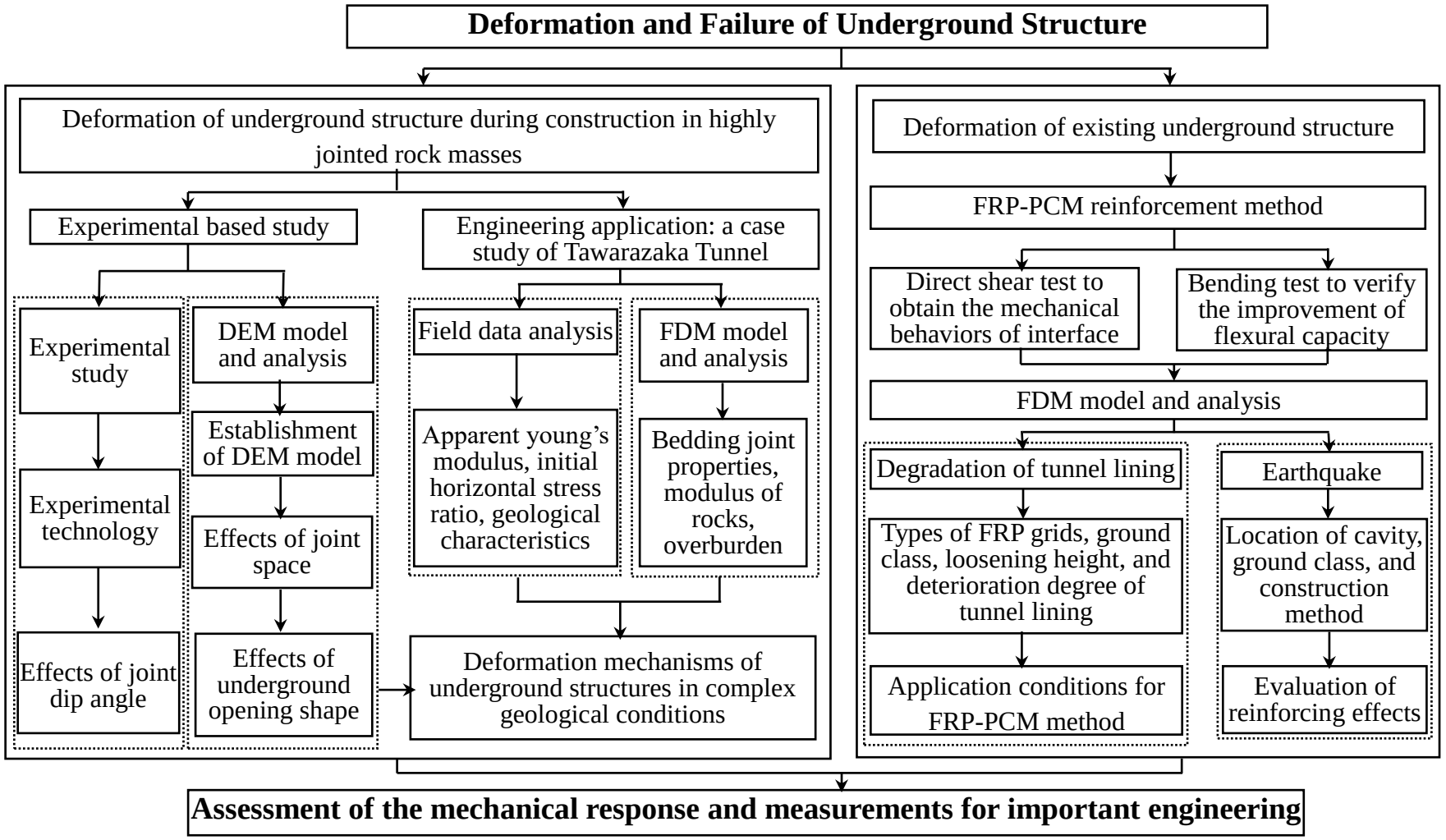

Fig. 1.1 Thesis structure

References:

Arduini M, Nanni A. Behavior of precracked RC beams strengthened with carbon FRP sheets. Journal of Composites for Construction, 1997, 1(2): 63-70.

Asakura T, Kojima Y. Tunnel maintenance in Japan. Tunnelling and Underground Space Technology, 2003, 18(2): 161-169.

Aydan Ö, Akagi T, Kawamoto T. The squeezing potential of rocks around tunnels; theory and prediction. Rock Mechanics and Rock Engineering, 1993, 26(2): 137-163.

Barla G. Innovative tunneling construction method to cope with squeezing at the Saint Martin La Porte access adit (Lyon-Turin Base Tunnel), ISRM Regional Symposium-EUROCK 2009. International Society for Rock Mechanics, 2009.

Berg A C, Bank L C, Oliva M G,Russel J S. Construction and cost analysis of an FRP reinforced concrete bridge deck. Construction and Building Materials, 2006, 20(8): 515-526.

Bilgin N, Algan M. The performance of a TBM in a squeezing ground at Uluabat, Turkey. Tunnelling and Underground Space Technology, 2012, 32: 58-65.

Bournas D A, Pavese A, Tizani W. Tensile capacity of FRP anchors in connecting FRP and TRM sheets to concrete. Engineering Structures, 2015, 82: 72-81.

Buyukozturk O, Hearing B. Failure behavior of precracked concrete beams retrofitted with FRP. Journal of composites for construction, 1998, 2(3): 138-144.

Cai M, Kaiser P K, Martin C D. A tensile model for the interpretation of microseismic events near underground openings. Pure and applied geophysics, 1998, 153, 67-92.

Cai M, Kaiser P K, Tasaka Y, Maejima T, Morioka H, Minami M. Generalized crack initiation and crack damage stress thresholds of brittle rock masses near underground excavations. International Journal of Rock Mechanics and Mining Sciences, 2004, 41, 833-847.

Ceroni F. Experimental performances of RC beams strengthened with FRP materials. Construction and Building Materials, 2010, 24(9): 1547-1559.

Chajes M J, Thomson T A, Januszka T F, Finch W W. Flexural strengthening of concrete beams using externally bonded composite materials. Construction and Building Materials, 1994, 8(3): 191-201.

Chen J F, Teng J G. Shear capacity of FRP-strengthened RC beams: FRP debonding. Construction and Building Materials, 2003, 17(1): 27-41.

Chiaia B, Fantilli A P, Vallini P. Combining fiber-reinforced concrete with traditional reinforcement in tunnel linings. Engineering Structures, 2009, 31(7): 1600-1606.

Chryssanthakis P, Barton N, Lorig L, Christianson M. Numerical simulation of fiber reinforced shotcrete in a tunnel using the discrete element method. International Journal of Rock Mechanics and Mining Sciences, 1997, 34(3): 54. e1-54. e14.

Clarke J L, Waldron P. The reinforcement of concrete structures with advanced composites. Structural Engineer, 1996, 74(17).

Cundall P A, Hart R D. Numerical modelling of discontinua. Engineering computations, 1992, 9, 101-113.

De la Fuente A, Pujadas P, Blanco A, Aguado A. Experiences in Barcelona with the use of fibres in segmental linings. Tunnelling and Underground Space Technology, 2012, 27(1): 60-71.

Esfahani M R, Kianoush M R, Tajari A R. Flexural behaviour of reinforced concrete beams strengthened by CFRP sheets. Engineering structures, 2007, 29(10): 2428-2444.

Franzén T. Shotcrete for underground support: a state-of-the-art report with focus on steel-fibre reinforcement. Tunnelling and Underground Space Technology, 1992, 7(4): 383-391.

Goodman E R, Shi G. Block Theory Application to Rock Engineering. Prentice-Hall, Englewood Cliffs, NJ, 1985, 338 p.

Hammah R E, Yacoub T, Corkum B, Curran J H. The practical modelling of discontinuous rock masses with finite element analysis. The 42nd US Rock Mechanics Symposium (USRMS), San Francisco, 2008, June 29–July 2, Document ID: ARMA-08-180.

Hao Y H, Azzam R. The plastic zones and displacements around underground openings in rock masses containing a fault. Tunnelling and underground space technology, 2005, 20, 49-61.

Hamidi J K, Bejari H, Shahriar K, Rezai B. Assessment of ground squeezing and ground pressure imposed on TBM shield. In: Proceedings of the 12th International Conference of International Association for Computer Methods and Advances in Geomechanics, Gao, India, 2008, 3907-3914.

Hensher D A. Fiber-reinforced-plastic (FRP) reinforcement for concrete structures: properties and applications. Elsevier, 2013.

Hoek E, Marinos P. Predicting tunnel squeezing problems in weak heterogeneous rock masses. Tunnels and tunnelling international Part 1 (November), 2000a, 32(11): 45-51.

Hoek E, Marinos P. Predicting tunnel squeezing problems in weak heterogeneous rock masses. Tunnels and tunnelling international Part 2 (December), 2000b, 32(11): 33-36.

Hoek E, Guevara R. Overcoming squeezing in the Yacambú-Quibor tunnel, Venezuela.

Rock Mechanics and Rock Engineering, 2009, 42(2): 389-418.

Jeng F, Lin M L, Yuan S C. Performance of toughness indices for steel fiber reinforced shotcrete. Tunnelling and underground space technology, 2002, 17(1): 69-82.

Jiang Y, Tanabashi Y, Li B, Xiao J. Influence of geometrical distribution of rock joints on deformational behavior of underground opening. Tunnelling and underground space technology, 2006, 21, 485-491.

Jiang Y, Li B, Yamashita Y. Simulation of cracking near a large underground cavern in a discontinuous rock mass using the expanded distinct element method. International Journal of Rock Mechanics and Mining Sciences, 2009, 46, 97-106.

Jimenez R, Recio D. A linear classifier for probabilistic prediction of squeezing conditions in Himalayan tunnels. Engineering Geology, 2011, 121(3): 101-109.

Jing L, Hudson J A. Numerical methods in rock mechanics. International Journal of Rock Mechanics and Mining Sciences, 2002, 39, 409-427.

Kiriyama K, Kakizaki M, Takabayashi T, Hirosawa N. Structure and construction examples of tunnel reinforcement method using thin steel panels. Nippon Steel Technical Report, 2005, 92: 45-50.

Kovári K, Staus J. Basic considerations on tunnelling in squeezing ground. Rock mechanics and rock engineering, 1996, 29(4): 203-210.

Kulatilake P, Malama B, Wang J. Physical and particle flow modeling of jointed rock block behavior under uniaxial loading. International Journal of Rock Mechanics and Mining Sciences, 2001, 38, 641-657.

Lau D, Pam H J. Experimental study of hybrid FRP reinforced concrete beams. Engineering Structures, 2010, 32(12): 3857-3865.

Lisjak A, Figi D, Grasselli G. Fracture development around deep underground excavations: Insights from FDEM modelling. Journal of Rock Mechanics and Geotechnical Engineering, 2014, 6, 493-505.

Martino J B, Chandler N A. Excavation-induced damage studies at the underground research laboratory. International Journal of Rock Mechanics and Mining Sciences, 2004, 41, 1413-1426.

Mezger F, Anagnostou G, Ziegler H J. The excavation-induced convergences in the Sedrun section of the Gotthard Base Tunnel. Tunnelling and Underground Space Technology, 2013, 38: 447-463.

Nystrom H E, Watkins S E, Nanni A, Murray S. Financial viability of fiber-reinforced polymer (FRP) bridges. Journal of Management in Engineering, 2003, 19(1): 2-8.

Saari K. Analysis of plastic deformation (squeezing) of layers intersecting tunnels and shafts in rock. Ph.D. Thesis, University of California, Berkeley, 1982.

Pešić N, Pilakoutas K. Concrete beams with externally bonded flexural FRP-reinforcement: analytical investigation of debonding failure. Composites Part B:

Engineering, 2003, 34(4): 327-338.

Sagong M, Park D, Yoo J, Lee J S. Experimental and numerical analyses of an opening in a jointed rock mass under biaxial compression. International Journal of Rock Mechanics and Mining Sciences, 2011, 48, 1055-1067.

Solak T. Ground behavior evaluation for tunnels in blocky rock masses. Tunnelling and Underground Space Technology, 2009, 24, 323-330.

Tanimoto C. NATM-1. Morikita Shuppan, 1984, 168-185 (in Japanese).

Tang C A. Numerical simulation of progressive rock failure and associated seismicity. International Journal of Rock Mechanics and Mining Sciences, 1997, 34, 249-261.

Tang C A, Yang W T, Fu Y F, Xu X H. A new approach to numerical method of modelling geological processes and rock engineering problems—continuum to discontinuum and linearity to nonlinearity. Engineering Geology, 1998, 49, 207-214.

Tang C A, Liu H, Lee P K K, Tsui Y, Tham L G. Numerical studies of the influence of microstructure on rock failure in uniaxial compression—part I: effect of heterogeneity. International Journal of Rock Mechanics and Mining Sciences, 2000, 37, 555-569.

Tang C A, Tham L G, Lee P K K, Tsui Y, Liu H. Numerical studies of the influence of microstructure on rock failure in uniaxial compression—part II: constraint, slenderness and size effect. International Journal of Rock Mechanics and Mining Sciences, 2000, 37, 571-583.

Täljsten B. Defining anchor lengths of steel and CFRP plates bonded to concrete. International Journal of Adhesion and Adhesives, 1997, 17(4): 319-327.

Timoshenko, S. and Goodier, J.N. Theory of Elasticity. McGraw-Hill Book Company. Inc., New York, 1951,506 p.

Toutanji H, Zhao L, Zhang Y. Flexural behavior of reinforced concrete beams externally strengthened with CFRP sheets bonded with an inorganic matrix. Engineering Structures, 2006, 28(4): 557-566.

Wang S H, Lee C I, Ranjith P G, Tang C A. Modeling the effects of heterogeneity and anisotropy on the excavation damaged/disturbed zone (EDZ). Rock mechanics and rock engineering, 2009, 42, 229-258.

Wang W W, Li G. Experimental study and analysis of RC beams strengthened with CFRP laminates under sustaining load. International journal of solids and structures, 2006, 43(6): 1372-1387.

Yao J, Teng J G, Chen J F. Experimental study on FRP-to-concrete bonded joints. Composites Part B: Engineering, 2005, 36(2): 99-113.

Zhu W C, Liu J, Tang C A, Zhao X D, Brady B H. Simulation of progressive fracturing processes around underground excavations under biaxial compression. Tunnelling

and Underground Space Technology, 2005, 20, 231-247.

CHAPTER 2

A review of tunnel deformation and control method in complex geological conditions

2.1 Introduction of complex geological conditions

Complexity is an ambiguous term, even from a purely geological perspective. A formation is characterized as complex rock formation either due to the complexity of its geological history, i.e. the processes that led to its present appearance or, more commonly, due to its present heterogeneity with respect to lithological and structural characteristics. In tunneling engineering filed, the deformations of tunnel were generally influenced by the complexity of surrounding rock masses. In this section, the deformation characteristics of two typical encountered soft or fractured rock masses in tunneling engineering were introduced.

2.1.1 Mechanical behaviors of soft rock masses

Many definitions and/or concepts regarding soft rocks have been proposed (Fan, 1995, Guo, 1996 and Lin, 1999). Although, in 1981, the International Society for Rock Mechanics (ISRM) raised the definition of soft rock: “the International Society for Rock Mechanics (ISRM) describes rock with an UCS (uniaxial/compressive strength) in the range of 0.25 MPa to 25 MPa as ‘extremely weak’ to ‘weak’ ” (ISRM, 1981), the definition of soft rock is still not commonly acknowledged. For typical simplicity, soft rocks have been classified into two sets (Clerici, 1992 and Russo, 1994): geological soft rock and engineering soft rock.

Geological soft rock refers to the rocks characterized by low stress, large porosity, poor cementation, broken surface and strong weathering-dependence, which basically contain swelling and loose clayey minerals and/or loose, soft, weak layers. The concept proposed by ISRM is within the scope of geological soft rock (He, 2014).

Engineering soft rock refers to the rocks that can produce significant plastic deformation under engineering forces (He, 2014). The concept of engineering soft rock emphasizes the importance of strength characteristics and the engineering forces, using the following conditions:

$$\left.\begin{array}{l}\sigma \geq [\sigma] \\ U \geq [U]\end{array}\right\} \tag{2.1}$$

where, σ is the engineering stress (MPa), $[\sigma]$ is the strength of engineering rock mass (MPa), U is the rock deformation (mm), and $[U]$ is the deformation allowance (mm).

The relationship between the geological soft rock and engineering soft rock is: when the load is smaller than the strength of geological soft rock (e.g. mud, shale), there is no significant plastic deformation of geological soft rock, so it is geological but not engineering soft rock. When the geological soft rock, e.g. shale and cemented sandstone, is under a condition of critical depth associated with high in situ stress, it would also undergo a significantly large deformation and displays soft rock characteristics. In such a case, it can be regarded as hard rock in terms of geology and/or soft rock in terms of engineering.

According to the strength characteristics, such as rock type, shale content, rock structure, surface characteristics and other mechanical characteristics associated with plastic deformation, soft rock can be divided into four categories, namely expansive soft rock (also called low-intensity soft rock), high-stress soft rock, jointed soft rock and combined soft rock, as shown in Table 2.1.

Table 2.1 Soft rock classification (He, 2014).

Class of soft rock	Conditions	Plastic deformation characteristics
Expansive soft rock (low-intensity)	Shale content > 25%	Under external loads applied, it slips along the clay mineral pieces of silicate, significant expansion under actionof water, etc.
High-stress soft rock	σ_c < 25MPa	A little inflation under action of water, it slips along the flaky clay minerals under high stress condition.
Jointed soft rock	$\sigma_c \geq$ 25MPa	Plastic deformations such as slip and expansion are produced along the jointed structure surface.
Combined soft rock	Shale content $\leq$ 25%	Complex mechanism with combination of the above-mentioned characteristics.

Note: σ_c is the uniaxial compressive strength (UCS).

2.1.2 Mechanical behaviors of jointed rock masses

A rock mass is a heterogeneous and discontinuous material commonly encountered in geotechnical engineering. The rock mass is composed of a system of rock blocks and rock joints, which behave in mutual dependence as a unit in the material (Matula et al., 1978). Due to the great diversity in the composition of intact rocks and in the properties and extent of fractures, the rock mass exhibits a high level of

complexity and uncertainty in its structure, and a high level of anisotropy and nonlinearity in its mechanical properties (Palmström, 1995 and 1996). To estimate the mechanical behavior of a rock mass, a comprehensive understanding of the mechanical structure of rock mass is required, involving the properties of intact rocks as well as the distribution and properties of rock joints.

Intact rocks are generally made up of an aggregate of crystals of different minerals and amorphous particles joined by varying amounts of cementing materials (Jaeger et al., 2007). Boundaries between crystals are weaknesses in the rock material, and lead to the discreteness of rocks. Besides the crystal boundaries, there are also some other types of defects existing in rocks, such as micro-cracks and micro-cavities, which may be generated by environmental stresses (Sang-Eun et al., 2006). Under external loads, the total deformation of rocks consists of the deformations of crystals and defects. Since defects have much lower strengths than crystals and can induce rock failure, they play a significant role in the mechanical behavior of rocks.

The mechanical performance of jointed rock masses is much more complicated than that of intact rocks, due to the involvement of discontinuities such as rock joints, fractures, cavities and etc. Rock joints divide the rock mass into a large number of sub-domains or blocks, whose sizes and interactions dominate the overall behavior of the rock mass (Jing, 2003). The existence of rock joints and fractures causes the stress redistribution and localized stress concentration in the host rock mass when subjected to external loads, which may subsequently lead to large plastic deformations and the failure of rock mass. Besides, joints in rock masses can open or close in the normal direction to their initial planes, and slide along their planes, making a major contribution to the overall deformation of the rock mass. Due to the controlling effects of discontinuities on the structure and mechanical behavior of rock masses, their geometrical and mechanical properties need to be investigated sufficiently in engineering practices.

The mechanical behavior of jointed rock masses also depend upon the scale and the detail involved in analysis, which is gennerally referred to as the scale effect (Da Cunha, 1993; Bamant. 2000; Fardin et al., 2001). At various scales, rock masses have different structures and contain different number of discontinuities with various shapes and extents. On a large scale of most concern in geotechnical engineering with dimensions from several meters to kilometers, the rock mass contains a great number of discontinuities such as joints and fractures, thereby, it usually has a lower strength than the small-scale rock mass such as samples used in laboratory tests (see Fig. 2.1). In engineering analysis, the proper scale of a mechanical model for a specific problem is important to perform a reliable assessment. To establish a reliable model, the rock mass structure needs to be investigated by means of geological and geophysical surveys,

including lithologies, boundaries of rock types and the distribution of fractures (especially the major joints and faults). Then mechanical properties of intact rocks and discontinuities need to be measured through laboratory tests on intact or fractured rock samples to provide reliable parameters for analysis.

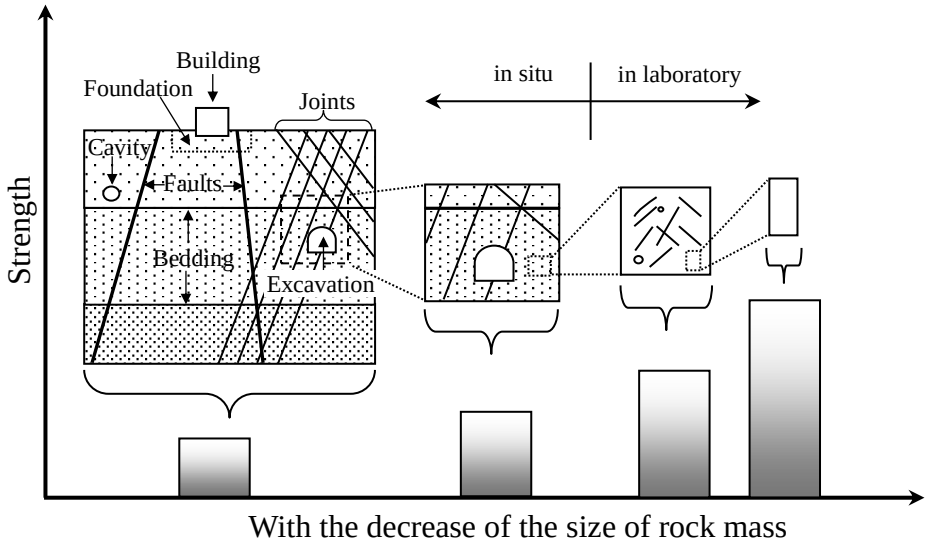

Fig. 2.1 Scale effect of rock mass and the variation of strength (after Palmström, 1995).

2.2 Deformations and control methods for tunnel in construction

2.2.1 Host rock response to excavation

2.2.2.1 Disturbed zone

Excavating tunnel in soft rock conditions will usually accident due to the complex geological conditions and mechanical behaviors of soft rocks (Zhou et al., 2014). The initial response to excavation is redistribution of stress from the excavated rocks into the surrounding medium (Hardin, 2014). This process concentrates stress near the walls, roof and floor of the opening. At distances exceeding 2 to 3 excavation diameters away from the opening, the stress magnitude changes in the excavation disturbed zone are relatively minor, i.e., less than 5% of the in situ stress magnitudes. Whereas the initial in situ stress condition in the host rock may be nearly lithostatic, the immediate stress condition adjacent to excavated openings is strongly deviatoric (i.e., large differences in stresses depending on direction). Deviatoric stresses can produce large deformations, dilatancy and fracturing especially in media with low strength compared to the overburden stress. For example, a soft shale unit with unconfined compressive strength of 5 MPa will undergo these effects when excavated at a depth of 300 m (7 MPa overburden stress). Strength increases with confinement, which occurs with increasing

distance from the opening, and also occurs after liner installation (Hardin, 2014).

Much of the immediate deformation associated with excavation occurs in the region ahead of, or close to the active excavating face. Thus, stress redistribution is inherently three -dimensional and produces three dimensional deformation features, where concentrated stress magnitudes exceed strength criteria. Dilatancy or bulking of the medium occurs when shear stress exceeds strength limits, and typically leads to weakening and plasticity. Pore fluid pressure release near an excavation may contribute to failure by pore-scale transfer of load from fluid pressure to the solid framework. Fractures form along surfaces of low normal stress and high shear, and parallel arrays of en echelon fractures form near the face as the tunnel is excavated. These excavation induced fractures may be evident as "chevron-like" shear fractures where they intercept the roof or walls of the tunnel (Delay et al. 2010). In laminar, anisotropic soft rock masses, these processes interact with pre-existing planes of weakness. The resulting fractures that form near the working face determine the extent of the excavation damage zone (EDZ) and deformation around every underground opening. Herein, the EDZ (see Fig. 2.2) is defined as the region beyond the excavation boundary where the physical, mechanical and hydraulic properties of the rock mass have been significantly affected as result of the excavation and redistribution of stresses.

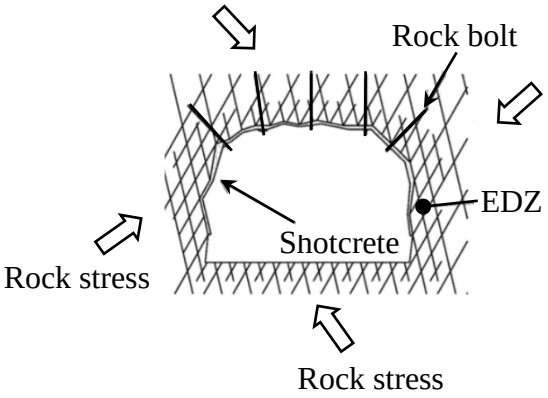

Fig. 2.2 EDZ around underground opening (Hardin, 2014).

2.2.2.2 Deformation/damaged zone

Practice experience from underground excavation in massive soft rock mass indicate that the amount of damage around an underground opening can be estimated by considering the ratio of σ_1 and σ_c, where σ_1 is the maximum far-field stress magnitude and σ_c is the laboratory short-term unconfined compressive strength.

When the ratio of $\sigma_1/\sigma_c < 0.1$, the rock mass will respond elastically and no excavation-induced damage or large deformation will occur in the disturbed zone. At a ratio of $\sigma_1/\sigma_c \approx 0.2$, some cracking that induced by large deformation will occur in the

disturbed zone close to the excavation wall, as a result of either the removal of the confining stresses or the loading by stress concentrations, thus creating a permanent deformation zone near the opening. This crack-induced damage weakens the rock by reducing its cohesive strength component; the largest reductions occur at the tunnel wall, where the damage is the greatest. Outside this damaged zone, the peak cohesive strength of the rock mass is unaffected. At a ratio of $\sigma_1/\sigma_c \approx 0.3$, the rock mass is so severely deformed or damaged near the opening that the maximum load-bearing capacity of the rock mass is exceeded. The accumulated strains in the damaged zone are excessive and crack coalescence will lead to rock mass disintegration, e.g., by slabbing of the excavation walls. However, even if slabbing occurs, the shape of the opening eventually will stabilize and the surface instability mechanisms will disappear. The opening will remain stable unless further disturbed, e.g., by a disturbance from a nearby opening or by stress changes caused by thermal gradients. At ratios of $\sigma_1/\sigma_c >$ 0.5, the failure process propagates and deformation of rocks developes rapidly, extending the depth of the damaged zone. These conditions are generally found at great depth or in tunnels where extraction ratios are very high, i.e., greater than 30-60%. Consequently, from a stability point of view, unstable or severe rock mass damage is of concern only at great depth or if two openings interfere because of their close proximity.

2.2.2.3 The main deformation behaviors of soft rocks

(1) Swelling and shrinkage.

The potentially destabilizing behaviors, such as swelling and shrinkage, have been understood for many years in soft rock tunneling, and referred to as slaking. It can be serious when groundwater that flows into underground openings interacts with exposed sensitive rock surfaces (Einstein, 1996 and Anagnostou, 1993).

Swelling ground displaces into the tunnel as a result of an increase in volume of the rock mass surrounding the tunnel due to the adsorption of water. When the volume increase is resisted significant swelling pressures can develop (Klein 2001). Swelling is mainly limited to the fine-grained rocks mentioned above that contain an appreciable amount of swelling clay minerals like montmorillinite (or smectite). Swelling can also occur due to the chemical or hydrothermal alteration of minerals such as feldspar, which produces montmorillinite, and also due to the hydration of anhydrite, which produces gypsum. Stress-induced cracking may facilitate access to water and promote swelling. The potential for swelling can be evaluated from the results of laboratory tests such as free swell tests, Atterberg limit determinations, grain size analyses to determine the clay content (< 2 micron), and X-ray diffraction evaluations (to determine the type of clay minerals present). Terzaghi (1946) indicates that swelling ground will increase in volume by more than 2 percent when immersed in water and Heuer (1974) indicates

that materials with a plasticity index exceeding 30 will exhibit a significant swelling potential. Kormornik and David (1969) conducted extensive testing and developed an equation between the water content, dry density, liquid limit, and the swelling pressure, and the swelling pressure from the liquid limit and dry density can be determined based on their studies. Howard et al. (1975) indicate that significant swelling problems are likely when the estimated swelling pressure is greater than about 250 kPa and very unlikely for swelling pressures less than 150 kPa. ISRM provides a test procedure for directly measuring the swelling pressure of a rock sample (ISRM, 1981).

(2) Squeezing

Squeezing behavior is progressive deformation that starts immediately after excavation and can produce large opening closure deformation within days to months. Squeezing is characterized by time-dependent deformations, which are associated with yielding, creep, or plastic behavior caused by overstressed conditions in the rock mass around the tunnel. Some of the effects of squeezing are evident immediately following excavation such as the convergence that occurs at the tunnel face, but there are long-term effects as well, including continued ground movements and a gradual buildup of load on the tunnel support system. The magnitude of the ground movements (i.e., tunnel convergence) associated with squeezing, the extent of the yielding zone around the tunnel, ground loads, and support requirements depend on the rock type, rock mass strength and deformation properties, and the in situ stress conditions. It is found that squeezing of ground is commonly occurred in soft rock masses with bedding joints. Stress analyses and ground-lining interaction analyses are usually carried out to address these issues. Approaches have been developed to do this and are discussed elsewhere (Deere et al., 1969; Jewtha et al., 1984).

2.2.2 A short review of development of commonly used deformation control method

Excavating tunnel in soft rocks usually will cause accident due to the complex geological conditions and mechanical behaviors of soft rocks. Many methods of support techniques have been proposed consequently to minimize the deformations induced by tunnel excavation and to ensure the stability of both the rock mass and its support structures. For example, the New Austrian Tunnelling Method (NATM) (Han, 1987), which is also known as the sequential excavation method (SEM), is a popular method used in modern tunnel design and construction. Salamon (1970) studied the support system in terms of energy. The support structure and surrounding rock simultaneously generate compatible deformation, and the support structure can absorb part of the dispersed energy from the surrounding rock mass. Feng (1990) proposed a combined support method, in which increasing the thickness of support was not the optimum method for tunneling in soft rocks, and the method of preflexibility and post-stiff was

of priority. He et al. (1994, 2007) suggested that the support technique for deep tunneling should be carried out in two steps: first flexible support, followed by a coupling support for the critical parts. Dong et al. (1994) also proposed a support theory for 'loose circles' in the surrounding rock mass. More recently, several researchers have proposed a large number of novel excavation and support methods to control the squeezing behaviour of the rock mass, e.g., the DSM method adopted by Barla et al. (2007) and the (steel) fibre reinforced high-strength shotcrete method adopted by Hisatake (2003) and Sustersic et al. (2004). In summary, these methods can be divided into two types: (i) the passive approach, and (ii) the active method. The so-called 'passive approach', which aims at accommodating large deformations, is preferred to the so-called 'active method', which aims at preventing rock deformation. For instance, the only feasible solution in heavily squeezing ground is a tunnel support that is able to deform without becoming damaged, in combination with a certain amount of over-excavation in order to accommodate the deformations. Supports which are based on this so-called 'yielding principle' can be structurally implemented in two main ways (Cantieni and Anagnostou, 2009): either by arranging a compressible layer between the excavation boundary and the extrados of a stiff lining, or through a suitable structural detailing of the lining that will allow a reduction in its circumference. In the first case, the ground undergoes convergences, while the clearance profile remains practically constant. This solution has been proposed particularly for shield tunneling with stiff segmental linings (Billig et al., 2008). The second solution is the one usually applied today. It involves steel sets with sliding connections in combination with shotcrete. Moreover, in order to achieve the required clearance profile after convergence, the tunnel is excavated to a certain size, which accommodates the convergence and support installation, including the inner lining. Consequently, a flexible support, over-excavation, longitudinal gaps in the shotcrete lining and yielding rock bolting are commonly applied to deal with large deformation problems of tunnels in deep soft rocks.

2.3 Deformations and control methods for tunnel in operation

2.3.1 Deformation of tunnels in operation caused by deterioration

Japan is a country that surrounded by sea and 70% of its land is covered by mountains. A large number of tunnels have been constructed during the last several decades, and those tunnels have been become an indispensable part of the national traffic networks. To date, a great number of tunnels have been in service for more than 50 years. Fig. 2.3 shows the number of tunnels that have been constructed more than 50 years in Japan (The ministry of land, infrastructure, transport and tourism, 2005).

In recent years, damages such as cracking, spalling, generation of internal voids, and water leakage occur frequently on degraded tunnels, which would lead to large deformation on tunnel linings and significantly undermine the workability, serviceability and safety reliability of tunnel operations (Aktan et al., 2000; Bhalla et al., 2005, Asakura et al., 2000; Asakura et al., 2003; Yu et al., 2007). The causes of deterioration can be classified broadly into two types:

(1) Those caused by the deterioration of materials such as lining concrete.

(2) Those caused by external pressure, including seismic load, earth pressure and freezing pressure.

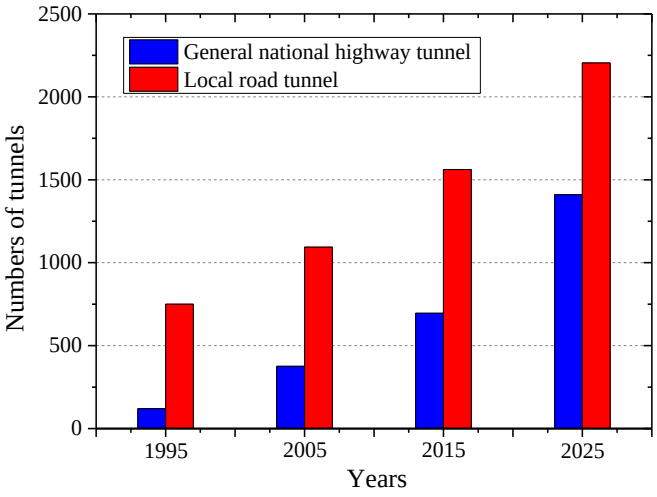

Fig. 2.3 The number of tunnels that have been constructed for more than 50 years.

2.3.2 Commonly used reinforcement methods for tunnel in operation

A series of reinforcement methods are adopted to improve the integrity of lining structures, typical ones of which are grouting reinforced (GR) method, fiber reinforced shotcrete (FRS) method, carbon fiber sheet (CFS) method, steel plate bonding (SPB) method and Fiber reinforcement plastic (FRP) method (Railway Technical Research Institute, 1998).

2.3.2.1 Grouting reinforced method

Sheet piling method is generally adopted in tunnel construction before the development of New Austrian Tunneling Method (NATM). Due to the use of steel supporting structures and sheet piles, back cavities may occur between the lining structures and surrounding rock masses, especially on the crown of arches. Lining deformation occurs mostly owing to the local discontinuity caused by back cavities. GR method is generally selected to control the tunnel deformation, taking into accounts the existence of back cavities, as shown in Fig. 2.4. Not only the traditional bowling method

but also the nondestructive methods, such as the electromagnetic wave method using geology radar, ultrasonic method and etc., are proposed to determine the location of back cavities. As a general use, cement is usually selected as the main grouting material, which is determined by the water bursting situation and scale of back cavities.

2.3.2.2 Fiber reinforced shotcrete method

In the past few decades, FRS method as shown in Fig. 2.5 was widely used in the tunnel lining reinforcement fields (De la Fuente et al., 2012; Chiaia et al., 2009; Chryssanthakis et al., 1997; Jeng et al., 2002; Franzén, 1992). FRS was not only selected as a part of tunnel structures to bear the ground pressure, but also as a measurement to prevent the cracks, water leakage, freezing damage and etc. In recent years, steel fibers have been added into reinforced shotcrete to improve the bearing capacities of reinforcement materials, and to prevent the spalling of lining concrete. Besides, the spraying thickness can also be reduced by 10 mm due to the adoption of steel fibers. The FRS method have been commonly used in tunneling practice in many countries, especially in Europe and in the United States (Franzén, 1992 and Morgan et al., 1995). The international symposiums and conferences on spray concrete have been held in Norway and other countries at least since 1993 (Kompen et al., 1993, Barton et al., 1996 and Barton et al., 1999). The FRS method is characterized by ductile behavior, namely better post-cracking strength and energy absorption. Since the steel fibers can transmit the tensile force between cracks, the structures that reinforced by FRS method still have a certain carrying capacity after cracking.

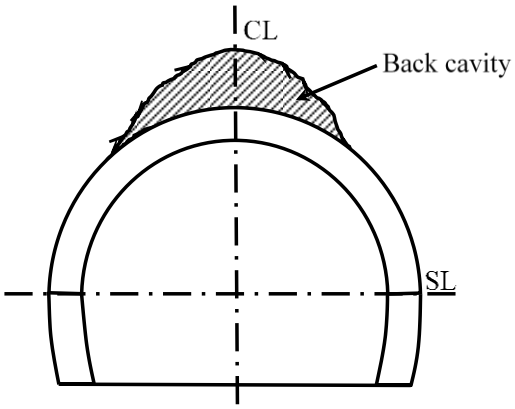

Fig. 2.4 Grouting reinforced method

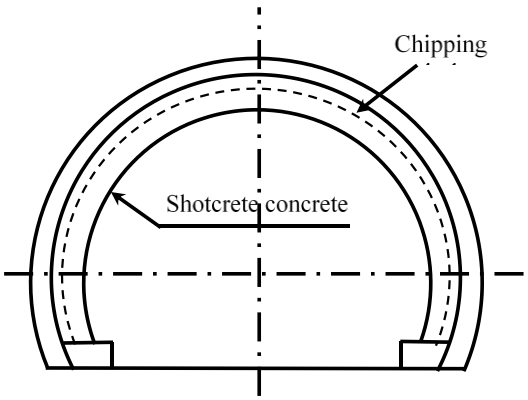

Fig. 2.5 Fiber reinforced shotcrete method

2.3.2.3 Carbon fiber sheet method

Recently, carbon fiber sheet (CFS) has been widely used for reinforcement and rehabilitation of damaged concrete structures (Lee et al., 2002; Miyauch, 1997; Katsumata et al., 1988; Gagio et al., 1998; Yokoyama et al., 1998 Spadea et al., 1997),

since they offer many advantages when compared to conventional steel (such as high specific strength and stiffness, low weight, high workability, easy handling and application). However, there are also some disadvantages, such as low compressive strength, inflammable, easy to deterioration and etc. Fig. 2.6 shows an example of application of CFS method.

2.3.2.4 Steel plate bonding method

The steel plate bonding method as shown in Fig. 2.7 has been widely used in tunnel engineering field due to its minor effects on tunnel cross sections. In this method, anchor bolt is employed as a main tool for the fix of steel plate. The steel plate bonded at the inner surface of lining structures can improve the tensile strength of tunnels and decrease the development of bending cracks. However, compared with the carbon fiber steel board method, the steel plate bonding method is difficult to construct, conducting, and susceptible to corrosion.

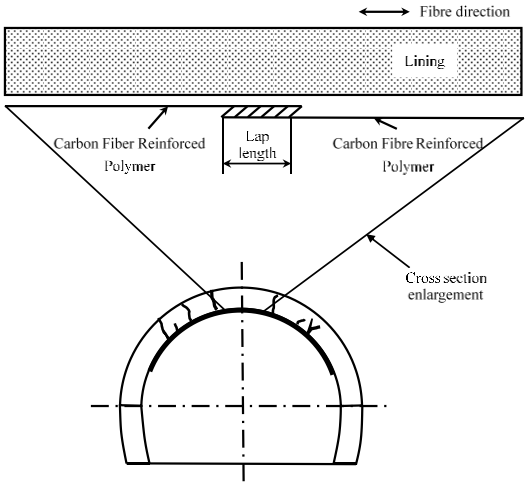

Fig. 2.6 Carbon fiber sheet method.

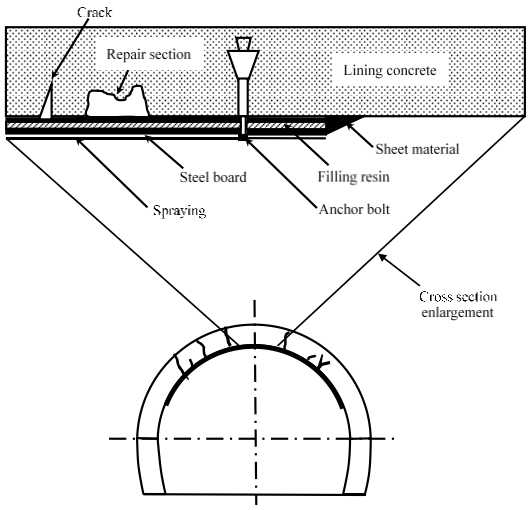

Fig. 2.7 Steel plate bonding method.

2.3.2.5 Fiber reinforcement plastic method

FRP method has become a practical alternative construction method in reinforcing concrete structural aspects (Research Society of FRP Grid Construction, 2007). Due to the favorable properties, such as high strength, low weight, high workability, easy handling and application, high strength, immunity to corrosion, minimal disruption of occupancy and etc.(Lau and Pam, 2010; Bournas et al., 2015), FRP as a strengthening material for reinforced concrete (RC) structures has become commonly used in engineering fields. Reinforcements using the FRP method can improve the performance of the existing concrete structures by installing FRP grids (see Fig .2.8)) and spraying

PCM on the surfaces of the existing structures (see Fig .2.8), such as bridges, box culverts and tunnel linings (Nakamura et al., 2009; Watanabe et al., 2009). For instance, if a concrete slab of a road bridge is reinforced with the FRP-PCM method, PCM and slab will be integrated to increase the thickness of the slab, while FRP grid will help improve the flexural, shear capacities and ductility of slabs (Lau and Pam, 2010; Grace et al., 1996; Triantafillou, 1998; Deniaud and Roger Cheng, 2003; Greco et al., 2007; Bruno et al., 2007). The FRP method can also improve the corrosion resistance of concrete by providing a cover for the existing concrete in some harsh environments where carbonation, salt damage, alkali-aggregate reaction and etc. are the main reasons for the deteriorations of concrete.

Fig. 2.8 Fiber reinforcement method (Higashi et al., 2012).

References:

Aktan A E, Catbas F N, Grimmelsman K A, Tsikos C J. Issues in infrastructure health monitoring for management. Journal of Engineering Mechanics, 2000, 126(7): 711-724.

Asakura T, Kojima Y. Tunnel maintenance in Japan. Tunnelling and Underground Space Technology, 2003, 18(2): 161-169.

Asakura T, Shiba Y, Matsuoka S, Matsuoka S, Yashiro K, Shiba Y, Oya T. Damage to mountain tunnels by earthquake and its mechanism//Proceedings-Japan Society of Civil Engineers. DOTOKU GAKKAI, 2000: 27-38.

Bamant Z. Size effect. International Journal of Solids and Structures, 2000, 37: 69-80.

Barla G, Barla M, Bonini M, Debernardi D. Lessons learned during the excavation of the Saint Martin La Porte access gallery along the Lyon-Turin Base tunnel. In: Schneider, E., John, M. & Brandner, R. (eds.), BBT 2007, Internationales Symposium.

Barton N R, Kompen R, Berg K. (Eds.), In the Procedings of the Second International Symposium on Sprayed Concrete -Modern Use of Wet Mix Sprayed Concrete for Underground Support, Fagernes, Gol, Norwegian Concrete Association, Norway, 1996.

Barton N R, Berg K, Davik K I, Garshol K, Grimstad E. (Eds.), In the Proceedings of the Third International Symposium on Sprayed Concrete - Modern Use of Wet Mix Sprayed Concrete for Underground Support, Gol, Norway, Norwegian Concrete Association, 1999, 525.

Bhalla S, Yang Y W, Zhao J, et al. Structural health monitoring of underground facilities–Technological issues and challenges. Tunnelling and Underground Space Technology, 2005, 20(5): 487-500.

Billig B, Gipperich C, Wulff M, Schaab A. Ausbausysteme für den maschinellen Tunnelbau in druckhaftem Gebirge. In: Taschenbuch für den Tunnelbau 2008. Essen: Verlag Glückauf GmbH, 2008: 223-262.

Bournas D A, Pavese A, Tizani W. Tensile capacity of FRP anchors in connecting FRP and TRM sheets to concrete. Engineering Structures, 2015, 82: 72-81.

Bruno D, Carpino R, Greco F. Modelling of mixed mode debonding in externally FRP reinforced beams. Composites Science and Technology, 2007, 67(7): 1459-1474.

Cantieni L, Anagnostou G. The interaction between yielding supports and squeezing ground. Tunn Undergr Sp Tech, 2009, 24, 309-322.

Chiaia B, Fantilli A P, Vallini P. Combining fiber-reinforced concrete with traditional reinforcement in tunnel linings. Engineering Structures, 2009, 31(7): 1600-1606.

Chryssanthakis P, Barton N, Lorig L, Christianson M. Numerical simulation of fiber

reinforced shotcrete in a tunnel using the discrete element method. International Journal of Rock Mechanics and Mining Sciences, 1997, 34(3): 54. e1-54. e14.

Clerici A. Engineering geological characterization of weak rocks: classification, sampling and testing. In: ISRM Symposium Eurock; 1992, 179-82.

Da Cunha A.P. Scale effects in rock masses. Balkema, Rotterdam, Holland, 1993.

Deere D U, Peck R B, Monsees J E, Schmidt B. Design of tunnel liners and support systems. Report prepared for U.S. Department of Transportation. OHSGT Contract 3-0152. NTIS, 1969.

De la Fuente A, Pujadas P, Blanco A, Aguado A. Experiences in Barcelona with the use of fibres in segmental linings. Tunnelling and Underground Space Technology, 2012, 27(1): 60-71.

Delay J, P Lebon, H Rebours. "Meuse/Haute-Marne centre: next steps toward a deep disposal facility." J. of Rock Mech. and Geotech. Engr. 2010, 2(1). pp. 52-70.

Deniaud C, Roger Cheng J. Reinforced concrete T-beams strengthened in shear with fiber reinforced polymer sheets. Journal of Composites for Construction, 2003, 7(4): 302-310.

Dong F T, Song H W, Guo Z H, Lu S M, Liang S J. Roadway support theory based on broken rock zone. Journal of China Coal Society. 1994, 19: 22-32. (in Chinese)

Fan QY. Discussions about determination of soft rock and critical depth of tunnels. Ground Pressure and Strata Control 1995; (Suppl. 1):115e7 (in Chinese).

Fardin N., Jing L. and Stephansson O. The scale dependence of rock joint surface roughness. International Journal of Rock Mechanics and Mining Sciences, 2001, 38: 659-669.

Feng Y. Research on the tunnel support of soft rock in China. Ground Pressure and Strata Control, 1990, 7: 1-5. (in Chinese)

Franzén T. Shotcrete for underground support: a state-of-the-art report with focus on steel-fibre reinforcement. Tunnelling and Underground Space Technology, 1992, 7(4): 383-391.

Gagio Hiroya, Katsumata Dideo, Kimura Kohzo, K. Yoshiro. A study of existing reinforced concrete structure retrofitted by carbon fiber. ACCM-1, 1998, 107.1-107.4.

Grace N F, Sayed G A, Soliman A K, Saleh K R. Strengthening reinforced concrete beams using fiber reinforced polymer (FRP) laminates. ACI Structural Journal, 1999, 96(5).

Greco F, Lonetti P, Blasi P N. An analytical investigation of debonding problems in beams strengthened using composite plates. Engineering Fracture Mechanics, 2007, 74(3): 346-372.

Guo Z. A study on the mechanical properties of the incompetent rocks. Journal of Engineering Geology 1996;4(3):79-84 (in Chinese).

Han R G. New Austrian tunnelling method in underground engineering. Beijing: Science Press, 1987. (in Chinese)

Hardin E L. Review of Underground Construction Methods and Opening Stability for Repositories in Clay/Shale Media. 2014.

He M C. Latest progress of soft rock mechanics and engineering in China. Journal of Rock Mechanics and Geotechnical Engineering, 2014, 6(3): 165-179.

He M C. Constitutive relationship for plastic dilatancy due to weak intercalations in rock masses. In: Proceedings of the 26th Annual Conference of the Engineering Group of the Geological Society. Rotterdam: A.A. Balkema; 1994, 4173-80.

He M C, Yang J, Qi G. Optimized design and its application of coupling support for soft rock roadway at great depth. J Liaoning Tech Univ, 2007, 26: 40-42.

Heuer R E. Important Ground Parameters in Soft Ground Tunneling. Proceedings of Subsurface Exploration for Underground Excavation and Heavy Construction. ASCE. New York. 1974, 41-55.

Higashi Y, Li B, Jiang Y. Reinforcement effect of PCM shotcrete method using FRP grid for tunnel maintenance//Renewable Energy Research and Applications (ICRERA), 2012 International Conference on. IEEE, 2012: 1-5.

Hisatake M. Effects of steel fiber reinforced high-strength shotcrete in a squeezing tunnel. Tunn Undergr Sp Tech, 2003, 18: 197-204.

Howard T R, Brekke T L, Houston W N. Laboratory Testing of Fault Gouge Materials. Bulletin of the Association of Engineering Geology. 1975, XII(4). 303-315.

International Society for Rock Mechanics (ISRM). Rock characterization testing and monitoring. New York: Pergamon Press; 1981. p. 211.

Jaeger J C, Cook N G W, Zimmerman R W. Fundamentals of rock mechanics (4th edition). Blackwell Publishing Ltd, Oxford, UK, 2007.

Jeng F, Lin M L, Yuan S C. Performance of toughness indices for steel fiber reinforced shotcrete. Tunnelling and underground space technology, 2002, 17(1): 69-82.

Jethwa J L, B Singh, B Singh. Estimation of ultimate rock pressure for tunnel linings under squeezing rock conditions - A New Approach. Proceedings of Design and Performance of Underground Excavations. ISRM. Cambridge. England. 1984: 231–238.

Jing L. A review of techniques, advances and outstanding issues in numerical modelling for rock mechanics and rock engineering. International Journal of Rock Mechanics & Mining Sciences, 2003, 40: 283-353.

Katsumata H, Kobatake Y, Takeda T. A study on strengthening with carbon fiber for earthquake-resistant capacity of existing reinforced concrete columns//Ninth

World Conference on Earthquake Engineering. 1988: 517-522.

Klein S. An approach to the classification of weak rock for tunnel projects//PROCEEDINGS OF THE RAPID EXCAVATION AND TUNNELING CONFERENCE. 2001: 793-806.

Komornik A, D David. Prediction of swelling pressure of clays. Journal of Soil Mechanics and Foundations Division. ASCE. 1969, 95(SM 1. January): 209-225.

Kompen R, Opsahl O A, Berg K R (Eds.). In Proceedings of the First International Symposium on Sprayed Concrete, Fagernes,, Norwegian Concrete Association, Norway, 1993.

Lau D, Pam H J. Experimental study of hybrid FRP reinforced concrete beams. Engineering Structures, 2010, 32(12): 3857-3865.

Lee J K, Lee J H. Nondestructive evaluation on damage of carbon fiber sheet reinforced concrete. Composite structures, 2002, 58(1): 139-147.

Lin YL. The research on several theoretical problems about engineering mechanics of soft rock. Chinese Journal of Rock Mechanics and Engineering 1999, 18 (6): 690-3 (in Chinese).

Matula M. and Holzer R. Engineering topology of rock masses. In: Proceedings of Felsmekanik Kolloquium, Grundlagen ung Andwendung der Felsmekanik, Karlsruhe, Germany, 1978: 107-121.

Miyauchi K. Estimation of strengthening effects with carbon fiber sheet for concrete column. Proceedings of the 3rd International Symposium on Non-Metallic (FRP) Reinforcement for Concrete Structures. Japan Concrete Institute, 1997: 217-224.

Morgan D R, Chen L, Beaupre D. Toughness of fibre reinforced shotcrete (Shotcrete for Underground Support VII). ASCE, 1995: 66-87.

Nakamura S, Yamaguchi K, Amiruddin A. Arwin, Taniguchi K. Effect of bending reinforcement of RC beam using CFRP grid by contacted arrangement two layers by PCM shotcrete method, Concrete Engineering, 2009, 31: 1429-1434.

Palmström A. RMi – a rock mass characterization system for rock engineering purposes. Ph.D thesis, Oslo University, Oslo, Norway, 1995.

Palmström A. Characterizing rock masses by the RMi for use in practical rock engineering – Part 1: The development of the Rock Mass index (RMi). Journal of Tunnelling and Underground Space Technology, 1996,11(2): 175-188.

Railway Technical Research Institute. Design manual of tunnel deformation measurements, 1998. (in Japanese)

Research society of FRP grid construction method. Design and construction manuals of reinforcement for concrete structure by FRP grid thicken or lining method (plan), 2007. (in Japanese)

Russo G. Some considerations on the applicability of major geomechanical classifications to weak and complex rocks in tunnelling. GEAM, 1994, 82: 63-70.

Salamon MDG. Stability, instability and design of pillar workings. International Journal of Rock Mechanics and Mining Sciences & Geomechanics Abstracts. 1970, 7(6):613e31.

Sang-Eun L, Man-II K, Jae-Hyeon P, Chang-Kun P, Meea K, Gyo-Cheol J. Damage process of intact granite under uniaxial compression: microscopic observations and contact stress analysis of grains. Geosciences Journal, 2006, 10(4): 457-463.

Spadea G, Bencardino F. Behavior of fiber-reinforced concrete beams under cyclic loading. J. Struct. Eng. 1997, 660-668.

Šušteršicˇ J, Jovicˇicˇ V, Zajc A, Ercegovicˇ R. Evaluation of improvement in the bearing capacity of fibre reinforced shotcrete tunnel lining. In: Di Prisco, M., Felicetti. R. & Plizzari, G.A. (eds.) Fibre Reinforced Concrete, BEFIB 2004: Proceedings of Sixth International RILEM Symposium, 20–22 September, 2004, Varenna, Italy. F-92220 Bagneux – France: RILEM Publications S.A.R.L., 2004, 2: 985-994.

Terzaghi K. Introduction to Tunnel Geology. Rock Tunneling with Steel Supports, R.V. Proctor and T.L. White eds. Youngstown: Commercial Shearing. 1946, 19–99.

The ministry of land, infrastructure, transport and tourism: White Paper of Land, Infrastructure, Transport and Tourism [R]. Tokyo: National Printing Bureau, 2005.

Triantafillou T C. Shear strengthening of reinforced concrete beams using epoxy-bonded FRP composites. ACI Structural Journal, 1998, 95(2): 107-115.

Watanabe H, Hino S, Yamaguchi K, Amiruddin A. Arwin. Experimental research of bond strength in CFRP grid contacted two layers, Concrete Engineering, 2009, 31: 1411-1416.

Yokoyama Atsushi, Nishiyabu Kazuakki.Fracture behavior of concrete beam strengthen with composite materials. ACCM-1, 1998: 103.1–103.4

Yu S N, Jang J H, Han C S. Auto inspection system using a mobile robot for detecting concrete cracks in a tunnel. Automation in Construction, 2007, 16(3): 255-261.

Zhou H, Zhang C, Li Z, et al. Analysis of mechanical behavior of soft rocks and stability control in deep tunnels. Journal of Rock Mechanics and Geotechnical Engineering, 2014, 6(3): 219-226.

CHAPTER 3

Experimental and numerical study on crack propagation and deformation around underground opening

3.1 Introduction

Understanding the stability of underground structures during excavation is an important issue in many engineering fields, such as mining, tunneling, power plants and radioactive disposal facilities. The deformation and failure behaviors of underground openings are generally governed by the geological discontinuities such as faults, joints and cracks, which exist in the host rock masses (Chappell, 1979; Dershowitz et al., 1988; Kulatilake et al., 1993; Lu, 2002; González-Palacio et al., 2005).In tunneling and mining operations, external loads and excavation disturbance could trigger the crack initiation, propagation and coalescence of microcracks in host rock masses, which may impact the mechanical behavior of rock masses, thereby affecting the long-term safety of underground structures (Cai et al., 1998; Cai et al., 2004; Martino et al., 2004; Wang et al., 2009). Therefore, an improved understanding of the deformation and failure mechanisms of host rock masses caused by discontinuities is essential to assess the stability of underground structures.

The general approach to investigate the deformation and failure behaviors around underground opening could be divided into three parts: classical analytical solution, model test and numerical analysis. Timoshenko and Goodier (1951) investigated the distributions of radial, tangential and shear stresses at the boundary of underground opening subjected to biaxial stress conditions. Depending on the various lateral pressure coefficients, typical stress distributions around the circular and elliptical underground opening in homogeneous rock masses were deduced. Goodman and Shi (1985) proposed a blocky theory to evaluate the stability of rock masses around underground openings. In the blocky theory, removability analysis was conducted on the rock blocks based on a precise characterization of rock joints (e.g. orientation, location, and spacing), underground opening shape, and width of underground opening. Although the capacity of this theory was increased with considering stress conditions, decrease of forces acting on the key block (Brady and Brown, 2004), these typical solutions are not applicable to the cases where ground shows anisotropy.

Several numerical studies have been contributed to investigating the deformation and failure behaviors of an underground opening in jointed rock masses. Two of the

most commonly adopted methods are continuum-based and discontinuum-based methods (Jing and Hudson, 2002). Among the continuum-based methods, the finite difference method (FDM) that uses a differential form of the governing partial differential equations is commonly utilized to investigate the deformation of rock masses during the excavation of underground openings (Lisjak et al., 2014). Although the joint elements can be integrated into the continuum formulation, the calculation precision could be seriously restricted by the increment of joint numbers (Hammah et al., 2008). The realistic failure process analysis (RFPA) code based on the finite element method (FEM) is commonly used to reproduce the failure process of quasi-brittle materials such as rock masses (Tang, 1997; Tang et al., 1998, 2000a, 2000b). The Young's modulus and uniaxial compressive strength were conformed to a Weibull distribution to characterize the nonlinear behaviors of deformation and failure of rock masses (Zhu, 2005). The RFPA code was applied to evaluate the deformation and failure process of rock masses around various types of underground openings, and it was found that the development of primary tensile cracks was governed by the lateral pressure coefficient (Zhu, 2005). Jia and Tang (2008) conducted the RFPA code to investigate the influences of dip angle and lateral pressure coefficient on the failure mode around the underground openings. They found that for a horizontal layered joints, the failure mode is the break of "rock beam"; for a moderate joint dip angle (30° and 45°), the failure occurs at the shoulder of underground opening caused by the flexing and breaking of layer blocks; for a high joint dip angle (60°), the failure mode is triggered by the sliding of rock masses along the joints. Wang et al. (2009) also utilized this modeling technique to confirm the effects of anisotropy and heterogeneity on the deformation of rock masses around underground openings and found that the fracture initiation and propagation in rock masses are triggered by a combination of the weak plane and stress concentration caused by the transverse anisotropy. One of the most commonly used discontinuum-based approach is the discrete element method (DEM), in which the materials such as rock masses are treated as an assemblage of independent rigid or deformable blocks, or particles with certain particle friction and bond strength to reproduce the strength of intact and/or jointed rock masses (Cundall et al., 1992). Shen and Barton (1997) classified the rock mass states around an underground opening into three types: the failure zone, open zone and shear zone based on the DEM. Hao and Azzam (2005) investigated the plastic zone and deformation around underground opening in rock masses containing a fault utilizing the DEM, and found that the physical parameters of fault play an important role on the deformation of host rock masses. Solak (2009) performed a parametric study based on the DEM, taking into accounts various joint characteristics and in situ stresses to investigate the deformation behaviors of host rock masses around a circular opening, and a delimiting criteria to classify the ground

behavior was established. Jiang et al. (2006) discussed the deformation behavior of rock masses around an underground opening from a fractal dimension perspective, and found that the deformation increases with the increment of fractal dimension of rock joint distributions. An expanded distinct element method (EDEM) was later developed by Jiang et al. (2009) to investigate the cracking procedure in jointed rock masses, and it was found that the number of newly generated cracks increases with the increment of depth of underground opening and initial ground stress. The generation of new cracks in a few weak zones is significantly influenced by the positions of existing rock joints. Sagong et al. (2011) conducted numerical analysis based on particle flow code (PFC) to investigate the fracture and sliding behaviors of jointed rock masses around a circular opening, and found that the damage zones increase with the decrease of joint dip angle. Jiao et al. (2012 and 2014) proposed an extended Discontinuous Deformation Analysis (DDA) called DDARF to simulate the shear behavior and even the hydraulic fracturing of jointed rock mass, and found that this newly proposed numerical model can simulate the hydraulic fracturing process correctly and effectively. Li et al. (2016) investigated the shear behavior of jointed rock masses by DDARF, and the crack initial, extension, coalescence and the ultimate shear failure were totally investigated by a series of numerical analysis with echelon joints under different axial loadings. A hybrid finite discrete element method (FDEM) code was developed by Lishjak et al. (2014) to simulate the fracturing process during tunnel excavation in brittle rock masses, which provided an explicit consideration of crack initiation, propagation and coalescence.

Although laboratory test is an essential method to evaluate the fracture processes and failure behaviors of jointed rock masses, due to the difficulties in reproducing the joints in rock masses, there are only a few experimental tests on the deformation and failure behaviors of jointed rock masses. Kulatilake et al. (2001) conducted the uniaxial compression tests on the artificial rock-like material with various joint dip angles from 0° to 40°, and classified the failure mode into three types as tensile failure, shear failure and mixed type failure. A similar biaxial compression test with the joint dip angle of 30°, 45° and 60° was performed by Sagong et al. (2011) and it was found that the propagation direction of tensile cracks is normal to the joint angle and the model with lower joint angle generates a larger number of tensile cracks.

Although the influences of rock joints on the stability of underground structures have been studied analytically, numerically and experimentally, the failure mechanism of underground openings under gravity condition is still incomplete. Most of the former studies focused on the failure mechanism of rock masses around underground openings, and only a few studies quantitatively investigated the deformation of host rock masses. In the present study, the deformation and failure procedure around circular openings in jointed rock masses under gravity were investigated with artificial rock-like materials

utilizing a base friction test, and a series of numerical analysis were performed to investigate the effects of joint spacing, tunnel shape and tensile strength of rock-like materials on the deformation of host rock masses using an originally developed DEM code. These results might provide valuable guidance for the constructions of underground openings in jointed rock masses.

3.2 Experiment processes and numerical models

3.2.1 Mechanical Properties of Rock-like Models and Joint Sets

Base friction tests were applied on rock-like models with a series of joint sets. The artificial rock-like material used in the experiments was manufactured with a mixture of gypsum (Noritake Super Rock Ex), sand, water and retarder with a weight ratio of 2:3:0.83:0.02. The mechanical properties of rock-like material were tested by conducting the unconfined compression tests on cylindrical intact samples, and the results are tabulated in Table 3.1. Three examples that numbered from 1 to 3, respectively, were selected to illustrate the stress-strain relationships during unconfined compression tests as shown in Fig. 3.1.

Table 3.1 Physico-mechanical properties of the rock-like material.

Parameter	Symbols	Unit	Values
Density	ρ	g/cm3	1.81
Young's modulus	E	MPa	870.9
Compressive strength	σ_c	MPa	4.87
Possion's ratio	υ	--	0.18
Cohesion	c	MPa	0.68
Internal friction angle	φ	°	18.6
Tensile strength	σ_t	MPa	0.032

Table 3.2 Mechanical properties of joint sets.

Parameter	Symbols	Unit	Values
Shear stiffness	k_s	MPa/m	18
Normal stiffness	k_n	MPa/m	300
Cohesion	c	MPa	0
Internal friction angle	φ	°	31.2
Tensile strength	σ_t	MPa	0

Due to the low strength and brittleness of artificial rock blocks, the traditional shear test is not applicable, and an improved shear test apparatus as shown in Fig. 3.2 was adopted to investigate the shear behaviors of test models. In the improved test apparatus, the lower part of shear box is larger than the upper part, which guarantees that the contact between the lower and upper part keep constant during the shear procedure (Jiang et al., 2001). Two examples of direct shear test results are shown in Fig. 3.3 with the normal stresses of 0.19 MPa and 0.27 MPa, respectively. The rock-like blocks were casted separately and polished to ensure the smooth/flat surfaces of artificial rock joints, so that the values of cohesion and tension strength among the joint sets could be determined as 0. The mechanical properties of joint sets are listed in Table 3.2.

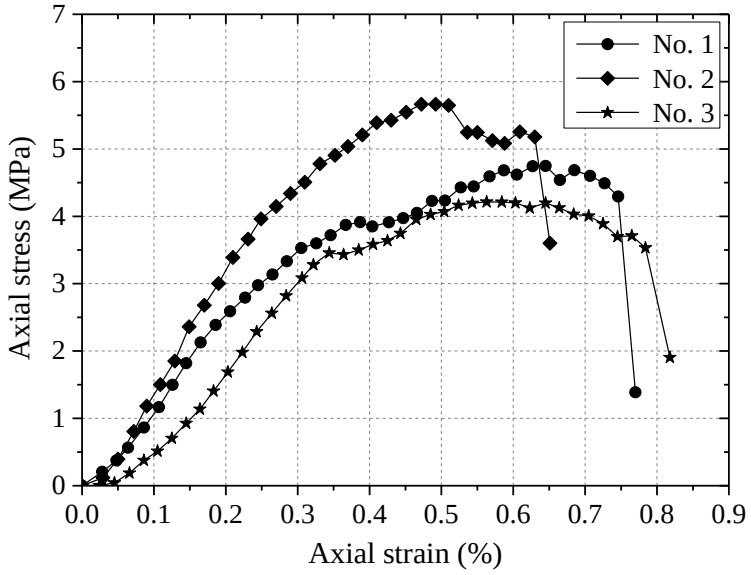

Fig. 3.1 Stress-strain relationships during unconfined compression tests.

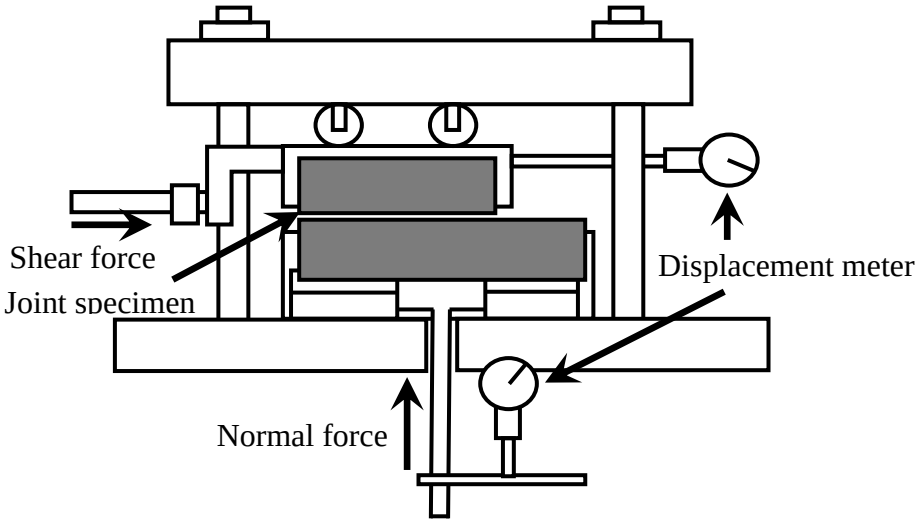

Fig. 3.2 The equipment of improved shear test.

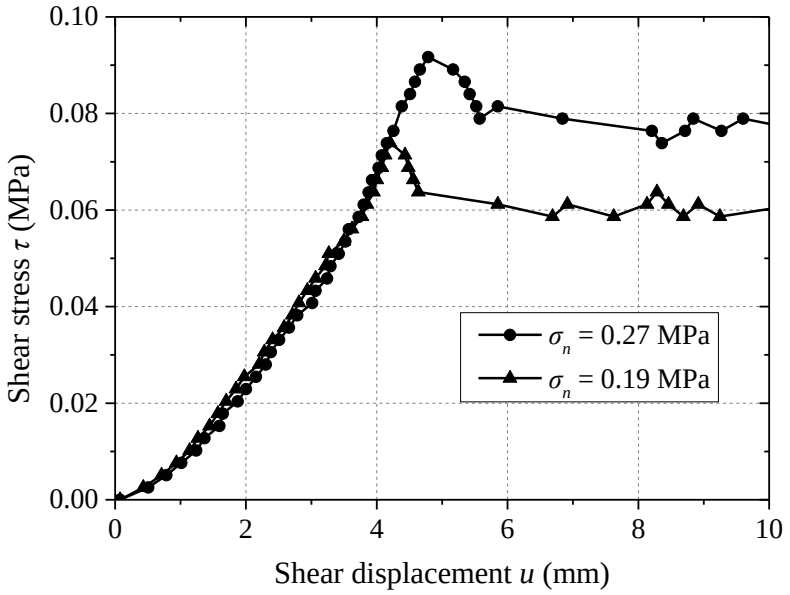

Fig. 3.3 Shear behaviors of artificial rock joints.

3.2.2 Specimen Preparation

The dimension of experimental specimen was 420 × 420 mm^2 with a thickness of 10 mm as shown in Fig. 3.4. The joint dip angles (α) of these specimens were selected as 30°, 45° and 60°, with a constant joint spacing (d) of 20 mm. The diameter of circular openings (D) was 85 mm.

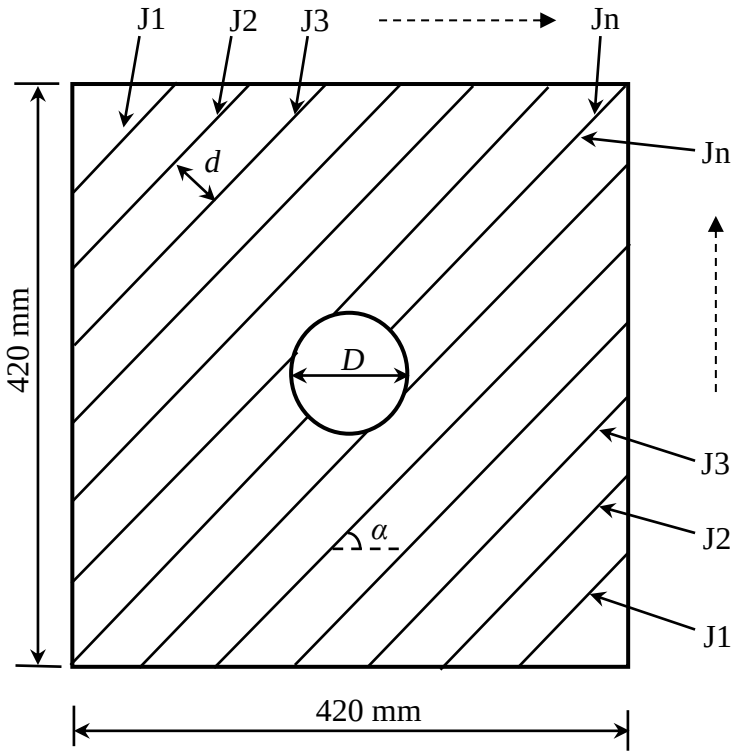

Fig. 3.4 Schematic view of experimental model.

The fabrication procedure for sample preparation is as follows: (i) the aggregate was mixed for 2 minutes by a mechanical agitator to make a full contact between materials; (ii) to ensure the generation of straight joint planers, steel strips were inserted into the rectangular mold at the position from J1, J2 to Jn (see Fig. 3.4), respectively. The angle between the strip and the horizontal direction was equal to the joint dip angle. (iii) the paste was poured into each closed domain generated by the rectangular mold

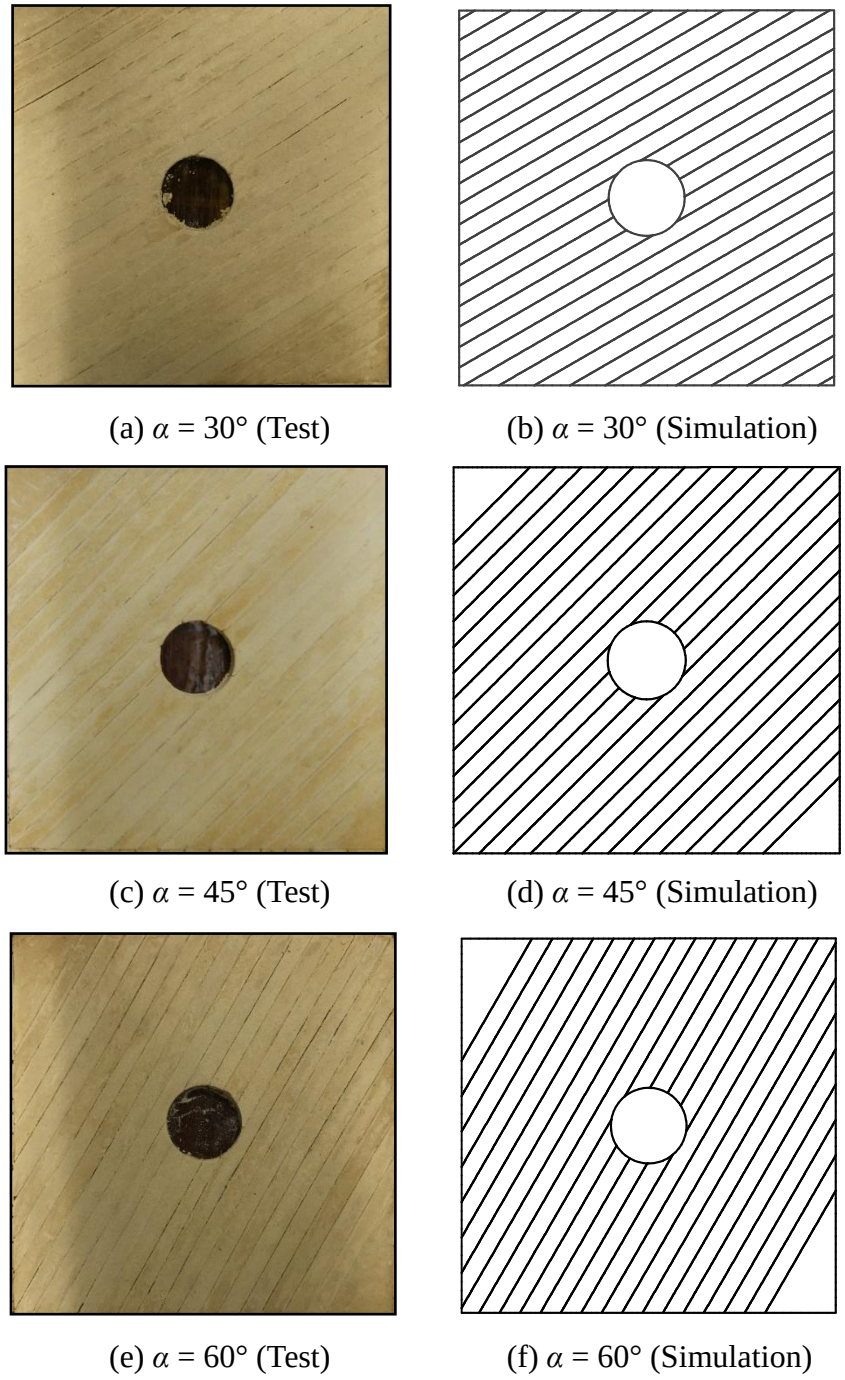

(a) α = 30° (Test) (b) α = 30° (Simulation)

(c) α = 45° (Test) (d) α = 45° (Simulation)

(e) α = 60° (Test) (f) α = 60° (Simulation)

Fig. 3.5 Artificial rock-like specimens and numerical models with various joint dip angles.

and the strips, with vibration for 1 min to minimize air bubbles inside the specimen. (iv) 5-10 minutes were necessary for the initial setting of paste, then, the strips were removed from the casted model and replaced by plastic films with a thickness of 0.1 mm to ensure the separation of each blocks. (v) the plastic films inserted between rock-like blocks were removed after 3 hours when the initial strength of paste was achieved, and the specimens were cured for 24 h with a room temperature of 25 ℃ and a humidity of 50%. The artificial rock-like specimens with various α are shown in the left column of Fig. 3.5.

3.2.3 Experimental Setup

Base friction technique is one of the typical testing methods for investigating the deformation and failure mechanism of rocks around underground openings (Bray and Goodman, 1981). In the present study, the base friction test apparatus as shown in Fig. 3.6 was developed, which employed a charge coupled device (CCD) camera to record the deformation and cracking process in rock mass models. The friction force was provided by removing the base stiff plate, with a changeable speed in the range of 0.1 - 10 mm/sec. An air pressure was applied vertically to the plate of base friction apparatus to change the frictional forces acting on the model. Noting that the upper surfaces of artificial rock blocks were polished to be flat before testing to ensure that the forces were uniformly distributed.

3.2.4. Principle of Base Friction Technique

Fig. 3.7 shows the principle of the base friction test apparatus, in which V is the movement velocity of base friction plate. With the removing of base stiff plate, a base friction force acting on the bottom of test model was applied in the horizontal plane (*xoz* plane). Under the gravity condition, the differential increment of base friction force dT could be determined as follows:

$$dT = \mu \times \gamma \times t \times dx \times dz \tag{3.1}$$

where μ is the friction coefficient between test model and base stiff plate, γ is the weight of artificial rock material (N/m^3), and t is the thickness of model (m).

When adding the air pressure, p_{air}, on the test model, Eq. (3.1) could be written as follows:

$$dT = \mu(\gamma \times t + p_{air}) \times dx \times dz \tag{3.2}$$

Giving that the model width in x direction is w (m), base friction force T at the depth of h could be determined in Eq. (3.3):

$$T = \mu \times (p_{air} + \gamma \times t) \times w \times h \tag{3.3}$$

Since P_{air} is much larger than T, Eq. (3.3) could be simplified as follows:

$$T = \mu \times p_{air} \times w \times h \tag{3.4}$$

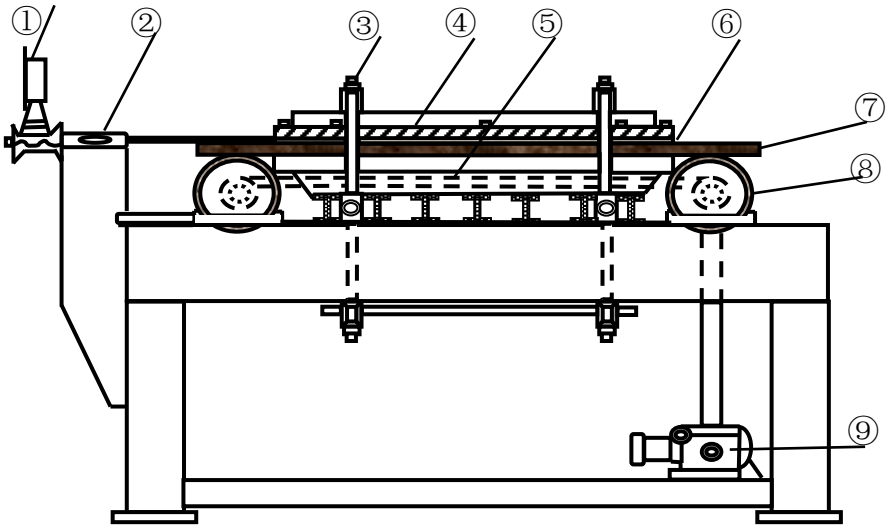

(a) Side view

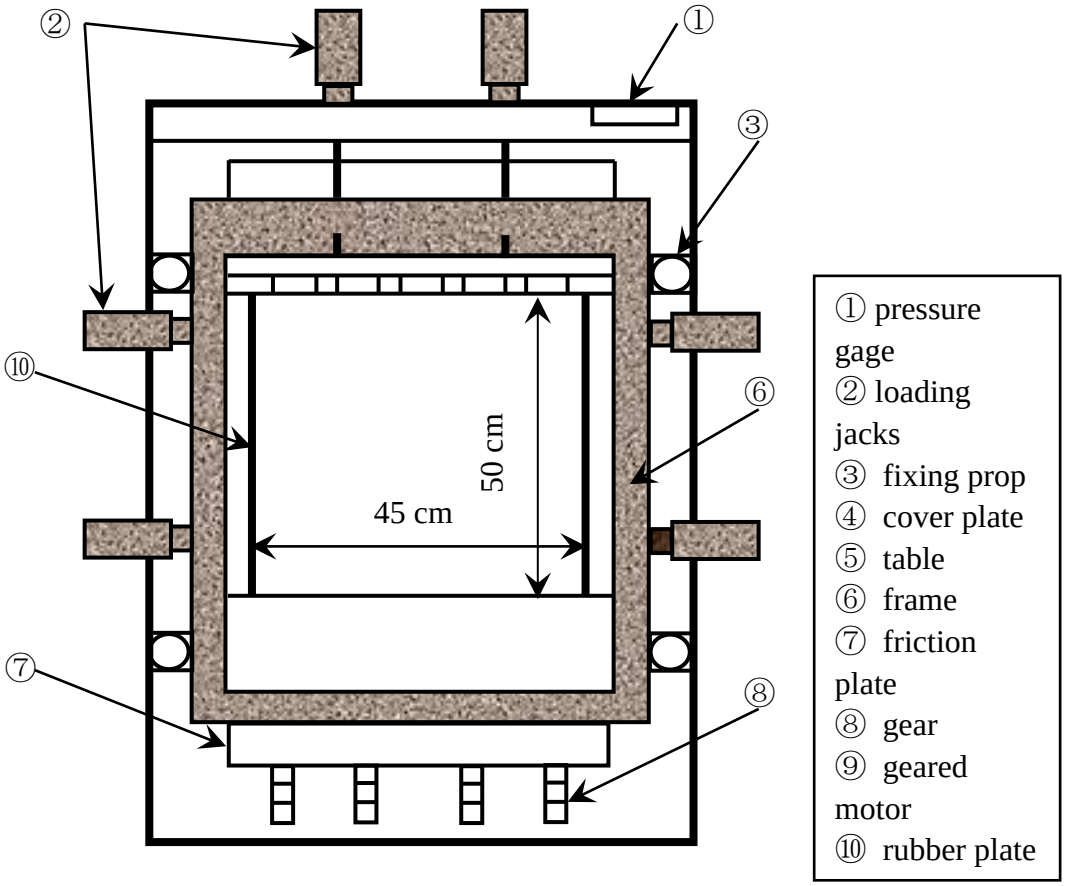

(b) Plane view

Fig. 3.6 The base friction test apparatus.

Correspondingly, the base friction stress σ_z at the depth of h in the test model is

$$\sigma_z = \frac{T}{w \times t} = \frac{\mu \times p_{air} \times h}{t} \tag{3.5}$$

The actual stress $\sigma_z^{'}$ vertically acting on the prototype model under the action of gravity is determined as below:

$$\sigma_z^{'} = \gamma' \times h_{act} \tag{3.6}$$

where γ' is the weight of prototype rock mass (N/m^3) and h_{act} is the actual depth in prototype (m).

According to the similarity laws, the geometric scale Λ and stress scale$\sum$ can be obtained as follows:

$$\Lambda = L / L_{act} \tag{3.7}$$

$$\sum = \sigma_c^{'} / \sigma_c = \sigma_z^{'} / \sigma_z \tag{3.8}$$

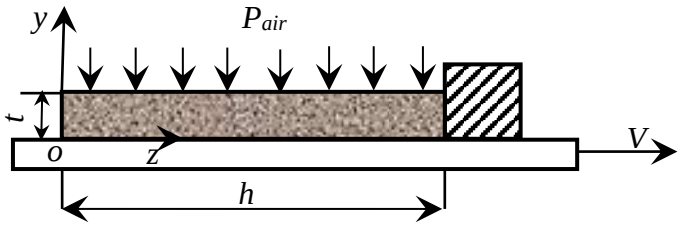

(a) Side view

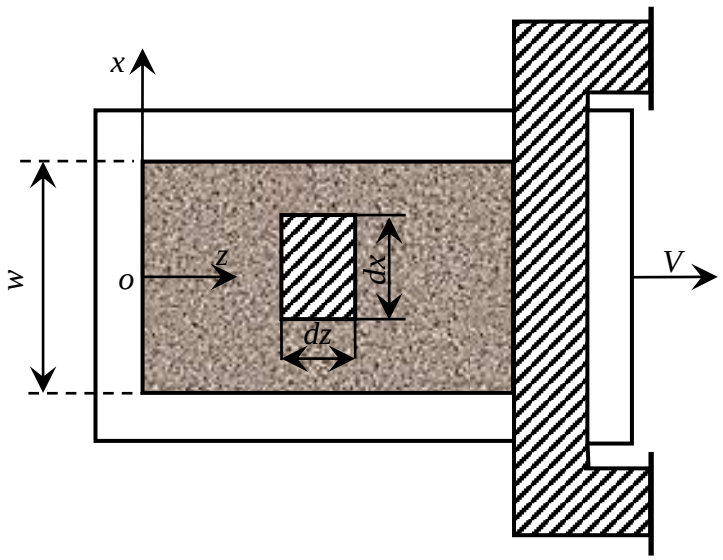

(b) Plane view

Fig. 3.7 The principle of the base friction test apparatus.

where L is the length of prototype (m), L_{act} is the length of test model (m), $\sigma_c^{'}$ and σ_c are the uniaxial compressive strength of prototype and test model (MPa), respectively.

Substituting Eqs. (3.7) – (3.8) into Eq. (3.4) yields:

$$p_{air} = \frac{t \times \gamma^{'} \times \Lambda}{\mu \times \Sigma} \tag{3.9}$$

Assumptions were made that the diameter of prototype tunnel D_p = 10.4 m, Λ = 122.35, $\sum$ = 1.11, and p_{air} = 0.012MPa.

3.2.5 Numerical Models

To quantitatively investigate the deformation and failure process in highly jointed rock masses around circular openings, an originally developed code based on the distinct element method (DEM) is developed, in which, the rock masses are treated as an assemblage of blocks separated by discontinuities, and these discontinuities are considered as the boundary conditions between blocks.

Two-dimensional numerical models with the same dimensions (420 × 420 mm^2) and joint distributions (location, dip angle and spacing) as the experimental models were established as shown in the right column of Fig. 3.5. During the simulations, the aperture of joint sets was not taken into accounts. The Mohr-Coulomb model was adopted to investigate the elastic/plastic deformation behaviors of artificial rock-like material with the properties as shown in Table 3.1, while the Coulomb slip model was adopted to present the deformation behaviors of joint sets with the properties as tabulated in Table 3.2. In accordance with the model test, the left and right sides of numerical models were considered as roller boundaries, and the bottom was fixed with no rotation and displacement, while the upper boundary was set free.

3.3 Comparisons between test and simulation results

Since the failure and deformation around an opening in jointed rock model were governed by tensile failure of weak rock masses (Sagong et al., 2011), it was reasonable to adopt the brittle artificial rock-like materials to evaluate the deformation and failure process in rock mass models. The cracking process observed during the model tests was mainly triggered by localized stress concentration and stress redistribution (Sagong et al., 2011, Jiang et al, 2009). To highlight the deformation behaviors around the circular opening, the enlarged views of model test results with the joint dip angles of 30°, 45° and 60° are depicted in the left column of Fig. 3.8. The main cracking directions of these three patterns are approximately 120°, 135° and 150°, respectively, which

demonstrates that the main propagation direction of newly generated cracks is perpendicular to the joint dip angle. The simulation results are shown in the right column of Fig. 3.8, where the red circle denotes the tensile failure and the green cross denotes the rock mass yielded in past. The distribution of newly generated cracks shows a similar tendency between model tests and numerical simulations. For joints with a low dip angle (α = 30°), the crack initiations are mainly confined in the regions near the left crown of circular openings as depicted in Figs. 3.8(a)-(b). For a moderate joint dip angle (α = 45°), the main cracks are generated near the left shoulder and right bottom side wall of circular openings as presented in Figs. 3.8(c)-(d). The models with a high joint dip angle (α = 60°) show a similar tendency with the moderate joint dip angle (α= 45°) pattern (see Figs. 3.8(e)-(f)). The tensile failure regions decrease with the increment of joint dip angle. It is concluded that the dip angle of joint sets in rock masses changes the failure mode around the opening. For a low joint dip angle (α = 30°), the failures are caused by the flexing and breaking of jointed blocks, and the deformation and failure around the openings are governed by the tensile strength of host rock masses. However, for rock masses with a high joint dip angle (α = 60°), the failure mode also couples with the sliding of rock blocks, which is controlled by the properties of discontinuities.

Heterogeneity of rock masses is one of the most important factors affecting the mechanical behaviors of rock masses during the fracture procedure (Wang et al., 2009). Although the test models were carefully manufactured, the heterogeneity of artificial rock-like material could not be totally eliminated, which could cause the discrepancy between model tests and numerical simulation results. Since the CCD camera can only capture the newly generated cracks on the upper surface of experimental models, microcracks generated in the interior of artificial rock blocks during test procedure could not be captured, which might be the main reason that the failure region in numerical results was larger than that in the model test results.

The model tests were focused on the deformation and failure process of a circular opening around by joint sets with various dip angles. The numerical analysis results agree well with the model test phenomenon, which indicates that the originally developed DEM code is suitable to investigate the deformation and failure characteristics of soft rock masses such as siltstone. Compared with the theoretical and experimental studies, numerical modeling method provides an economic, convenient and rapid way to study the deformation behavior around an underground opening. The numerical analysis also could help us investigate the explicit interpretation of test phenomenon and estimate the deformation behavior of host rock masses quantitatively. Therefore, in the following Section, a series of extended numerical models were established and parametric studies were performed to extensively investigate the effects

of joint spacing and tunnel shape on the deformation and failure behaviors of highly jointed host rock masses around the underground openings.

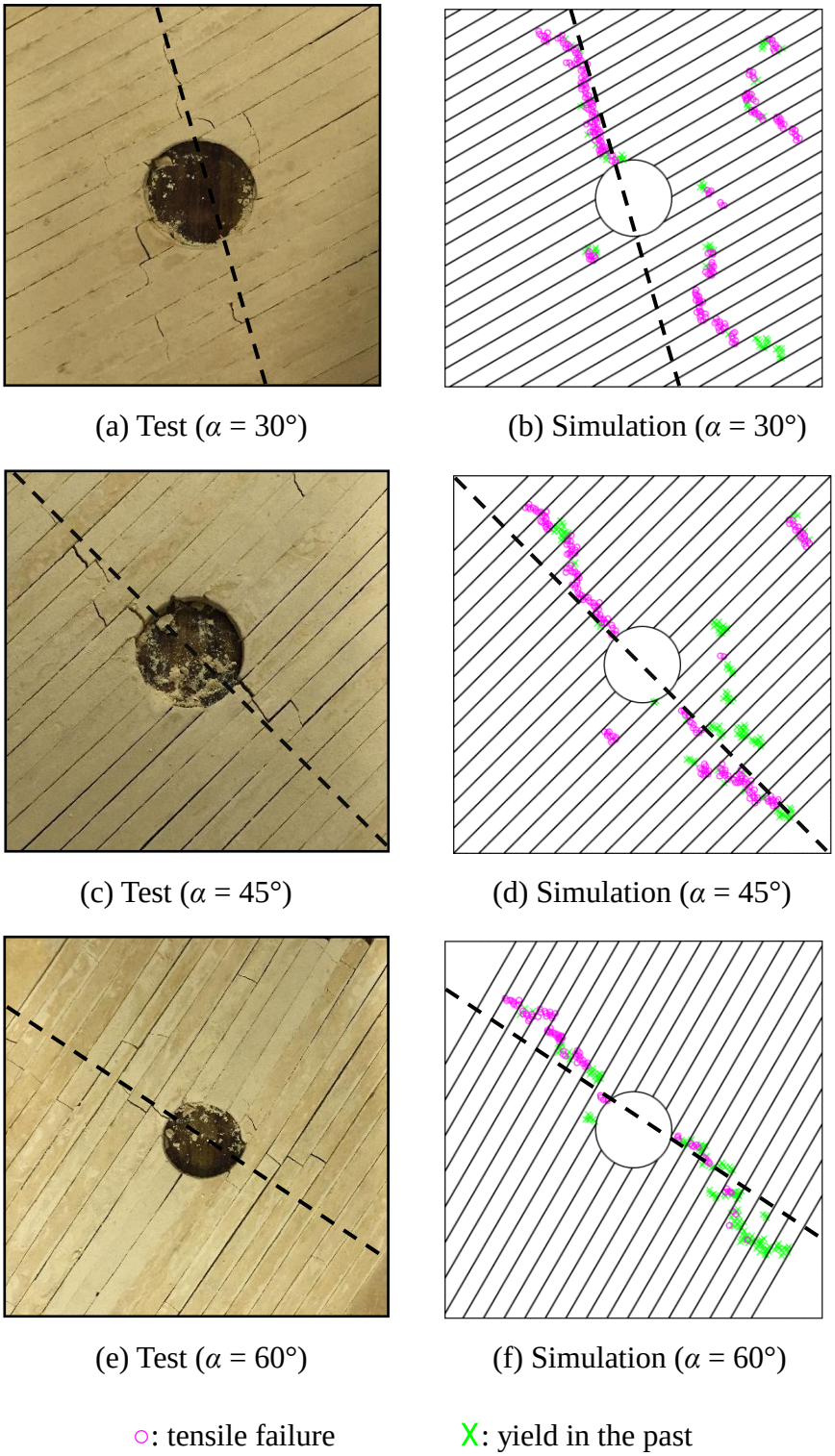

Fig. 3.8 Comparisons of crack propagations between model tests ((a), (c) and (e)) and numerical simulations ((b), (d) and (f)).

3.4 Parametric study

Five sets of joint spacing (10 mm, 20 mm, 30 mm, 40 mm and 60 mm) and three variably-shaped openings (circular, square and horseshoe) were considered. The effects of tensile strength on the crack propagation direction were investigated with the tensile strength of rock-like materials varied from 0.4 T to 10 T (T is the tensile strength of rock-like materials used in the base friction tests as shown in Table 3.1). The dimensions and boundary conditions were identical to those in Section 3.2. The diameter of the circular opening, the side length of the square opening and the maximum width of the horseshoe opening were all 82.5 mm, which is approximately 1/5 length of the whole model (420 mm). The configurations of the numerical model with different opening shapes are schematically depicted in Fig. 3.9.

3.4.1 Effect of Joint Spacing

The plastic zones with various joint spacing and dip angles are depicted in Fig. 3.10. For a low joint dip angle (α = 30°) with joint spacing of 10 mm and 20 mm (see Figs. 3.10(a) and (d)), the main propagation direction of newly generated cracks around the circular openings are approximately 120°. The remote cracks are initiated at a distance of 1.5 D (D is the diameter of circular tunnel) from the edge of opening, paralleling to the direction of the major cracks. The region of failure zones near the underground openings decreases with the increment of joint spacing as shown in Figs. 3.10(a), (d), (g) and (j). No tensile failure zone was observed when d > 40 mm (≈ 0.5 D). For a moderate joint dip angle (α = 45°) as shown in Figs. 3.10(b), (e), (h) and (k), all of the propagation directions of newly generated cracks are approximately 135°, meanwhile, the remote cracks are initiated at a distance of 2.0 D from the edge of circular opening. With the increment of joint spacing, the area of tensile failure zones around circular underground opening decreases, and the newly generated cracks only located at the right bottom of opening when d = 40 mm (see Fig. 3.10(k)). For a high joint dip angle (α = 60°) as depicted in Figs. 3.10(c) (f) (i) and (l), the major cracks are initiated at an approximate angle of 150° around the circular opening, with no remote cracks generated. Besides, when α = 60°, a smaller joint spacing of 10 mm leads to a growth of tensile failure zones at the right upper shoulder of underground opening (see Fig. 3.10(c)).

To investigate the influence of joint spacing on the deformation behavior of host rock masses around underground openings, eight key points were selected as the measuring points for each model as shown in Fig. 3.11. The displacements around the circular opening with various joint dip angles are depicted in Fig. 3.12. When the joint spacing is larger than 40 mm (≈ 1/2 D), the displacements around the underground openings are negligibly small. After a joint spacing of 40 mm is exceeded, the

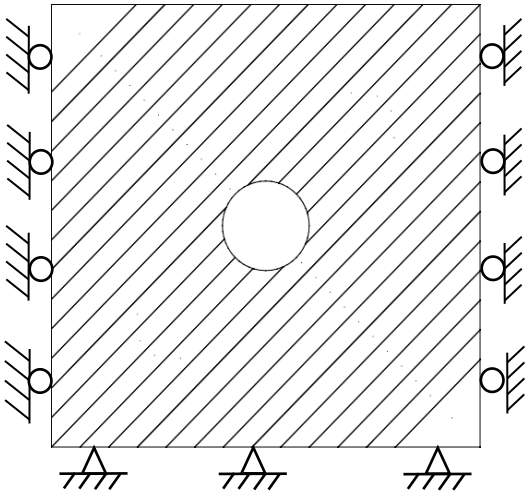

(a) Circular opening

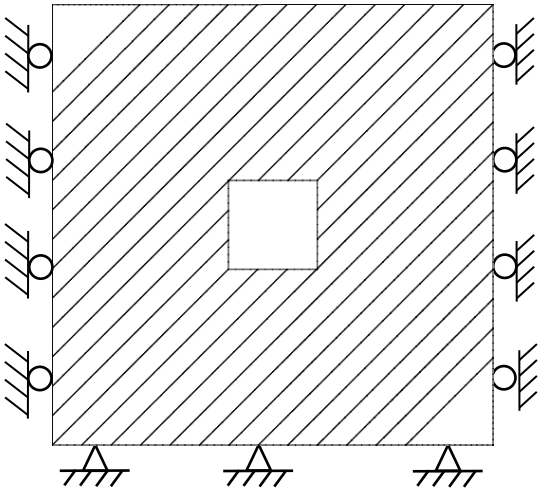

(b) Square opening

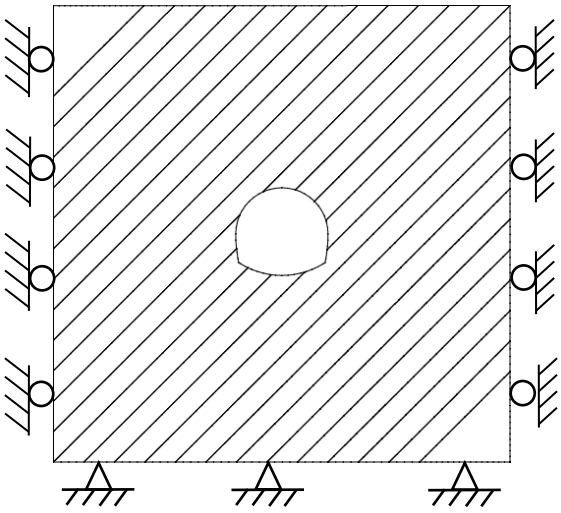

(c) Horseshoe opening

Fig. 3.9 Configurations of numerical model with variably-shaped openings.

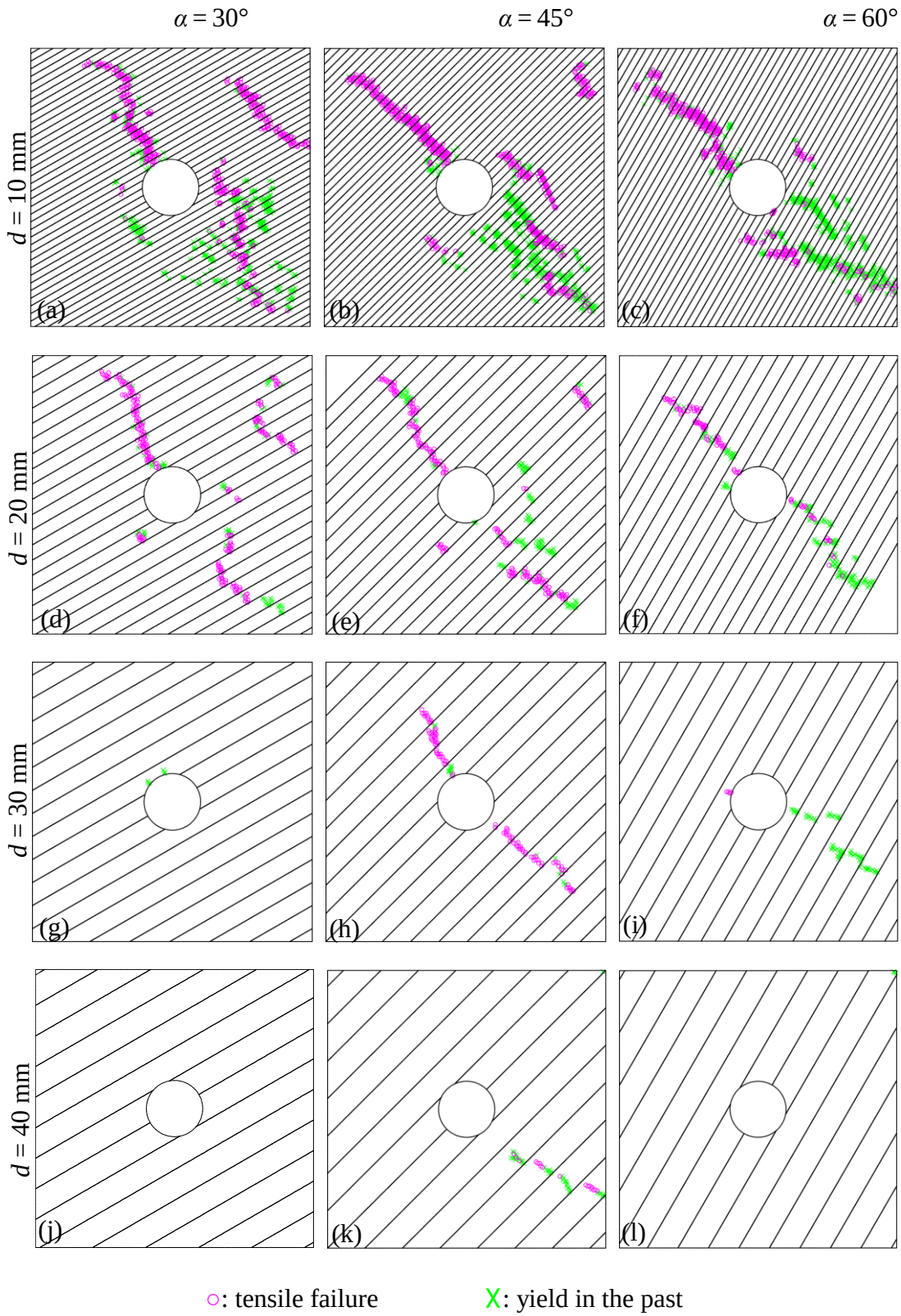

Fig. 3.10 Plastic failures of host rock masses with various joint spacing and dip angles (*d* is the joint spacing).

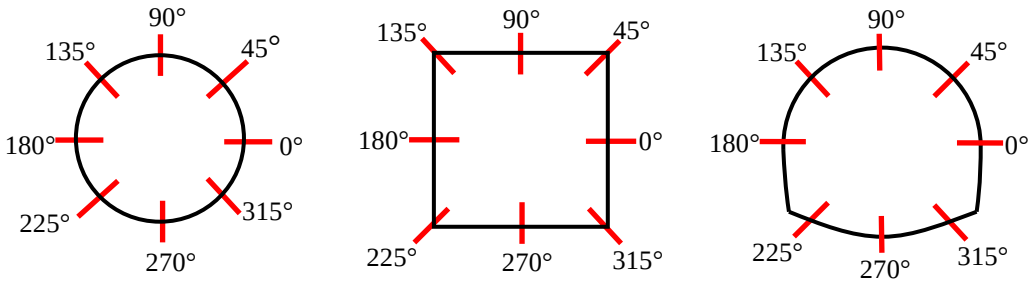

(a) Circular opening (b) Square opening (c) Horseshoe opening

Fig. 3.11 Measuring points around underground openings.

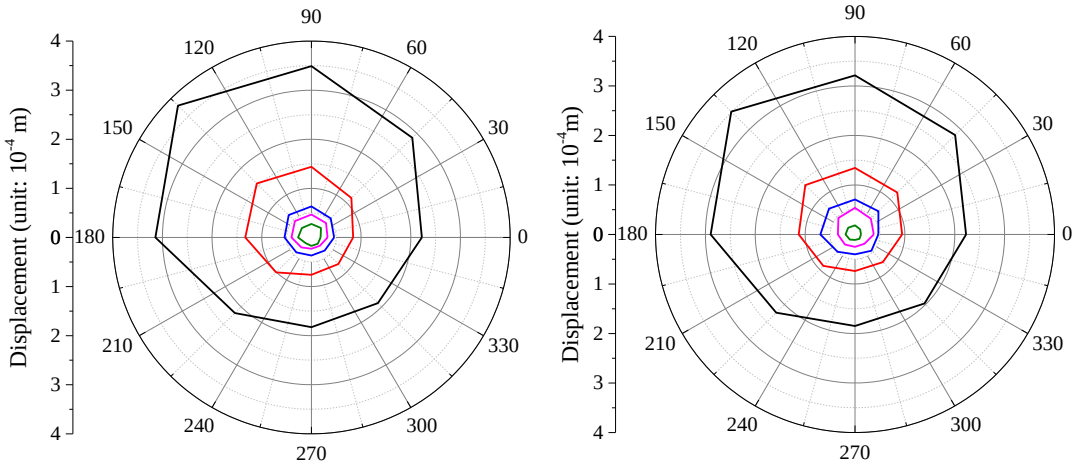

(a) α = 30° (b) α = 45°

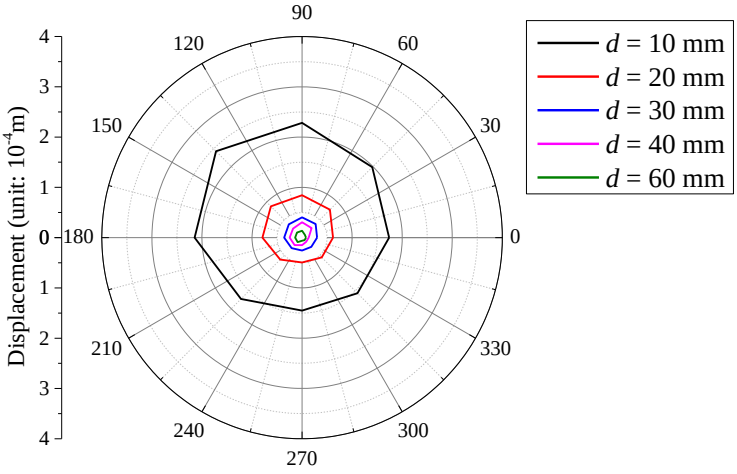

(c) α = 60°

Fig. 3.12 Displacements around circular openings.

displacements around the openings decrease dramatically. The numbers of intersections between the joints and underground openings are 18, 10, 6, 6 and 2 corresponding to the joint spacing of 10 mm, 20 mm, 30 mm, 40 mm and 60 mm, respectively. Since an increase in joint spacing leads to a dramatic decrease in the number of intersections between joints and underground openings, which might be the main reason that the displacements around the opening decrease dramatically when the $d > 1/2\ D$. The maximum displacement at the left shoulder of underground opening is about 1.8 – 2 times of the minimum displacements at the right side wall of openings for all the cases.

3.4.2 Effect of Opening Shape

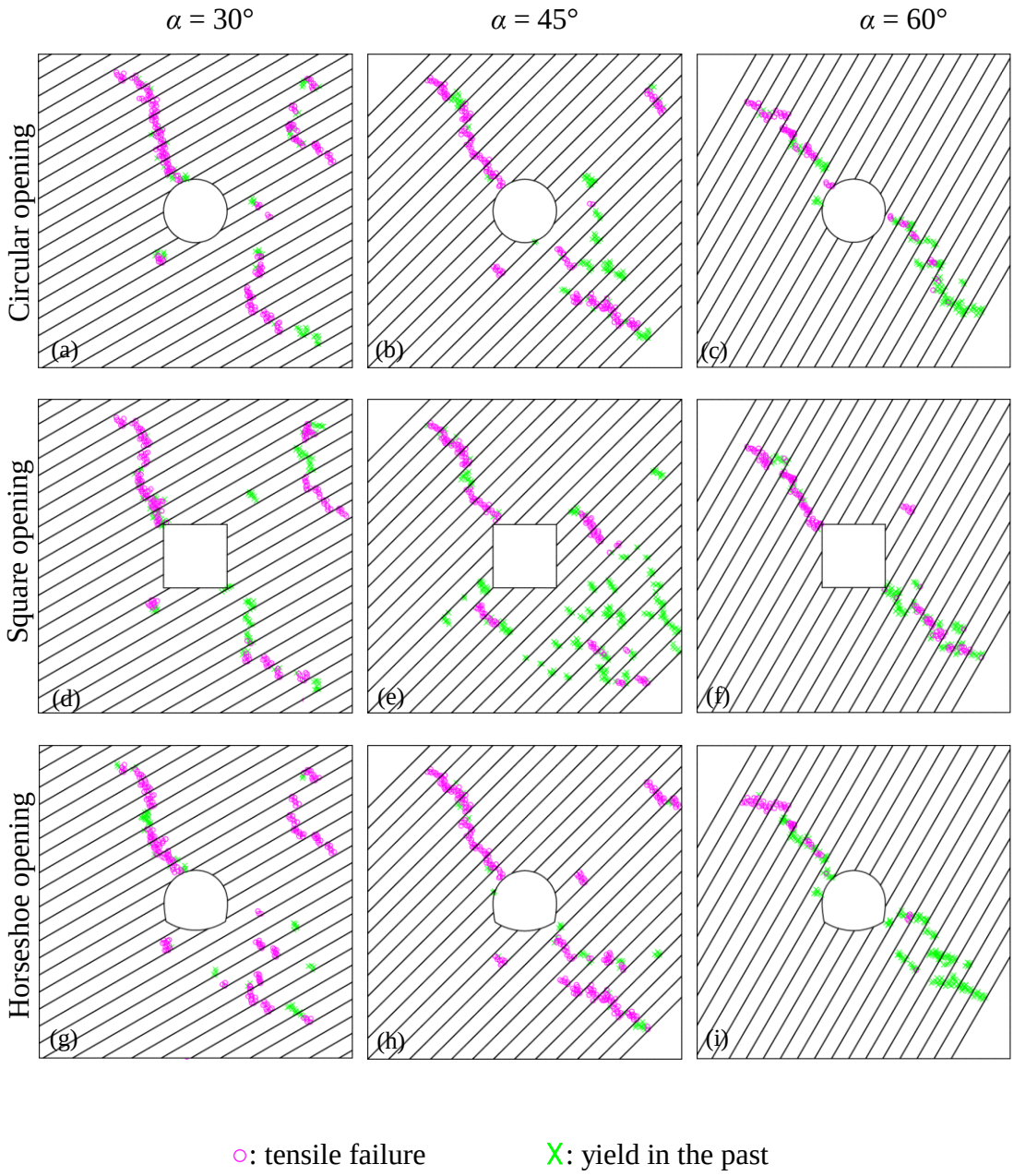

Fig. 3.13 Plastic failures of host rock masses with various underground opening shapes and joint dip angles.

The simulation results with the joint spacing of 20 mm and variably-shaped openings are shown in Fig. 3.13. The tensile failure in the zones located on the left upper side and right bottom side could be observed. Compared with the circular opening, a larger area of tensile failure zones is observed at the right upper and left lower side of the square opening due to the existence of sharp corners (see Figs. 3.13(d)-(f)). Figs. 3.13(g)-(i) show the plastic failures of host rock masses around horseshoe opening with different joint dip angles. Stress concentration occurs at the right bottom side of underground opening when α = 60°. The influence of opening shape on the main propagation direction of newly generated cracks could be negligible. For a further study of highly jointed rock mass deformations around variably-shaped openings, the displacements at different measuring points are concluded in Fig. 3.14. For a low joint dip angle (α = 30°), the maximum displacement occurs at the left shoulder of underground opening. A larger displacement around the square opening is observed compared with the others, and no obvious discrepancy could be observed between

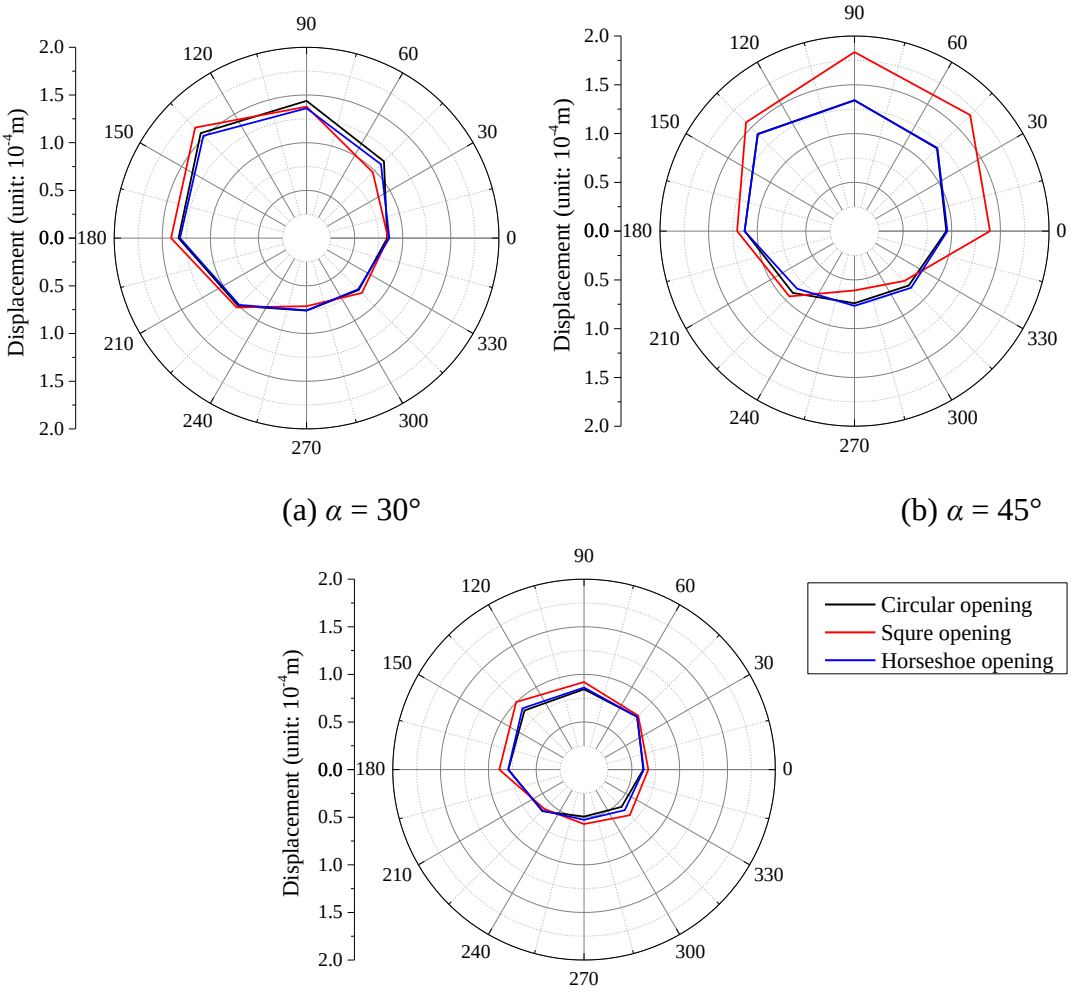

(a) α = 30° (b) α = 45°

(c) α = 60°

Fig. 3.14 Displacements around underground openings with various shapes.

circular and horseshoe openings (see Fig. 3.14(a)). For a moderate joint dip angle (α = 45°), the displacements at the crown and right shoulder of square opening are about 1.4 times of those around the other two opening shapes (see Fig. 3.14(b)), which are triggered by the stress concentration at the sharp corners of square opening and the overlay of tensile and slipping failures of rock masses. For a high joint dip angle (α = 60°), displacement around square opening is larger than that around the square/horseshoe opening (see Fig. 3.14(c)).

3.4.3 Effect of tensile strength

The plastic zones with various tensile strengths and joint dip angles are shown in Fig. 3.15. The region of failure zones near the underground openings decreases with the increment of tensile strength. Since no tensile failure zone is observed when the tensile strength is larger than 1.4 T, only the results with the tensile strength of 0.4 T, 0.6 T, 1.0 T and 1.2 T are plotted (T is the tensile strength of rock-like materials used in the base friction tests as shown in Table 3.1). Although the main propagation directions of newly generated cracks around the circular openings are approximately perpendicular to the joint dip angles, slight variations of the main propagation direction are observed as shown in Fig. 3.15. The correlations between the tensile strength and the main propagation direction of newly generated cracks are plotted in Fig. 3.16. Herein, β means the obtuse angle between horizontal and the main propagation direction of newly generated cracks as depicted in Fig. 3.16(a). For a low (α = 30°) or moderate joint dip angle (α = 45°) as shown in Fig. 3.16(b), β decreases with the increment of tensile strength. For a high joint angle (α = 60°), the influences of tensile strength on the main propagation direction of newly generated cracks could be negligible.

3.5 Summaries and conclusions

In this study, base friction tests were conducted to investigate the influences of joint dip angle on the stability of underground openings in highly jointed rock masses. A series of numerical simulations using the originally developed DEM code were performed based on the experiment-based and extended numerical models. The results indicate that both the joint spacing and opening shape have great impacts on the deformation of host rock masses around underground openings. Based on the model tests carried out and numerical analysis performed, the following conclusions are drawn:

(1) The main propagation direction of newly generated cracks are approximately perpendicular to the joint dip angles. For the brittle rock with a low joint dip angle (α = 30°), the failure of host rock masses is given rise to the flexing and creaking of layer

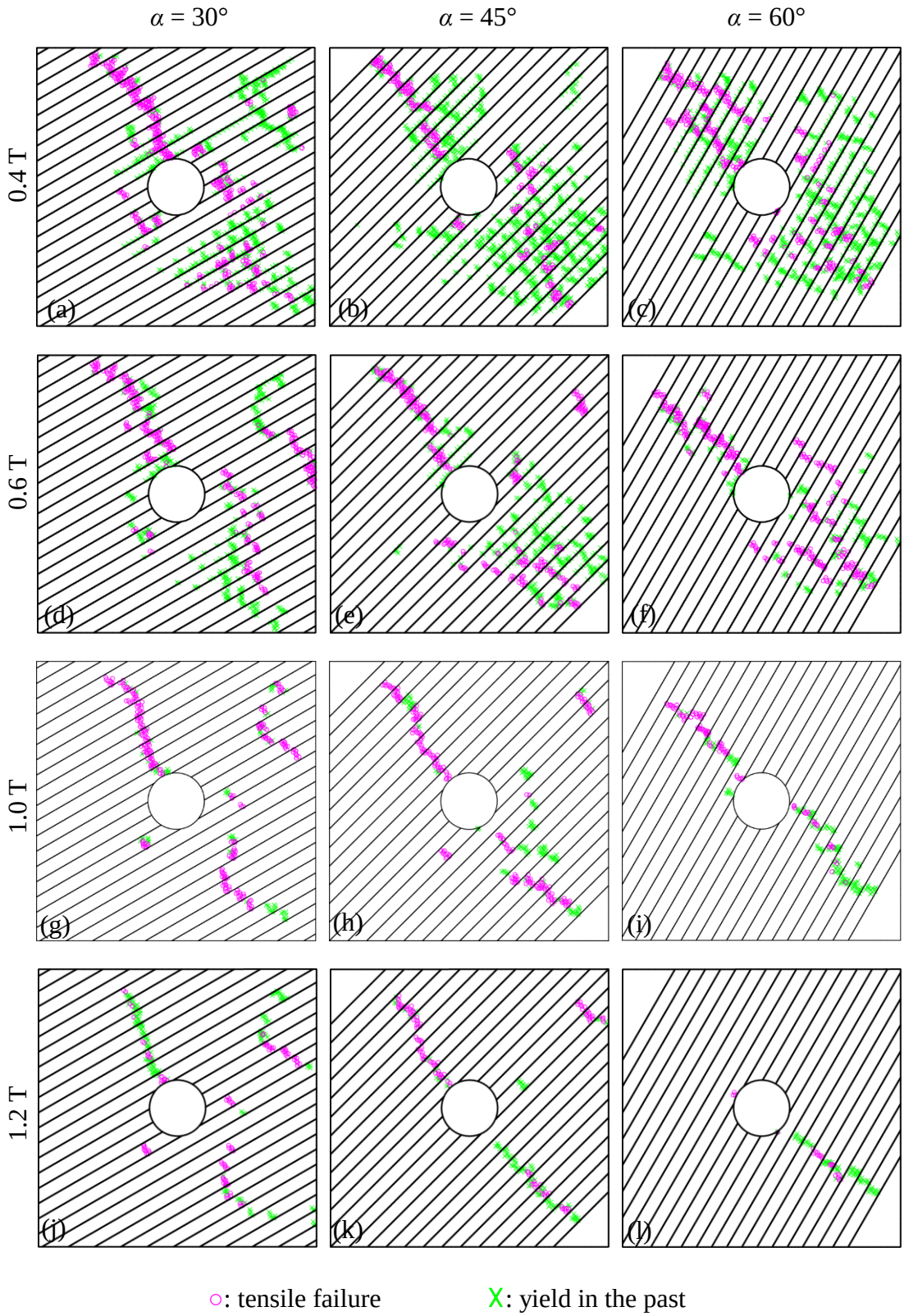

Fig. 3.15 Plastic failures of host rock masses with various tensile strengths and joint dip angles (T is the tensile strength of rock-like materials used in the base friction tests as shown in Table 3.1).

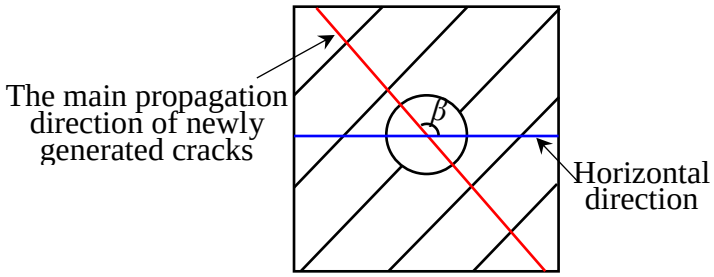

(a) The obtuse angle β between horizontal and the main propagation direction of newly generated cracks

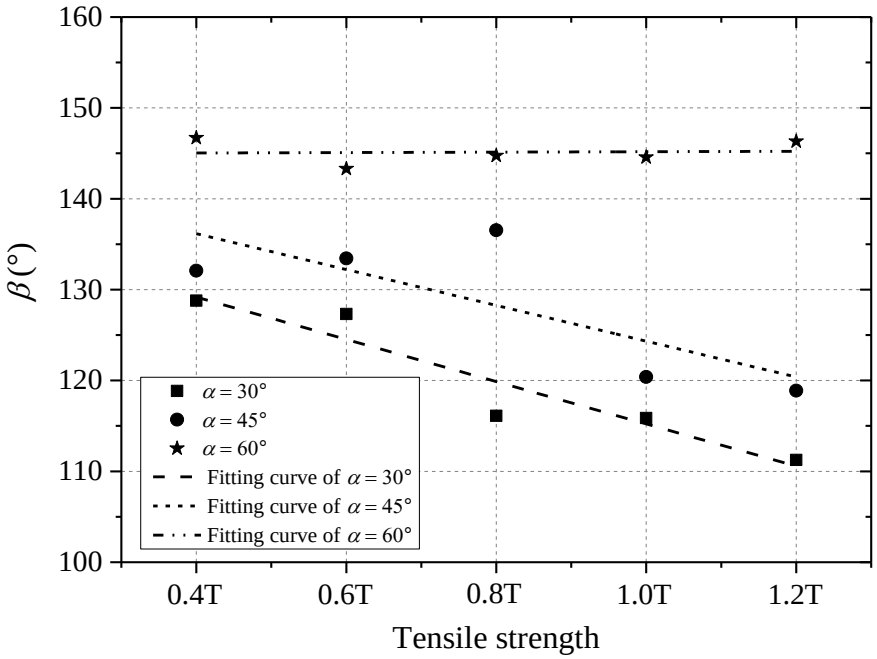

(b) Correlations between tensile strength and β

Fig. 3.16 Crack propagation directions with various tensile strengths and joint dip angles.

blocks, and the deformation and failure around the underground openings are generally governed by the tensile strength of host rock masses. Besides, for a moderate (α = 45°) or high joint dip angle (α = 60°), sliding of rock masses also plays an important role on the deformation of rock masses.

(2) The remote cracks are initiated at a certain distance of 1.5 – 2.0 D from the edge of underground opening with a low (α = 30°) or moderate (α = 45°) joint dip angle, where D is the diameter of circular underground opening. When a joint angle of 60° is exceeded, no remote crack could be observed around the underground opening. The maximum displacement at the left shoulder of tunnel is almost 1.8 – 2 times of the minimum displacement at the right side wall of underground opening.

(3) When the joint spacing is equal to or larger than 0.5 times of diameter of circular opening, the deformation around the underground openings is negligibly small.

(4) The influence of opening shapes on the main propagation direction of newly generated cracks could be negligible. Compared with the circular/horseshoe opening, a larger area of tensile failure zones are observed around the square opening due to the existence of sharp corners. For a moderate joint dip angle, the displacement around the square opening is remarkable due to the stress concentration at the sharp corners and the overlay of tensile and slipping failures.

(5) The main propagation direction of newly generated cracks is influenced by the tensile strength of rock-like materials. For a low (α = 30°) or moderate joint dip angle (α = 45°), the obtuse angle between the main propagation direction of newly generated cracks and the horizontal decreases with the increment of tensile strength. While for a high joint dip angle (α = 60°), the effects of tensile strength on the main propagation direction of newly generated cracks could be negligible.

References:

Brady B and Brown H G. Rock mechanics for underground mining. Kluvier Academic Publishers, Netherland, 2004, 628 p.

Bray J W and Goodman R E. The theory of base friction models. International Journal of Rock Mechanics and Mining Sciences & Geomechanics Abstracts, 1981, 18, 453-468.

Cai M, Kaiser P K and Martin C D. A tensile model for the interpretation of microseismic events near underground openings. Pure and applied geophysics, 1998, 153, 67-92.

Cai M, Kaiser P K, Tasaka Y, Maejima T, Morioka H, and Minami M. Generalized crack initiation and crack damage stress thresholds of brittle rock masses near underground excavations. International Journal of Rock Mechanics and Mining Sciences, 2004, 41, 833-847.

Chappell B A. Deformational response in discontinua. International Journal of Rock Mechanics and Mining Sciences & Geomechanics Abstracts, 1979, 16, 377-90.

Cundall P A and Hart R D. Numerical modelling of discontinua. Engineering computations, 1992, 9, 101-113.

Dershowitz W S and Einstein H H. Characterizing rock joint geometry with joint system models. Rock Mechanics and Rock Engineering, 1988, 21, 21-51.

Goodman E R and Shi G. Block Theory Application to Rock Engineering. Prentice-Hall, Englewood Cliffs, NJ, 1985, 338 p.

González-Palacio C, Menéndez-Díaz A, Álvarez-Vigil A E and González-Niciezaa C. Identification of non-pyramidal key blocks in jointed rock masses for tunnel excavation. Computers and Geotechnics, 2005, 32, 179-200.

Hammah R E, Yacoub T, Corkum B and Curran J.H. The practical modelling of discontinuous rock masses with finite element analysis. The 42nd US Rock Mechanics Symposium (USRMS), San Francisco, 2008, June 29-July 2, Document ID: ARMA-08-180.

Hao Y H and Azzam R. The plastic zones and displacements around underground openings in rock masses containing a fault. Tunnelling and underground space technology, 2005, 20, 49-61.

Jia P and Tang C A. Numerical study on failure mechanism of tunnel in jointed rock mass. Tunnelling and Underground Space Technology, 2008, 23, 500-507.

Jiang Y, Xiao J, Yamaguchi K, Tanabashi Y and Esaki T. Behaviour and Support Design of Large Underground Opening in Discontinuous Rock Masses. JOURNAL-MINING AND MATERIALS PROCESSING INSTITUTE OF JAPAN, 2001, 117, 639-644.

Jiang Y, Tanabashi Y, Li B and Xiao J. Influence of geometrical distribution of rock joints on deformational behavior of underground opening. Tunnelling and underground space technology, 2006, 21, 485-491.

Jiang Y, Li B and Yamashita Y. Simulation of cracking near a large underground cavern in a discontinuous rock mass using the expanded distinct element method. International Journal of Rock Mechanics and Mining Sciences, 2009, 46, 97-106.

Jiao Y Y, Zhang X L, and Zhao, J., 2012, Two-dimensional DDA contact constitutive model for simulating rock fragmentation. Journal of Engineering Mechanics ASCE, 138,199-209.

Jiao Y Y, Zhang H Q, Zhang X L, Li H B and Jiang Q H. A two‐dimensional coupled hydromechanical discontinuum model for simulating rock hydraulic fracturing. International Journal for Numerical and Analytical Methods in Geomechanics, 2015, 39, 457-481.

Jing L and Hudson J A. Numerical methods in rock mechanics. International Journal of Rock Mechanics and Mining Sciences, 2002, 39, 409-427.

Kulatilake PHSW, Wang S and Stephansson O. Effect of finite-size joints on the deformability of jointed rock in 3-dimensions. International Journal of Rock Mechanics and Mining Sciences & Geomechanics Abstracts, 1993, 30, 479-501.

Kulatilake P, Malama B, and Wang J. Physical and particle flow modeling of jointed rock block behavior under uniaxial loading. International Journal of Rock Mechanics and Mining Sciences, 2001, 38, 641-657.

Li Y, Zhou H, Zhu W, Li S C and Liu J. Experimental and numerical investigations on the shear behavior of a jointed rock mass. Geosciences Journal, 2016, 1-9.

Lisjak A, Figi D and Grasselli G. Fracture development around deep underground excavations: Insights from FDEM modelling. Journal of Rock Mechanics and Geotechnical Engineering, 2014,6, 493-505.

Lu J. Systematic identification of polyhedral rock blocks with arbitrary joints and faults. Computers and Geotechnics, 2002, 29, 49-72.

Martino J B and Chandler N A. Excavation-induced damage studies at the underground research laboratory. International Journal of Rock Mechanics and Mining Sciences, 2004, 41, 1413-1426.

Sagong M, Park D, Yoo J and Lee J S. Experimental and numerical analyses of an opening in a jointed rock mass under biaxial compression. International Journal of Rock Mechanics and Mining Sciences, 2011, 48, 1055-1067.

Shen B and Barton N. The disturbed zone around tunnels in jointed rock masses. International Journal of Rock Mechanics and Mining Sciences, 1997, 34, 117-125.

Solak T. Ground behavior evaluation for tunnels in blocky rock masses. Tunnelling and Underground Space Technology, 2009, 24, 323-330.

Tang C A. Numerical simulation of progressive rock failure and associated seismicity. International Journal of Rock Mechanics and Mining Sciences, 1997, 34, 249-261.

Tang C A, Yang W T, Fu Y F and Xu X H. A new approach to numerical method of modelling geological processes and rock engineering problems—continuum to discontinuum and linearity to nonlinearity. Engineering Geology, 1998, 49, 207-214.

Tang C A, Liu H, Lee P K K, Tsui Y and Tham L G. Numerical studies of the influence of microstructure on rock failure in uniaxial compression—part I: effect of heterogeneity. International Journal of Rock Mechanics and Mining Sciences, 2000, 37, 555-569.

Tang C A, Tham L G, Lee P K K, Tsui Y and Liu H. Numerical studies of the influence of microstructure on rock failure in uniaxial compression—part II: constraint, slenderness and size effect. International Journal of Rock Mechanics and Mining Sciences, 2000, 37, 571-583.

Timoshenko S and Goodier J N. Theory of Elasticity. McGraw-Hill Book Company. Inc., New York, 1951, 506 p.

Wang S H, Lee C I, Ranjith P G and Tang C A. Modeling the effects of heterogeneity and anisotropy on the excavation damaged/disturbed zone (EDZ). Rock mechanics and rock engineering, 2009, 42, 229-258.

Zhu W C, Liu J, Tang C A, Zhao X D, and Brady B H. Simulation of progressive fracturing processes around underground excavations under biaxial compression. Tunnelling and Underground Space Technology, 2005, 20, 231-247.

CHAPTER 4

Deformation and mechanical characteristics of tunneling in squeezing ground: a case study of the west section of the Tawarazaka Tunnel in Japan

4.1 Introduction

Ground squeezing generally occurs during the construction of tunnels through weak rock strata. The main characteristics of ground squeezing, such as high deformability, low shear strength, and a high in situ stress state, can affect tunneling performance, delay projects and increase costs due to remedial actions (Mezger et al., 2013). Therefore, understanding the squeezing characteristics of ground is a crucial issue for the design of a stable support system of tunnels.

Previous theoretical and numerical studies have been performed to analyze the squeezing characteristics of the ground, and practical experiences have been considered. Saari (1982) suggested that the intensity of the tangential strain of a tunnel be used as a parameter to evaluate the squeezing degree of ground and proposed closed form solutions for some special cases by considering the squeezing phenomenon an elasto-visco-plastic behavior of rocks. Tanimoto (1984) treated the ground as an elasto-plastic material following the strain-softening constitutive law to evaluate the degree of squeezing of rocks and suggested that squeezing would occur when the rock is strained to its residual flow state. Aydan et al. (1993) accounted for experiences acquired via squeezing rocks in Japan and found that squeezing occurs if the competence factor, which is the ratio of the uniaxial compressive strength of intact rock to the overburden pressure, is less than 2.0. Kovári et al. (1996) suggested that the low strength and high deformability of rocks, as well as the pore pressure of water, could facilitate ground squeezing and found that the following rock types are specifically prone to developing large pressures and deformation: altered gneiss, shale, phyllite, schist, clay, mudstone and tuff. Hoek et al. (2002a, b) proposed a semi-analytical method to estimate potential tunnel squeezing and suggested that the ratio of the uniaxial compressive strength of a rock mass to the in situ stress could be used as an indicator of tunnel ground squeezing. Hamidi et al. (2008) assessed the maximum radial displacement to determine the squeezing characteristics of the ground in Nasoud tunnel by utilizing the Fast Lagrangian Analysis of Continua (FLAC) two-dimensional code and proposed some

preventive measures to mitigate the potential for squeezing problems. Hoek et al. (2009) presented a case history of Yacambú-Quibor tunnel, which experienced severe squeezing problems during construction, to illustrate the different mechanisms of support system failure and found that these mechanisms are related to the installation sequence of different support components. Barla (2009) discussed the recent innovations in yield–control support systems applied to conventional tunneling in difficult ground conditions associated with squeezing, and some measures that have been applied to address the squeezing conditions encountered during excavation in the Carboniferous formation were studied based on a case study of the Saint Martin access adit along the Base Tunnel of the Lyon–Turin railway link. Jimenez et al. (2011) proposed a novel empirical method for predicting the squeezing characteristics in rock tunnels based on the application of the theory of linear classifiers to an extensive database of well-documented squeezing cases from tunnels in the Himalayas and Himalayan foothills. This method was used to calculate the probabilities of squeezing for different combinations of tunnel depth and rock mass quality, and the analysis results showed that the probability of squeezing significantly increases with depth and is mainly affected by the quality of the rock mass. Bilgin et al. (2012) studied the squeezing characteristics of the ground in the Uluabat Tunnel based on a detailed Tunnel Boring Machine (TBM) performance analysis and found that overburden, rock mass rating (RMR) values, the increase in machine thrust for a given tunnel length and time, and the variation in the torque/thrust ratio could be utilized by practicing engineers to implement mitigation measures. Mezger et al. (2013) suggested that the frequently observed phenomenon of squeezing variability could be tracked back to different degrees of shearing, different schistosity orientations and the influences of nearby weaker or stronger zones. A simple empirical equation that can address the effect of shearing and schistosity reasonably well and provide reliable indications of squeezing intensity was proposed.

The objective of the present study is to identify the factors that may have significant influences on the convergence of the west section (WS) of the Tawarazaka Tunnel. These factors can be selected as indicators during tunnel construction in squeezing ground. First, a concise overview of the available relevant data, geology, excavation and support methods is provided (Section 4.2). Second, the correlations between the in situ measured convergences and the geological characteristics such as overburden, initial horizontal stress ratio and rock quantities are discussed (Section 4.3). Third, a two-dimensional numerical analysis based on the geological distribution is performed to investigate the factors that influence the induction of ground squeezing in the WS. The effects of bedding joint stiffness, internal friction angle of bedding joints, moduli of rock masses and overburden on tunnel deformation in the WS were

analyzed (Section 4.4). Finally, the deformation mechanism of rocks in the WS of the Tawarazaka Tunnel is discussed, and conclusions are presented.

4.2 General description of construction project

4.2.1 Location of Tawarazaka Tunnel

The 5675-m long Tawarazaka mountain tunnel is the major construction portion of the Kyushu Shinkansen West Kyushu route project, which crosses Saga Prefecture and Nagasaki Prefecture in Japan, as shown in Fig. 4.1. The purpose of this project is to reduce the travel time between the cities of Fukuoka and Nagasaki and create a fast and comfortable transportation route. The excavation region was divided into the east section (ES) and WS based on the geological conditions, as illustrated in Fig. 4.2, based on the chainages of 11 km 755 m – 14 km 400 m and 14 km 400 m – 17 km 430 m, respectively. Since ground squeezing has mainly occurred in the WS, the present study focuses on the deformation in this section.

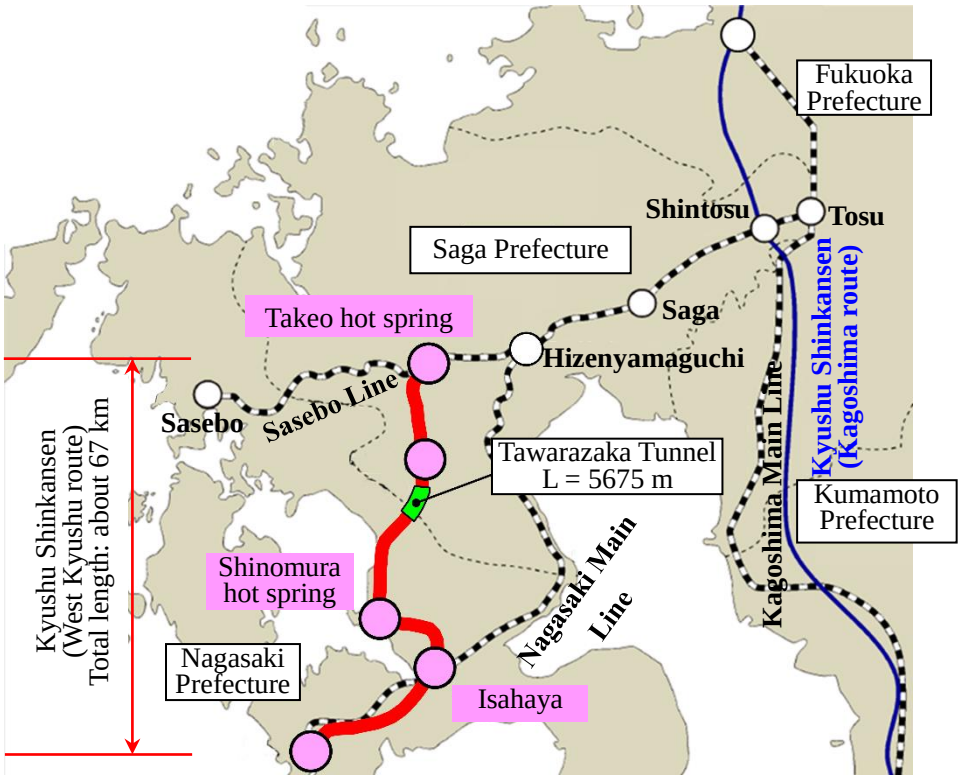

Fig. 4.1 Location of the Kyushu Shinkansen West Kyushu route project.

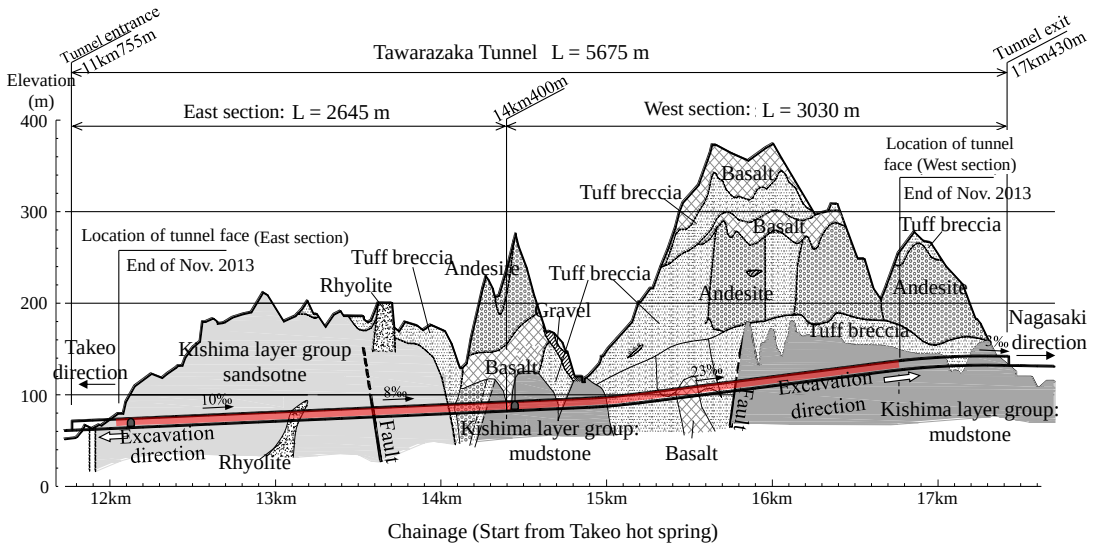

Fig. 4.2 Longitudinal geological section of the Tawarazaka Tunnel.

4.2.2 General geological setting

The main rock formation in the WS of the Tawarazaka Tunnel is composed of mudstone that formed in the Paleogene Period and underlain is by volcanic sediments that were developed in the Neogene and Quaternary Periods. Fig. 4.2 shows a longitudinal geological section of the ground formations together with the location of the WS of the Tawarazaka Tunnel. In the WS, excavation was performed at an elevation of approximately 60 m ~ 130 m, and the maximum overburden depth was observed in the chainages from 15 km 700 m to 16 km 100 m. A large regional fault was encountered in this section, and the overall strength of rocks was decreased by the development of cracks and rock slacking.

4.2.3 Construction method

The typical New Austrian Tunneling Method (NATM) with a mini-bench, as shown in Fig. 4.3, was adopted during the construction of the Tawarazaka Tunnel. The role of the mini-bench was to ensure the self-supporting capacity of rocks. The tunnel section was divided into three parts: the top heading, lower bench and invert. The length of the top heading was 4 ~ 8 m based on the geological conditions of the surrounding rock masses, and the lengths of the lower bench and invert were 2 m and 4 m, respectively. Steel beams spaced at 1.0 m were used to reduce the rock pressure caused by excavation. Shotcrete and rock bolts were installed behind the tunnel face after bench excavation was completed. The representative support patterns are given in Table 4.1, and Fig. 4.4 shows the information regarding the primary support systems.

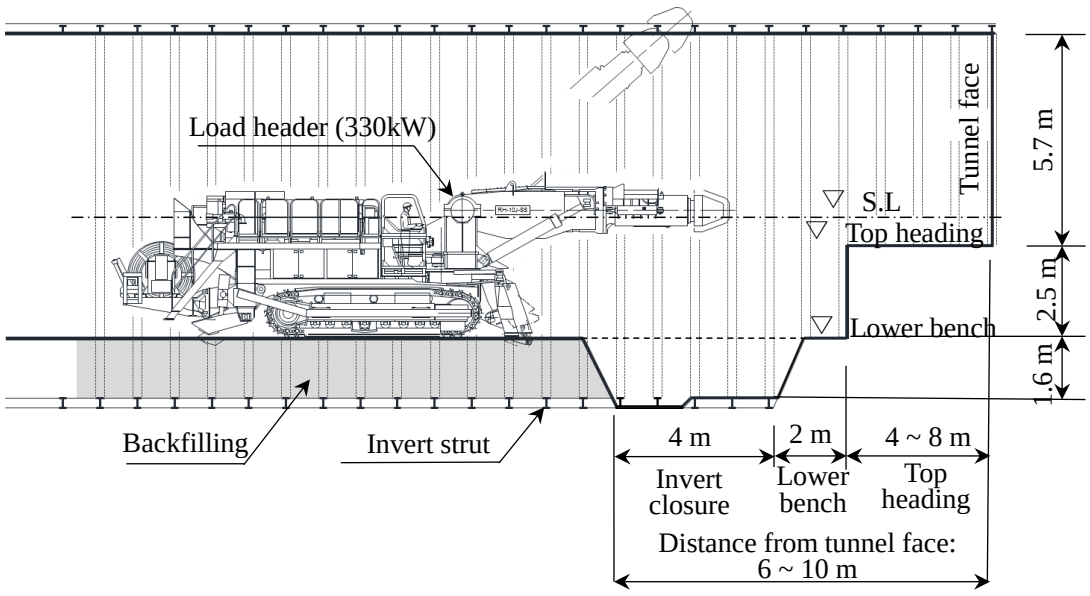

Fig. 4.3 Invert closure using the bench method.

Table 4.1 Representative support patterns applied in the WS of Tawarazaka Tunnel.

Support pattern	Standard	Special
Steel Support	H150	H200
Support location	Top and lower sections	Top and lower sections
Space of steel beams (m)	1.0	1.0
Shotcrete thickness (mm)	150	250
Rock bolt	3 m × 14	3 m × 22

4.2.4 Ground squeezing

Squeezing is a time-dependent, large deformation process that occurs around tunnels associated with the plastic flow caused by the reduction of the shear strength of rock masses (Barla, 2001; Japan Railway Construction, 2009). In practice, the ground deformation often occurs due to the combined squeezing and swelling of rock masses, which are difficult to distinguish (Okazaki et al., 2016). An X-ray diffraction analysis, a cation exchange capacity (CEC) test, a water content test (WCT) and a point loading test (PLT) were conducted to test the smectite content, CEC, natural water content and uniaxial compressive strength of the rocks, respectively. Fig. 4.5 shows the test results in two tunnel profiles located at the starting and ending sides in the chainages of 14 km 600 m and 16 km 200 m, respectively. The smectite contents in these two profiles were 2% and 10%, which were less than the critical value of 20% (Japan Society of Civil

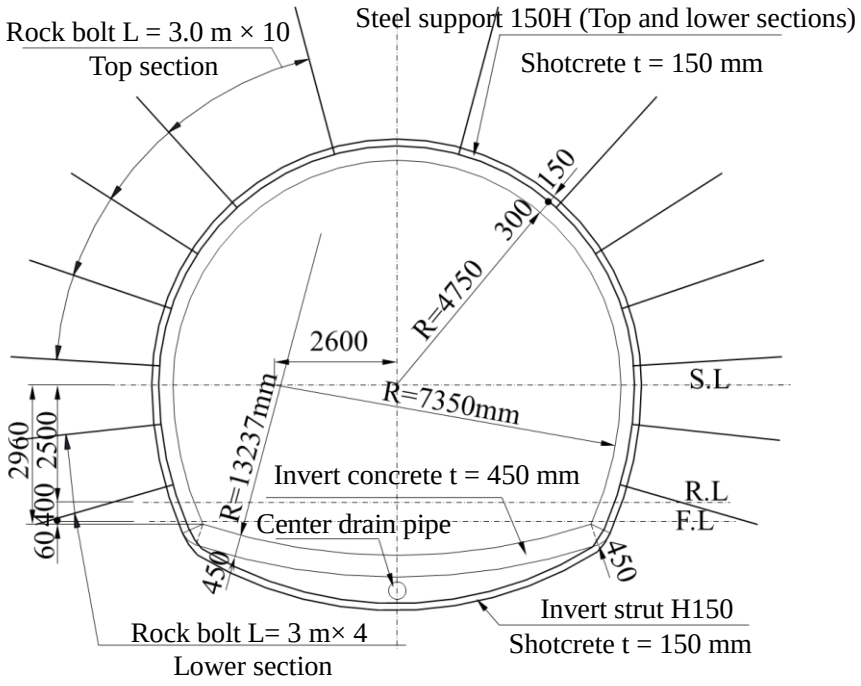

(a) Standard support pattern

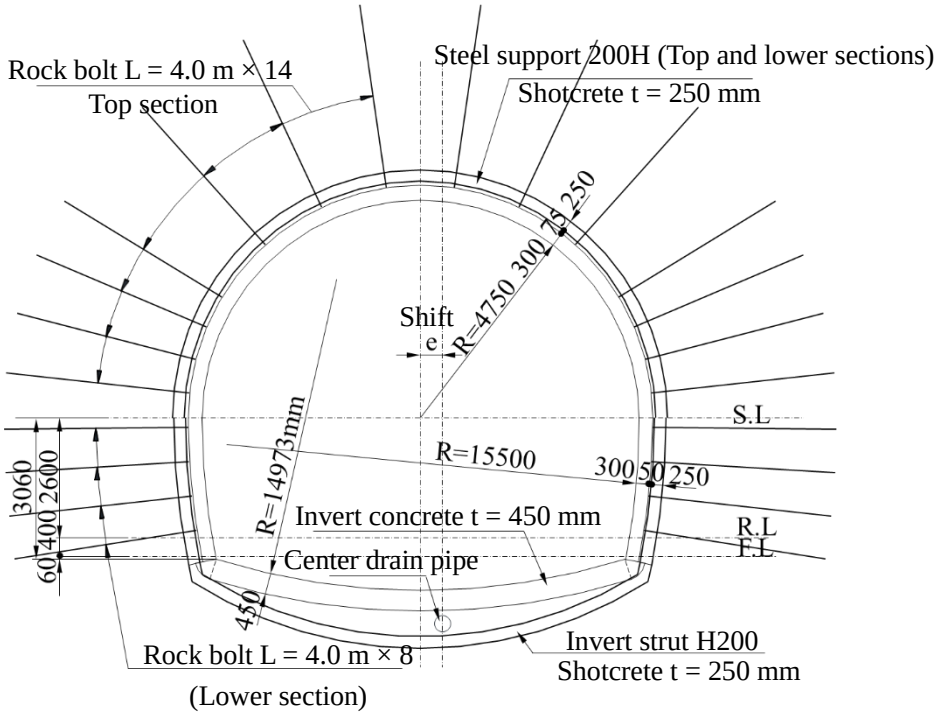

(b) Special support pattern

Fig. 4.4 Support systems in the WS of Tawarazaka Tunnel (unit: mm).

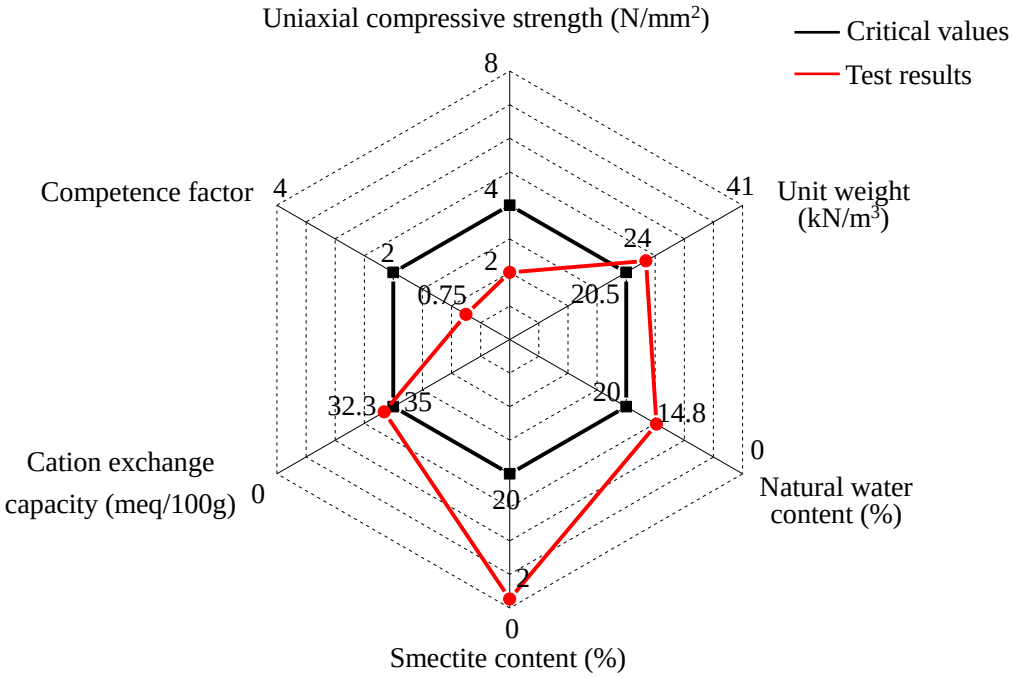

(a) Chainage 14 km 600 m

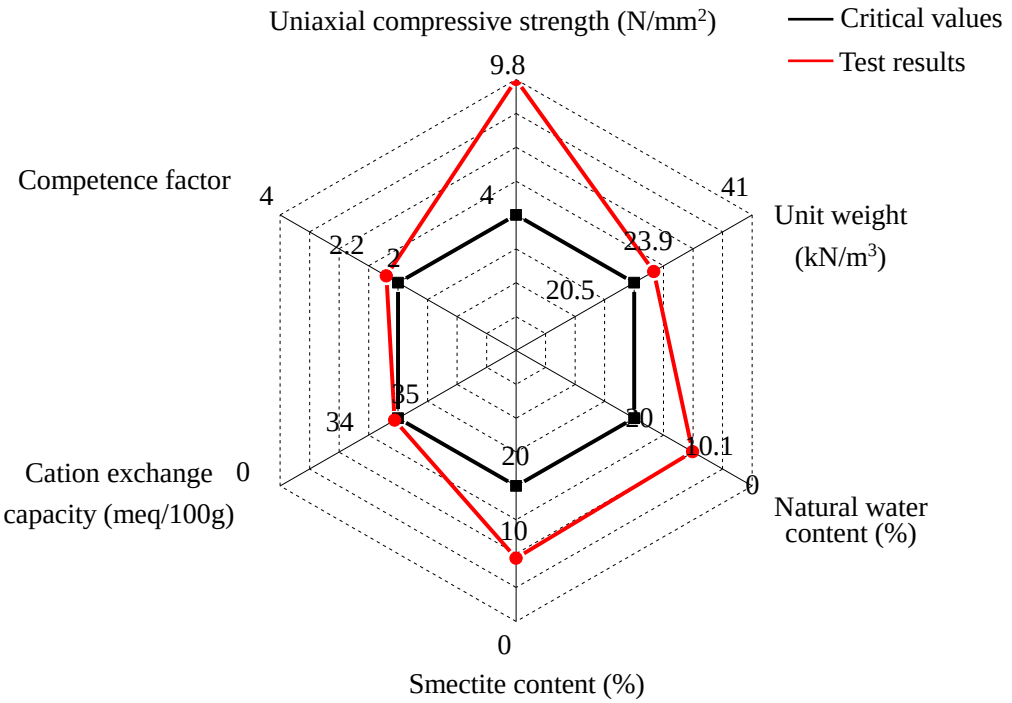

(b) Chainage 16 km 200 m

Fig. 4.5 Results of the X-ray diffraction analysis, cation exchange capacity test, water content test and point loading test in two representative tunnel profiles located at the starting and ending sides of the chainages of (a) 14 km 600 m and (b) 16 km 200 m ((a) Chainage 14 km 600 m and (b) Chainage 16 km 200 m).

Engineers, 2006). The values of cation exchange capacity (CEC) were 32.3 meq/100 g and 34 meq/100 g, both of which were smaller than the upper limit of 35 meq/100 g (Japan Society of Civil Engineers, 2006). Because the rocks exhibited good physicochemical characteristics, deformation was primarily caused by squeezing rather than swelling (Japan Society of Civil Engineers, 2006). The competence factor was defined as the ratio of the uniaxial compressive strength of the rock mass to the in situ stress and was selected as an indicator to quantify ground squeezing (Hoek and Marinos, 2000a, b). The performances of the uniaxial compressive strength qu and competence factor Gn of the rocks are plotted in Fig. 5.6. A large variation in qu was observed, which might have been induced by the existence of a bedding plane in the local region. Aydan et al. (1993) suggested that squeezing occurs if Gn is less than 2.0 based on experiences in Japan. In the WS of the Tawarazaka Tunnel, Gn in several profiles was less than 2.0, which further confirmed that deformation was commonly induced by ground squeezing.

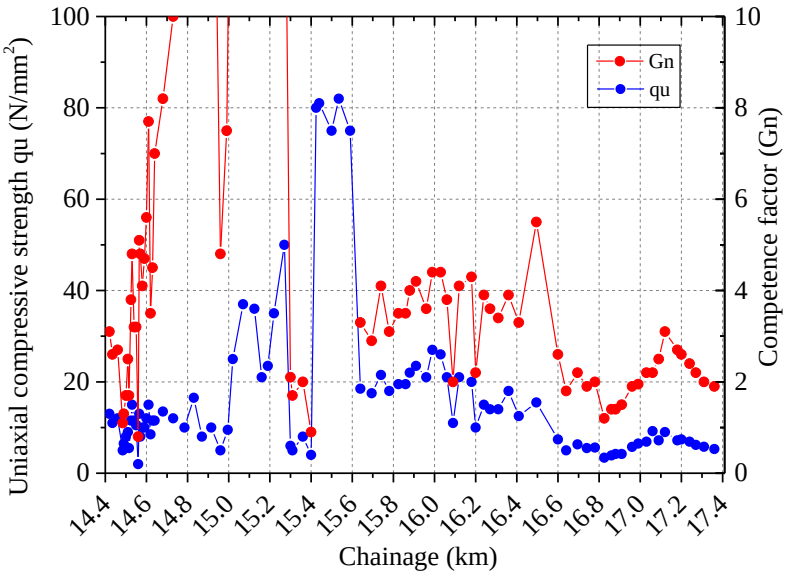

Fig. 4.6 Performances of compressive strength qu and competence factor Gn.

4.3 Squeezing characteristics analysis based on in-site measurements

4.3.1 Data collection

To analyze the squeezing characteristics, convergence was measured at the positions of T1-T3, as shown in Fig. 4.7. Since the rock formations in the ES were mainly composed of sandstone that formed in the Paleogene Period, the convergences in the ES were selected for comparison to analyze the ground squeezing caused by different rock formations. Moreover, the convergences of 8 existing Shikansen tunnels

that were excavated in mudstone and sandstone formations formed in the Neogene period were also analyzed. A total of 14 sections and 2157 tunnel profiles are summarized in Table 4.2. To ensure the comparability of the measured data, only the tunnel profiles with the same depth of overburden were selected. Fig. 4.8 shows the variations in tunnel profile numbers and cumulative percentages for various overburdens, and tunnel profiles with overburden in the range of 100 m ~ 150 m accounted for 35.79% and 31.38% of the Tawarazaka Tunnel and tunnels in the Neogene formation (NF), respectively..

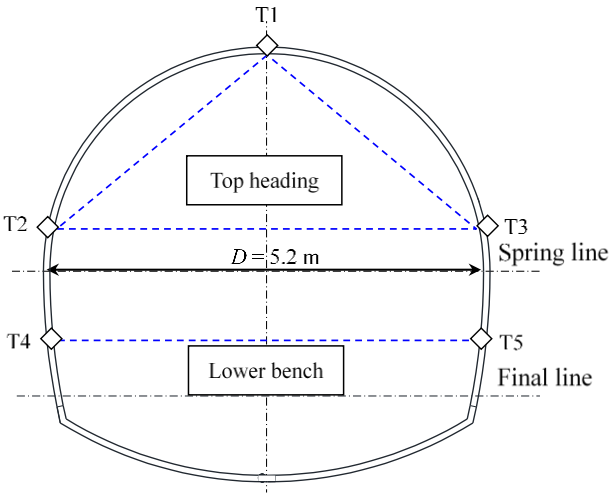

Fig. 4.7 Arrangement of measurements points in the cross section to characterize tunnel deformation (◇ Position of measuring points).

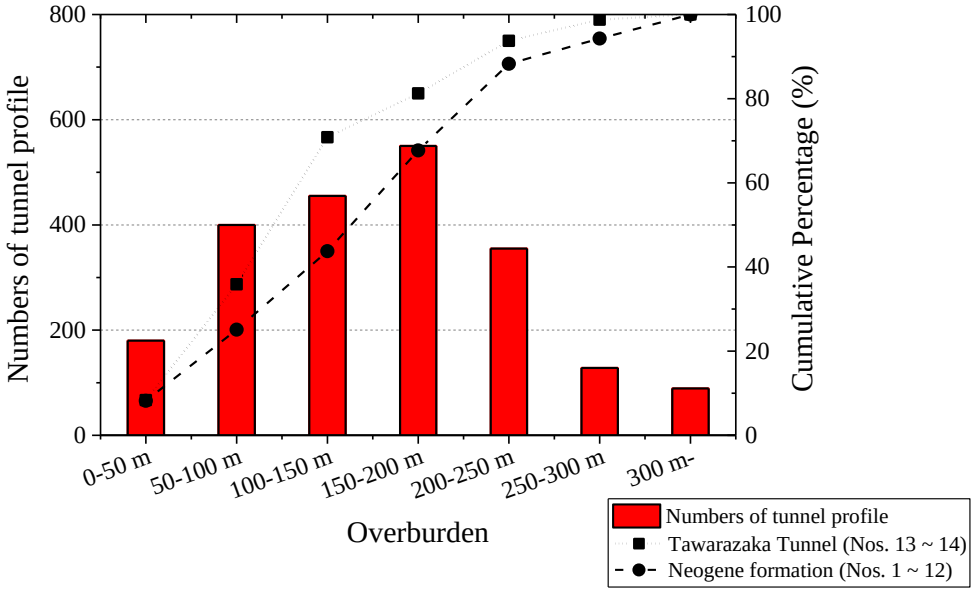

Fig. 4.8 Variation in tunnel profile number and cumulative percentage for various overburden depths.

Table 4.2 General profile of objective tunnels.

No.	Railway section	Tunnel (Engineering district)	Geological age	Lithology	The maximum of overburden (m)	Numbers of cross sections
1	Hokkaido Shinkansen	IzumisawaTunnel	Neogene formation	Sandstone, mudstone	200	101
2	Tohoku Shinkansen	Iwate-Ichinohe Tunnel (Mega section)		Tufaceous sandstone, tuffaceous breccia	170	54
3	Hokuriku Shinkansen	Ichinose Tunnel (East section)		Tuffaceous breccia, tuff	270	157
4		Ichinose Tunnel (West section)		Tuffaceous breccia, tuff, andesite	310	115
5		Usui Tunnel (East section)		Tuffaceous breccia	300	124
6		Iiyama Tunnel (Tomikura section)		Sandstone, mudstone	330	294
7		Iiyama Tunnel (Higashisuganuma Section)		Mudstone	220	206
8		Iiyama Tunnel (Konari Section)		Mudstone	250	362
9		Iiyama Tunnel (Itakura Section)		Mudstone, gravel	180	72
10		Matsunoki Tunnel (East section)		Mudstone, sandstone	200	115
11		Mineyama Tunnel (East section)		Mudstone	390	130
12		Mineyama Tunnel (West section)		Mudstone	300	8
13	Kyushu Shinkansen	Tawarazaka Tunnel (East section)	Paleogene formation	Sandstone, tuffaceous breccia, andesite	150	123
14		Tawarazaka Tunnel (West section)		Mudstone, tuffaceous breccia, basalt	260	296
	Total	8 Tunnels (14 Engineering sections)				2157

4.3.2 Convergences

Fig. 4.9 shows the relationship between the horizontal convergence δ_h and the crown settlement δ_v measured in the upper section. Here, δ_h was the total horizontal convergence at T2 and T3, as illustrated in Fig. 4.9. In the ES section of the Tawarazaka Tunnel, the overall horizontal convergences were small and concentrated in the interval of 0 ~ 50 mm, with crown settlement varying from 0 to 25 mm. The convergence ratio λ, which was determined as the ratio of δ_h to δ_v, was approximately 2 in the ES of the Tawarazaka Tunnel. Additionally, when the tunnel deformed uniformly, the radial deformation around the tunnel should be almost the same; thus, λ should equal 2. $\lambda > 2$ suggests that convergence in the horizontal direction is greater than that in the vertical direction. In the WS, λ increased from 2 to 10, revealing that the horizontal convergence in this section was greater than the vertical convergence. For tunnels in the NF (Nos. 1 ~ 12), the plot covered a wide range of distributions, and λ varied from approximately 1 to 5. It was evident that ground squeezing occurred in the WS, and δ_h in the mudstone formation of the WS was larger than that in the sandstone formation of the ES.

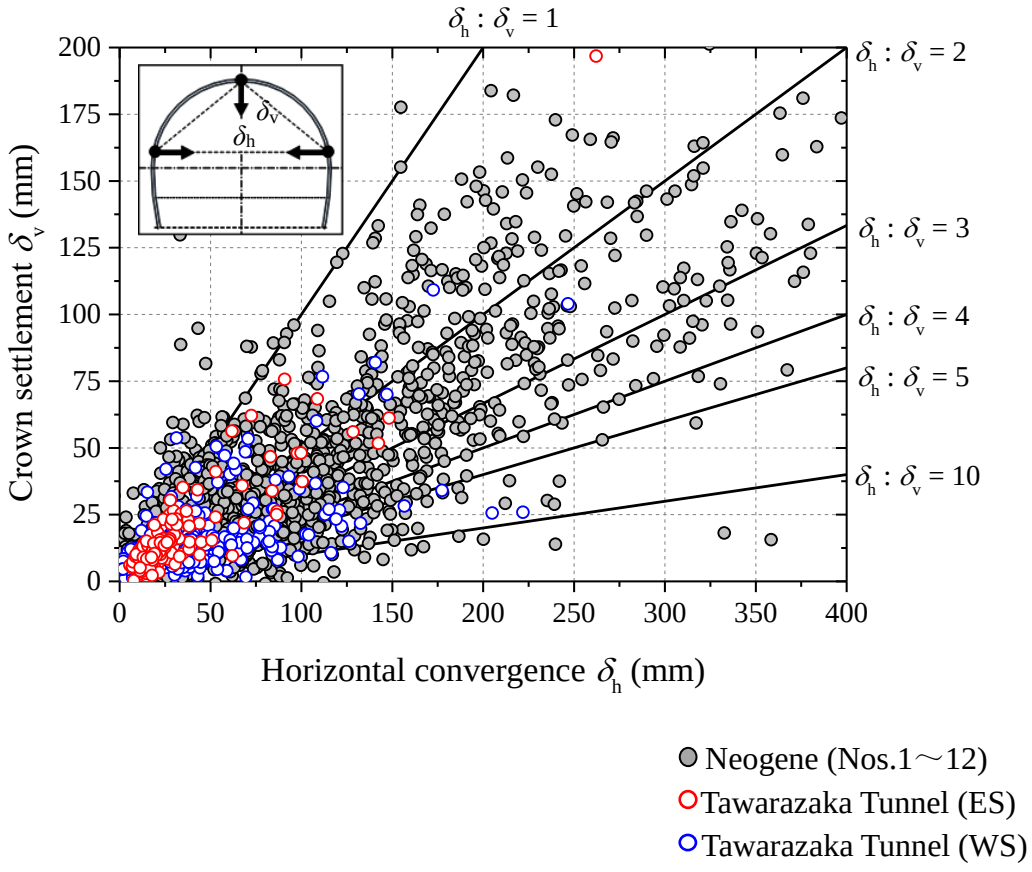

Fig. 4.9 Correlation between horizontal convergence δ_h and vertical convergence δ_v.

4.3.3 Overburden

The correlation between the measured λ and overburden H is shown in Fig. 4.10, in which the green line denotes the fitting curve of H and λ. λ increased as H increased when $H \leq 100$ m in the WS (No. 14) and tunnels in the NF (Nos. 1~ 12), revealing that a large overburden depth below a critical value led to a higher convergence ratio. λ varied from 4.0 to 4.5 when $H \geq 100$ m in the WS. However, λ was equal to 3.0 and 2.0 for tunnels in the NF (Nos. 1~ 12) and ES (No. 13), respectively. It can be concluded that λ in the WS was larger than those in the NF and ES, likely due to the high deformability of mudstone in the Paleogene formation.

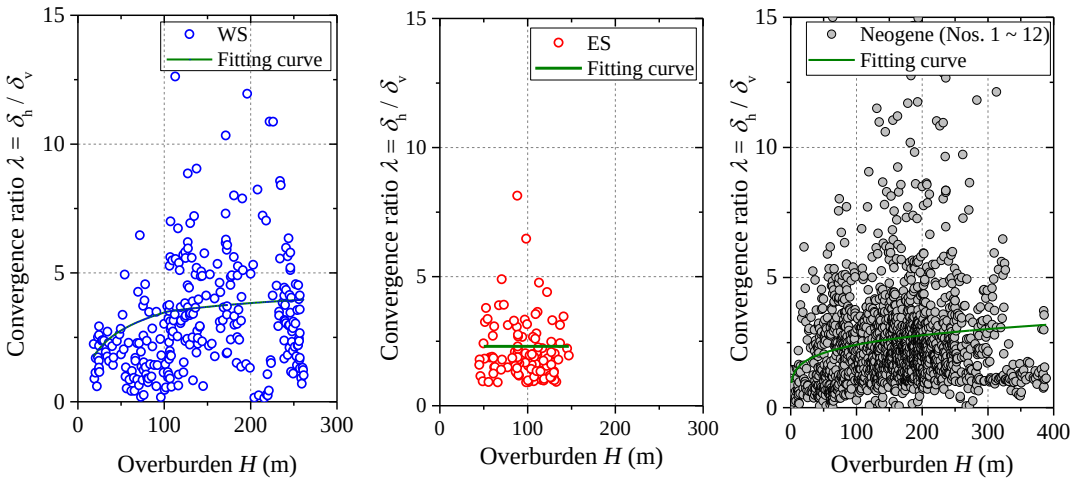

(a) Tawarazaka Tunnel (WS) (b) Tawarazaka Tunnel (ES) (c) Tunnels in NF

Fig. 4.10 Correlations between overburden H and convergence ratio λ for (a) the WS of Tawarazaka Tunnel, (b) the ES of Tawarazaka Tunnel, (c) tunnels in NF.

4.3.4 Apparent young's modulus

The apparent young's modulus E_a was selected to evaluate the deformation behaviors of rocks in engineering fields, which can take into account the tunnel shapes, effects of support, and ground stress condition (Nasseri et al., 2003; Einav et al., 2004; Kakunai et al., 1985 and Jardine et al., 1986). In the present study, E_a was studied by simplifying the shape of tunnels to circular. The rock masses were assumed to be an isotropic homogeneous elastic material, then E_a and initial horizontal stress ratio K_0 (ratio of horizontal stress to vertical stress, $K_0 = \sigma_h / \sigma_v$) of rocks around railway tunnel could be determined as follows (Working group report of economic research subcommittee of Shinkansen tunnel, 1983):

$$E_a = \frac{0.75 \times K_0 \times \gamma_t \times H}{\varepsilon_h} \tag{4.1}$$

$$K_0 = \frac{\lambda \times (2-\nu) + 2 \times (1-\nu)}{\lambda \times (1-\nu) + 2 \times (2-\nu)} \tag{4.2}$$

where, γ_t is the unit weight of rock masses that equals to 21.0 kN/m^3, ε_h is the horizontal strain (= δ_h / D) and ν is poisson's ratio.

The relationship between H_0 and E_a is shown in Fig. 4.11, which shows that the performance of E_a depended on the variation of H_0. The order of E_a was 10^2 ~ 10^3 MPa, which was consistent with the empirical value of soft or medium hard rocks (Japan Society of Civil Engineers, 2006).

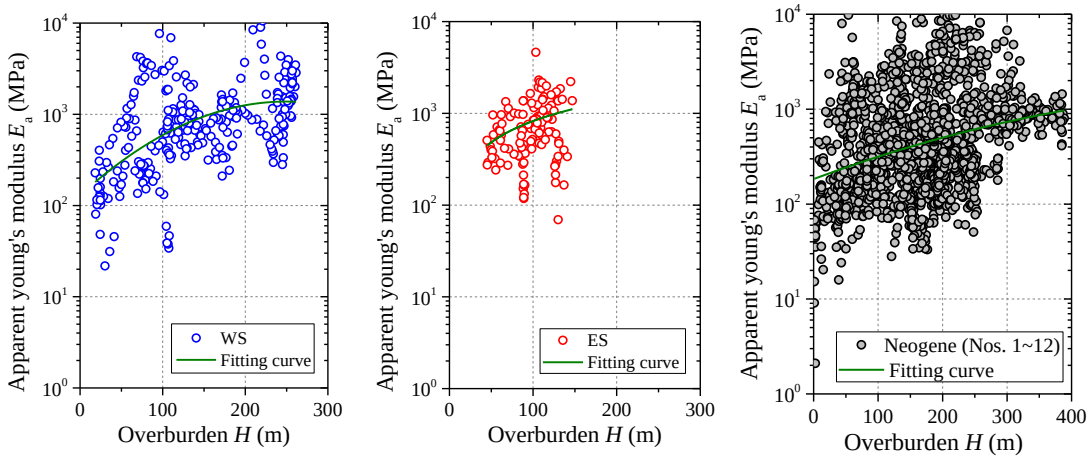

(a) Tawarazaka Tunnel (WS) (b) Tawarazaka Tunnel (ES) (c) Tunnels in NF

Fig. 4.11 Correlations between E_a and H for (a) the WS of Tawarazaka Tunnel, (b) the ES of Tawarazaka Tunnel, (c) tunnels in NF.

4.3.5 Initial horizontal stress ratio

The initial horizontal stress ratio K_0 has a considerable impact on the deformation characteristics of a tunnel after excavation (Pulko et al., 2011; Li et al., 2010). The correlation between H and K_0 is depicted in Fig. 4.12. The first quarter point K_f and third quarter point K_t, as formulated in Eqs. (4.3) and (4.4), were selected to give describe K_0:

$$K_f = K_{min} + (K_{max} - K_{min}) / 4 \tag{4.3}$$

$$K_t = K_{min} + 3 \times (K_{max} - K_{min}) / 4 \tag{4.4}$$

where K_{min} and K_{max} are the minimum and maximum values of the horizontal stress ratio, respectively, for each overburden depth.

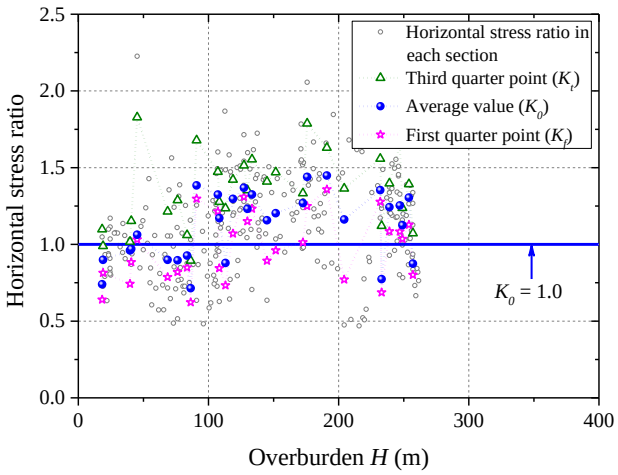

(a) Tawarazaka Tunnel (WS)

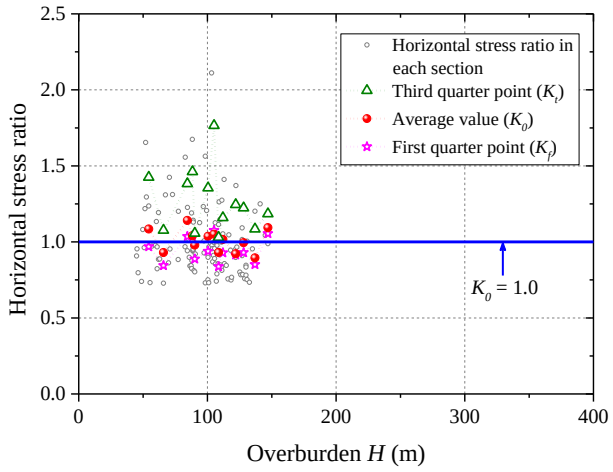

(b) Tawarazaka Tunnel (ES)

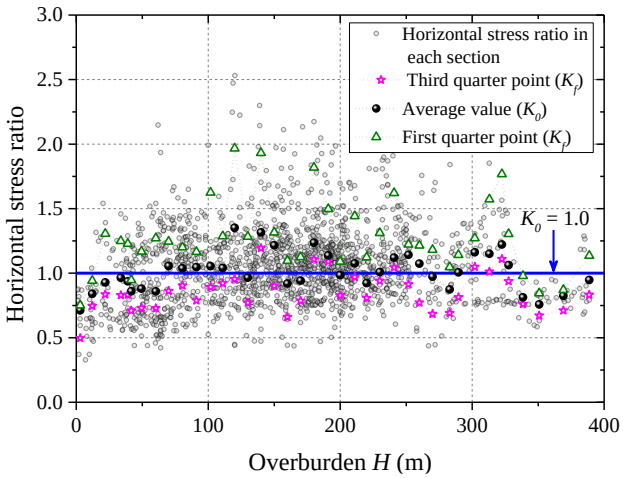

(c) Tunnels in NF

Fig. 4.12 Correlations between overburden H and horizontal stress ratio K_0 for (a) the WS of Tawarazaka Tunnel, (b) the ES of Tawarazaka Tunnel and (c) tunnels in NF.

K_0 changed significantly in the WS with variations in H. When $H \leq 100$ m, the average value of K_0 was approximately 1.0, and when $H \geq 100$ m, K_0 varied from 1.1 to 1.4 (see Fig. 4.12(a)). However, for tunnels in the NF (see Fig. 4.12(c)) and ES (see Fig. 4.12(b)), the average values of K_0 were approximately 1.0. Due to the differences in K_0 and the deformation characteristics between the tunnels in the WS, ES and NF, K_0 was one of the main factors that led to ground squeezing (Bilgin et al., 2012).

4.3.6 Effects of geological characteristics of host rocks

Two representative tunnel faces in the WS and ES of the Tawarazaka Tunnel are shown in Fig. 4.13. The rock masses in the WS were mainly composed of mudstone, and slickensides generally formed in the separation planes of stratified rocks (see Fig. 4.13(a)), which may lead to sudden shear failure and enlarge the plastic zone in rock masses, resulting in ground squeezing in this section (Bilgin et al.; 2012 and Suzuki et al.; 1993). However, because the rock masses in the ES were mainly composed of sandstone (see Fig. 4.13(b)), the frictional resistance caused by the stress relief was not significantly reduced during the excavation process, and only small horizontal convergence was observed due to the high stability of the rock masses, as shown in Fig. 4.9 (Kitagawa, 2003).

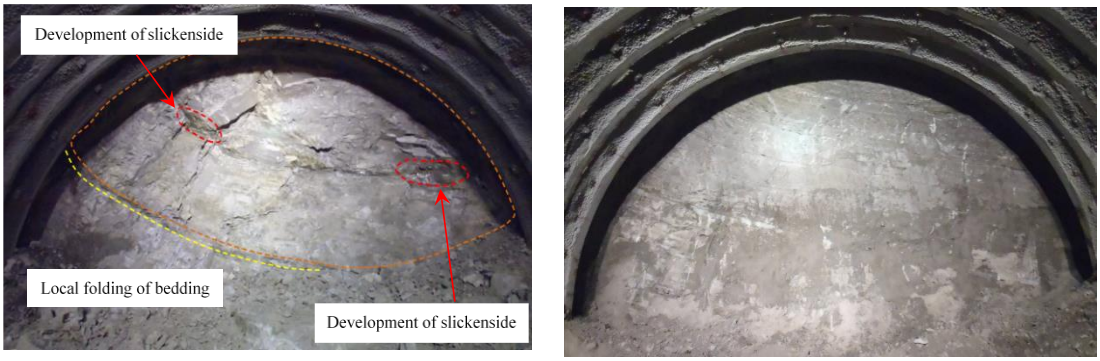

(a) a tunnel face in WS (b) a tunnel face in ES

Fig. 4.13 Representative tunnel faces in (a) WS and (b) ES.

4.4. Analysis of squeezing characteristics based on numerical modeling

Although ground squeezing characteristics have been analyzed based on the in situ measurements discussed in Section 4.3, the main factors that induced the ground squeezing were not clarified. Numerical modeling has become an important approach in the design of underground structures in rocks (Vardakos et al., 2007). It can take into account the key issues during tunneling, such as the geological characteristics of the

ground, in situ stress conditions, etc., to reproduce a realistic representation of field conditions. Since three-dimensional modeling is time consuming and not always practical, an equivalent two-dimensional model was selected by assuming plane strain conditions and using the convergence-confinement method during the numerical analysis (Vardakos et al., 2007; Fakhimi et al., 2004; Karakus, 2007 and Hejazi et al., 2008). The convergence-confinement method introduced by Panet and Guenot (1982) can account for the three-dimensional face effect determined by the plane strain analysis. According to this approach, the radial stress σ_r acting on the tunnel periphery is utilized to reproduce the face effect during excavation and can be given as follows:

$$\sigma_r = (1-\lambda_s)\sigma_0 \tag{4.5}$$

$$\lambda_s = \frac{u_r(x)}{u_r(\infty)} \tag{4.6}$$

$$u_r(\infty) = \frac{(1+\nu)}{2E}\sigma_0 D \tag{4.7}$$

where σ_0 is the initial stress of the ground (MPa), λ_s is the reduction factor utilized in the two-dimensional simulation and varies from 0 to 1, $u_r(x)$ is the radial component of displacement at a distance x behind the face (m) and $u_r(\infty)$ is the radial component of displacement at an infinite distance behind the tunnel face (m).

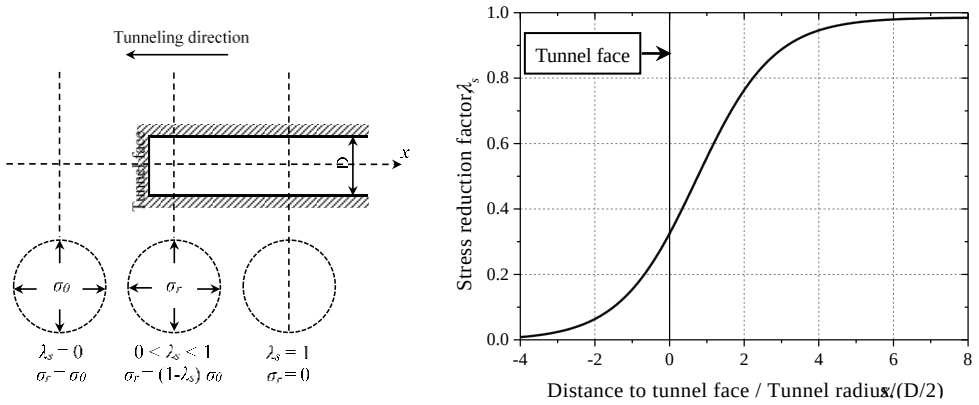

(a) Confinement loss in a tunnel (b) Determination of stress reduction factor

Fig. 4.14 Determination of stress reduction factor in the vicinity of tunnel face (after Panet and Guenot, 1982).

In the plane strain analysis, σ_r was applied on the tunnel periphery and was decreased from σ_0 to zero with no support, as illustrated in Fig. 4.14(a). The relationship between λ_s and the ratio of distance from the tunnel face to the radius of the tunnel is plotted in Fig. 4.14(b), and the reduction factor for the initial stress at the working face can be determined based on this plot. In the present study, the reduction factor was

determined as 0.3 based on Fig. 4.14(b) (Kitagawa et al.; 2002 and Fakhimi et al.; 2004).

A field measurement analysis and literature survey showed that K_0, the strength of a rock mass, the existence of bedding joints or intermix bands and H are the main factors that potentially lead to ground squeezing (Steiner 1996; Bilgin et al., 2012; Kovári et al., 1996). In the present study, a series of numerical analyses was performed to determine the deformation characteristics by comparing the numerical results to the measured convergences.

4.4.1 Introduction of the tunnel profile used in numerical analysis

The tunnel profile in the chainage of 16 km 074 m, as shown in Fig. 4.15, was selected to build the two-dimensional numerical models. Mudstone and mixed bands with mudstone and tuff were encountered, with the strike of the bedding plane parallel to the tunnel axis. From the upper left to the lower right side, the orientation of the bedding plane is approximately 15°. The convergence behaviors of rocks exposed in the tunnel profile are shown in Fig. 4.7. The targets of T1-T3 were fixed after the installation of primary supports in the upper section of the tunnel; thus, the initial values of these three targets were set to 0 when the supports in the upper section were installed. The convergences in this tunnel profile are given in Table 4.3, with λ = 6.15, revealing that squeezing was encountered in this profile.

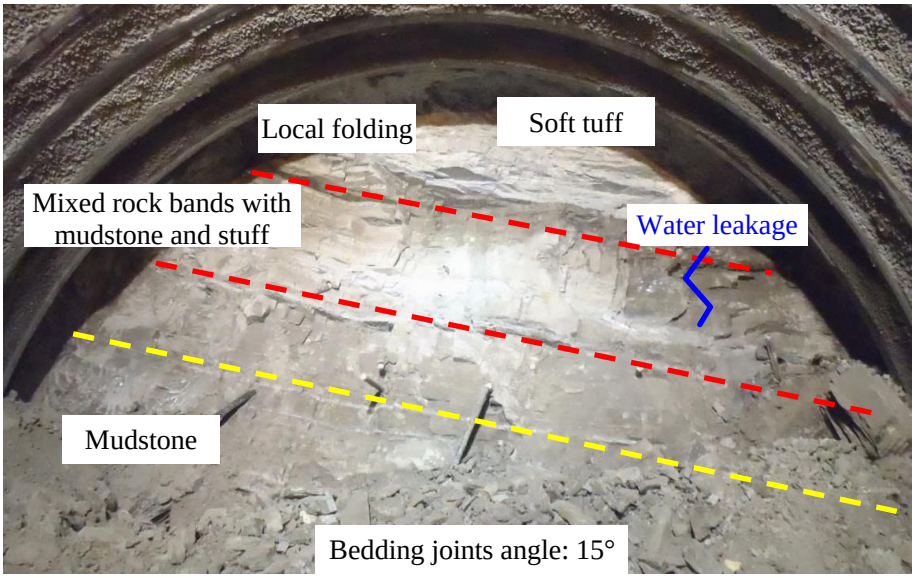

Fig. 4.15 The exposure of rocks on tunnel face in the chainage of 16 km 074 m (H = 234.9 m).

Table 4.3 Measured convergences at different observation positions.

Observation positions	T1	T2	T3
δ_h (mm)	--	90	-70
δ_v (mm)	-26	-52	-36
λ		6.15	

Notes: Direction of horizontal displacement: → (+), ← (-);
Direction of vertical displacement: ↑ (+), ↓ (-).

4.4.2 Numerical modeling

The numerical model was generated using the finite difference method (FDM). Fig. 4.16 shows the boundary conditions utilized in the numerical analysis. To reduce the influence of boundary effects on the accuracy of the numerical simulation results, the distance from the side of the tunnel to the boundary of the numerical model was selected as 3*D* (Feng et al., 2013). A uniform vertical stress σ_v was applied on the top of the model corresponding to the overburden stress, and a horizontal stress σ_h that varied linearly with depth was applied on the lateral boundaries, as depicted in Fig. 4.16. The bottom boundary was fixed with no rotation or displacement.

The Mohr-Coulomb model was adopted to investigate the elastic/plastic deformation behaviors of rocks, and an interface element based on the Mohr-Coulomb failure criterion was selected to reproduce the existence of bedding joints. The effects of steel support and shotcrete lining were reproduced by entity elements based on a composite equivalent section. The thickness of the shotcrete lining was 150 mm, and the excavation and installation of supports were consistent with the field construction.

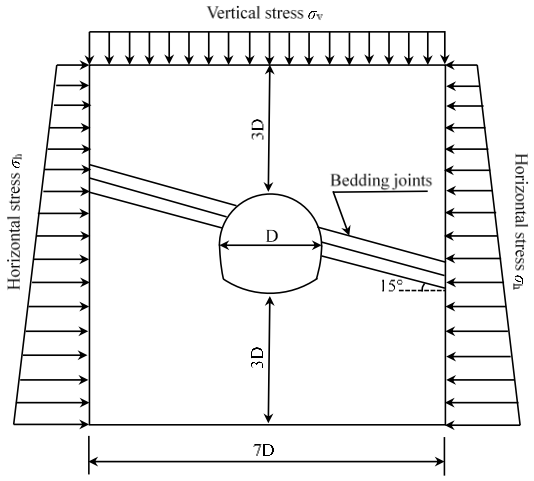

Fig. 4.16 Boundary conditions of numerical analysis.

4.4.3 Results and analysis

4.4.3.1 Effects of the bedding joint stiffness and horizontal stress ratio

The properties of the rock masses were preliminarily determined based on geological surveys, as depicted in Figs. 4.6 and 4.15. Since the intermixed bands were composed of mudstone and tuff, the properties of the rock masses that overlaid the mudstone layer were determined as rock type CII, and the rock masses in the mudstone layer, as shown in Fig. 4.15, were determined as rock type DI (The ministry of Public Works Research Institute Tunnel Laboratory, 1994; Urban Development Bureau of Hiroshima, 2013). The mechanical properties of these two types of rocks are initially summarized in Table 4.4. To obtain the mechanical properties of bedding joints, a digitally controlled shear test was conducted by utilizing the test approach described by Jiang et al. (2004, 2006), and the test results are shown in Table 4.5. Due to the existence of microcracks, cleavages and faults at the engineering sites, the physical and mechanical parameters obtained from the laboratory experiments should be discounted before they are adopted in numerical analyses (Barton, 2013; Li et al., 2016 and Fakhimi et al., 2004). Wang et al. (2012) estimated the effects of bedding joints on the stability of a mine tunnel through three-dimensional discontinuum and continuum analyses, and 30% increases or decreases in bedding joints parameters were applied to account for the hardness of the surrounding rocks, such as diorite, marble, granite and magnetite. In the present study, to investigate the effects of the joint stiffness, a series of numerical analyses based on the FDM were carried out by discounting the parameters of shear stiffness k_s and normal stiffness k_n. Here, the discount ratio d_r of k_s and k_n varied from 0 to 0.9 and was applied. K_0 was determined as 0.8 ~ 1.4 based on the results, as shown in Fig. 4.12(a).

The results of the numerical analysis are presented in Fig. 4.17 in terms of K_0 versus the tunnel convergences at T1, T2 and T3. The tunnel deformed as the joint stiffness decreased, revealing that a low bedding joint stiffness led to a large deformation of rocks in the tunnel (Wang et al., 2012). With the discount of the bedding joint stiffness, the horizontal convergences at the left and right walls of the tunnel were almost symmetrical, as shown in Fig. 4.17 (a); however, these parameters were unsymmetrical based on the in situ investigations, as shown in Table 4.3. These results indicate that the bedding joints were not the main factor that led to the unsymmetrical deformation of the tunnel. When K_0 was greater than 1.3, δ_h at the right wall of the tunnel was larger than the on-site measurement, whereas at the left wall, the simulated value was much smaller than the measured value. Fig. 4.17(b) shows the correlation between K_0 and δ_v at T2 and T3. When d_r = 0 or 0.5, δ_v at the right wall of the tunnel was generally less than that at the left wall. δ_v on the right side of the tunnel increased considerably as d_r increased. When d_r > 0.5 and the horizontal stress ratio was larger

than 1, δ_v on the right side of the tunnel was greater than that on the left side. It can be deduced that a reduction in the joint stiffness considerably increased the vertical convergence on the right side of the tunnel. With the increase in K_0, δ_h at both side walls of the tunnel increased linearly; however, δ_v tended to flatten, which could lead to an increase in λ.

The influences of bedding joint stiffness and K_0 on λ are shown in Fig. 4.18. A low value of bedding joint stiffness and a large K_0 led to a large value of λ. When $K_0 \geq 1.3$, λ was not merely influenced by the behavior of the bedding joint stiffness. Although, λ varied from 3.5 to 4.5 when $K_0 \geq 1.2$, which agrees well with on-site measurements, as shown in Fig. 4.9, the convergence tendencies in the numerical simulations and the on-site investigations exhibited poor agreement. It can be concluded that K_0 plays a much more important role in ground squeezing than do bedding joints.

Table 4.4 Mechanical properties of rocks.

Parameters	Symbols	Unit	Ground classes	
			CII	DI
Unit weight	γ	kN/m^3	22.6	21.6
Young's modulus	E	MPa	980	490
Possion's ratio	v	--	0.30	0.35
Cohesion	c	MPa	0.98	0.49
Internal friction angle	φ	°	40.0	35.0
Tensile strength	σ_t	MPa	0.42	0.19

Table 4.5 Mechanical properties of bedding joints.

Parameters	Index	Unit	Values
Shear stiffness	k_s	MPa/m	2.42×10^3
Normal stiffness	k_n	MPa/m	10.51×10^3
Cohesion	c	MPa	0.55
Internal friction angle	φ	°	25.14
Tensile strength	σ_t	MPa	0.1

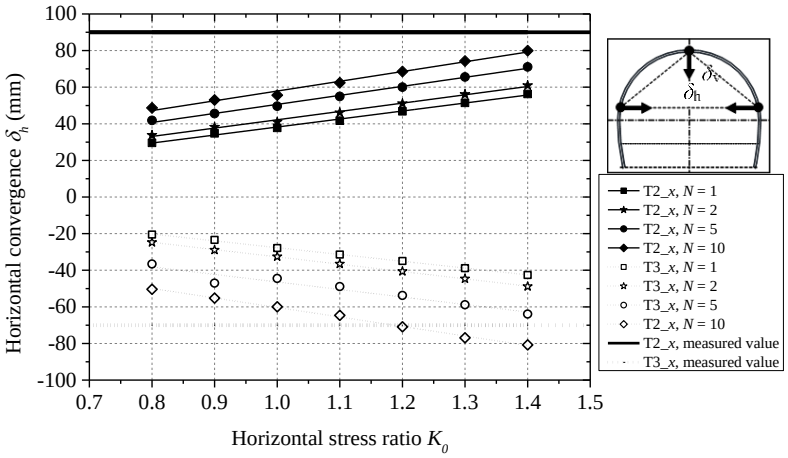

(a) Horizontal convergence at the positions of T2 and T3

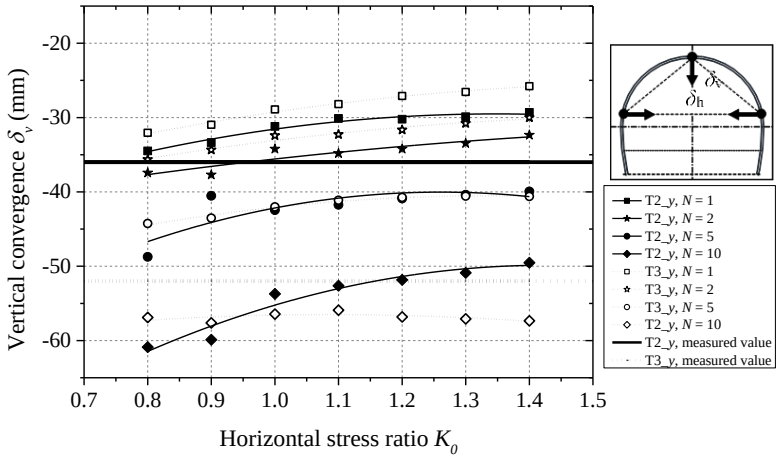

(b) Vertical convergence at the positions of T2 and T3

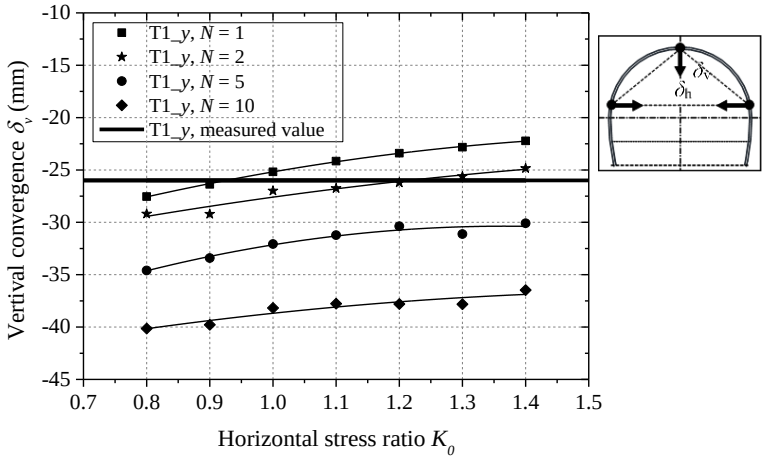

(c) Vertical convergence at the position of T1

Fig. 4.17 Effects of horizontal stress ratio K_0 and joint stiffness on tunnel convergences at different locations.

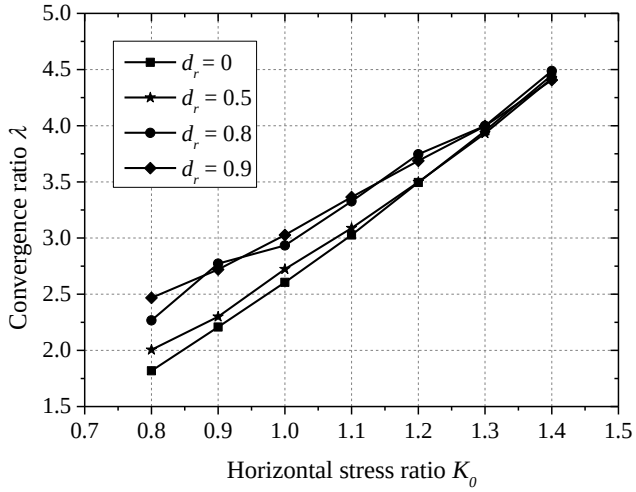

Fig. 4.18 Effects of horizontal stress ratio K_0 and joint stiffness on tunnel convergence ratio.

4.4.3.2 Effects of the internal friction angle of bedding joints

In Section 4.4.3.1, the values of bedding joint stiffness and K_0 were changed while the values of other geomechanical parameters were held constant, and the effects of these variations on tunnel convergence were analyzed. In this section, the effects of the internal friction angle of bedding joints (α_0) on tunnel convergence were investigated, and a 30% increase or decrease in α_0 was applied (Wang et al., 2012). Fig. 4.19 illustrates the tunnel convergence based on variations in α_0. No evident variation in convergence was observed as α_0 increased or decreased, especially for the horizontal convergences at T2 and T3. However, the convergences varied greatly as K_0 increased. Thus, ground squeezing was not greatly influenced by α_0.

4.4.3.3 Effects of the rock modulus

The predicted convergences based on the mechanical properties given in Tables 4.4 and 4.5 were much lower than on-site measurements. Vardakos et al. (2007) investigated the deformation mechanism of the Shimizu Tunnel in a sandstone formation using a distinct element method, and a series of numerical analyses was performed by discounting the rock mass modulus by a ratio varying from approximately 20% to 80%. Wang et al. (2012) investigated the stability of a mine tunnel through three-dimensional discontinuum and continuum analyses by increasing and decreasing the intact rock mass modulus by 20%. Kulatilake et al. (1993) obtained a mean rock mass modulus equal to approximately 30% of the Young's modulus of the intact rock for granitic gneiss. For an Aspo-diorite rock located at a depth of 485 m at the Aspo Hard Rock Laboratory, Sweden, the mean rock mass modulus was 51% of the Young's modulus of the intact rock (Kulatilake et al., 1994). For a limestone rock mass, a mean deformation modulus equal to approximately 50% of the intact rock mass modulus was

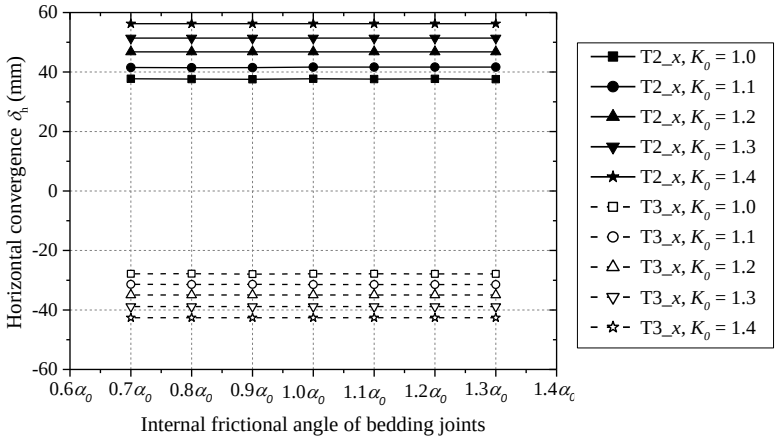

(a) Horizontal convergences at the positions of T2 and T3

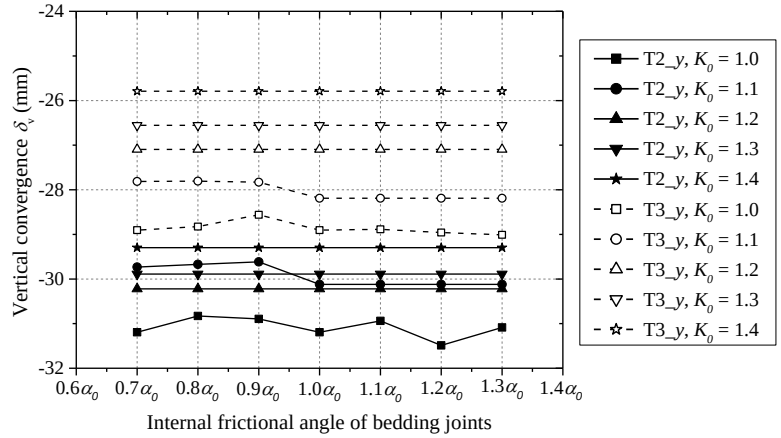

(b) Vertical convergences at the positions of T2 and T3

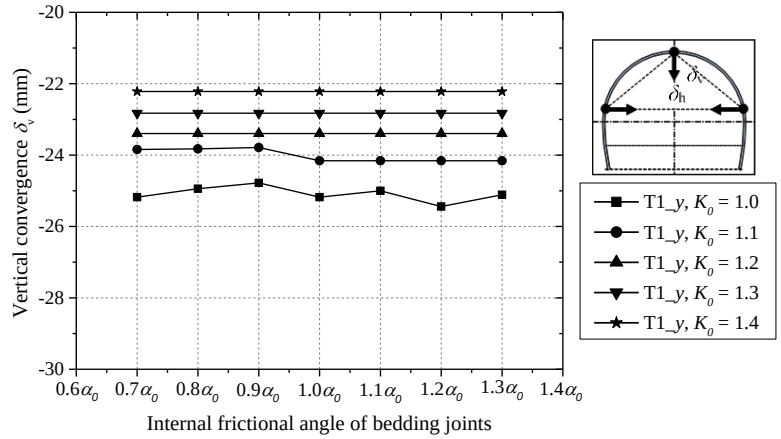

(c) Vertical convergences at the position of T1

Fig. 4.19 Effects of internal friction angle of bedding joints on tunnel convergences at different locations.

selected (Wu and Kulatilake, 2012). Since the joint stiffness and internal friction angle did not significantly affect the tunnel response, the rock mass modulus should be reduced. In the present study, a numerical analysis was performed by means of discounting the Young's modulus values of mudstone and intermixed rocks from their original values to 50% of those values. The mechanical properties of bedding joints were determined based on the test results, as given in Table 5, and K_0 was selected as 1.4 according to Fig. 4.12(a). The effects of different values of the rock mass modulus on the convergences at the positions of T1, T2 and T3 are plotted in Fig. 4.20. Here, E_m and E_t are the original Young's modulus values of mudstone and intermixed layers (Fig. 14), respectively, and the heavy black line denotes the on-site measurements. The predicted results near the heavy black line illustrate that the modulus values of rocks in these cases reasonably reproduced the in situ ground conditions. Convergence increased linearly as the Young's modulus of the rock mass decreased. To characterize the predicted and measured convergence values at these three positions simultaneously, the least square method was used to select the appropriate values of the rock mass modulus in different layers. The residual sum of squares Q can be calculated as follows (Elawadi et al., 2001):

$$Q = \sum_{i=1}^{2}(C_{P\_Ti\_x} - C_{m\_Ti\_x})^2 + \sum_{j=1}^{3}(C_{p\_Tj\_y} - C_{m\_Tj\_y})^2 \ (i = 1, 2; \ j = 1, 2, 3) \quad (4.8)$$

where $C_{p\_Ti\_x}$ is the predicted horizontal convergence at position Ti (mm), $C_{m\_Ti\_x}$ is the in situ measurement of horizontal convergence at position Ti (mm), $C_{p\_Tj\_y}$ is the predicted vertical convergence at position Tj (mm) and $C_{m\_Tj\_y}$ is the in situ measurement of vertical convergence at position Tj (mm).

A minimum value of Q was obtained when the rock mass modulus values of mudstone and intermixed layers were discounted by 59% of their original values, as plotted in Fig. 4.21. Fig. 4.22 shows the comparison between the predicted and measured convergences, and the red line and black line denote the measured and predicted convergences, respectively. The deviations between the measured convergences and the numerically predicted convergences are given in Table 4.6. There is relatively good agreement between the predicted and measured convergences. An exception occurred at position T1, which had the largest discrepancy in measured displacement because at this point, the rock mass was mainly composed of tuff and little mudstone, as shown in Fig. 4.15, which led to a larger modulus and lower deformation at the tunnel crown. The results of this analysis indicated that rock squeezing was mainly affected by the modulus of rocks.

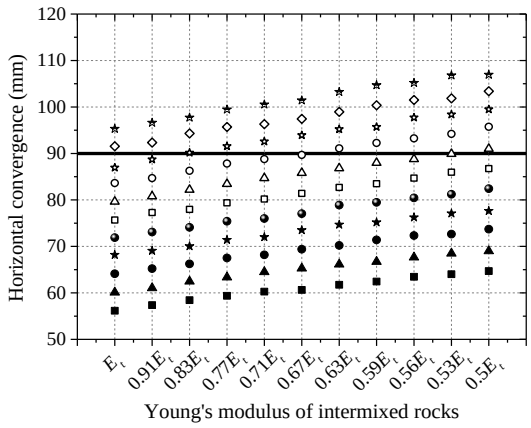

(a) Horizontal convergence at the position of T2

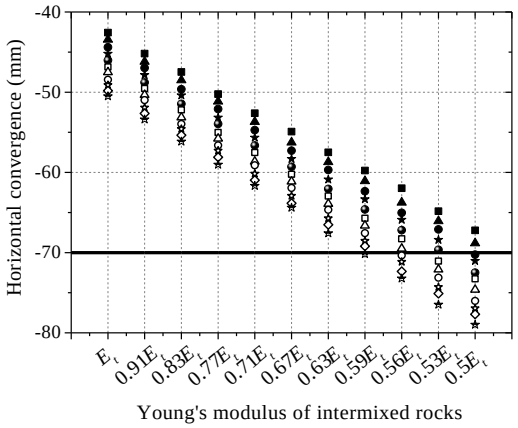

(b) Horizontal convergence at the position of T3

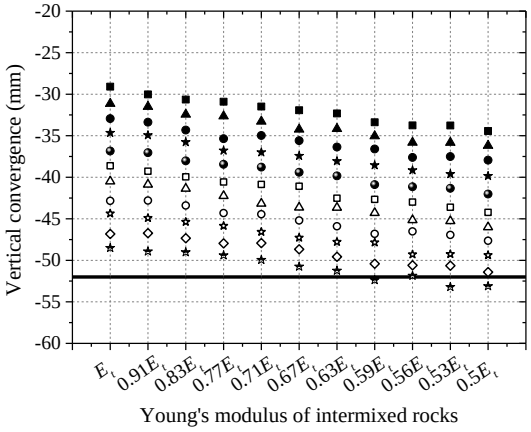

(c) Vertical convergence at the position of T2

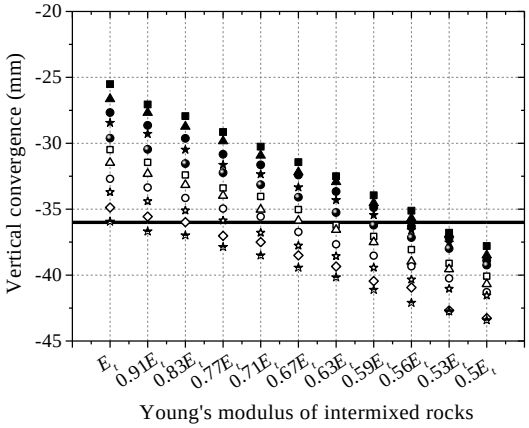

(d) Vertical convergence at the position of T3

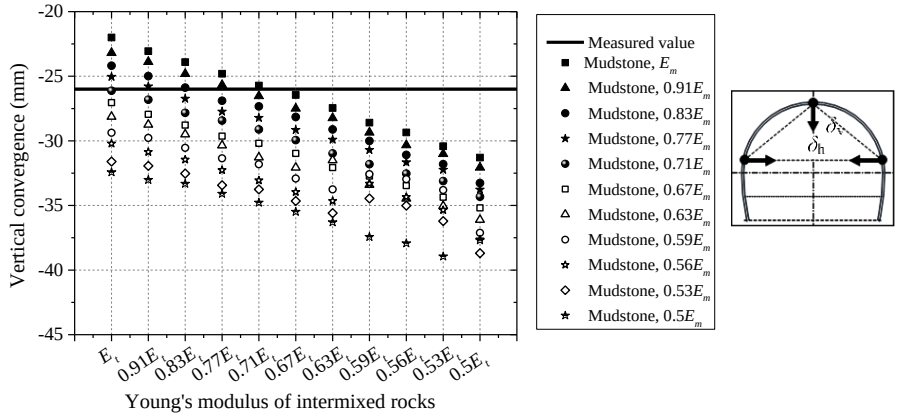

(e) Vertical convergence at the position of T1

Fig. 4.20 Effects of different values of rock mass modulus on convergences at different locations (E_m and E_t are the original values of the young's modulus of mudstone and intermixed layers, respectively).

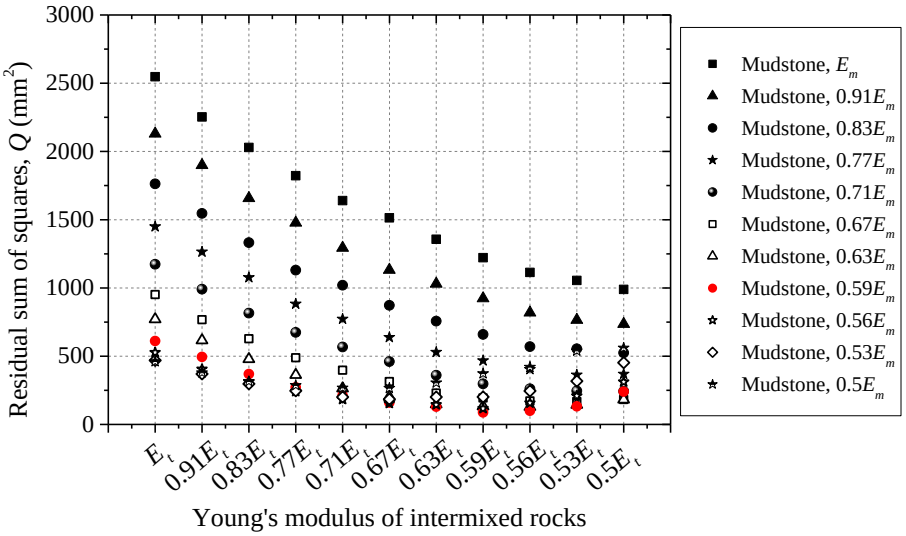

Fig. 4.21 The residual sum of squares for different rock mass modulus (E_m and E_t are the initial values of the young's modulus of mudstone and mixed rocks, respectively).

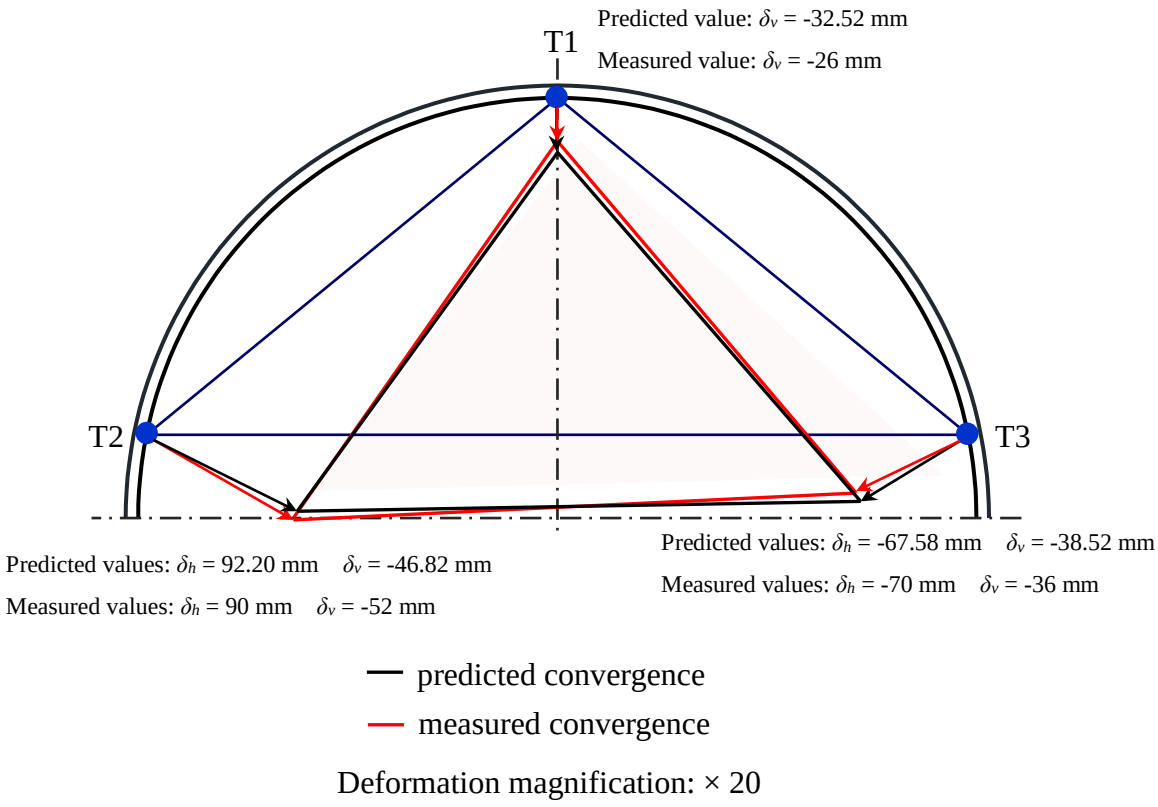

Fig. 4.22 Comparisons between predicted convergences and measured convergences.

4.4.3.4 Effects of overburden

The impacts of overburden on ground squeezing were discussed based on the analyses presented in Sections 4.4.3.1 – 4.4.3.3. In the numerical analysis, H varied

from 50 m to 300 m according to the on-site investigation, as shown in Fig. 4.8. The effects of overburden depth on the tunnel convergences at different locations are illustrated in Fig. 4.23.

As H increased, the convergence at each position increased. However, the horizontal convergences at both sides of the tunnel walls generally exhibited larger rates of increase compared to the vertical convergences. The predicted values and measured values of λ are shown in Fig. 23(b), which shows that λ increased significantly as H increased when $H \leq 100$ m. After an overburden of 100 m was exceeded, the variation

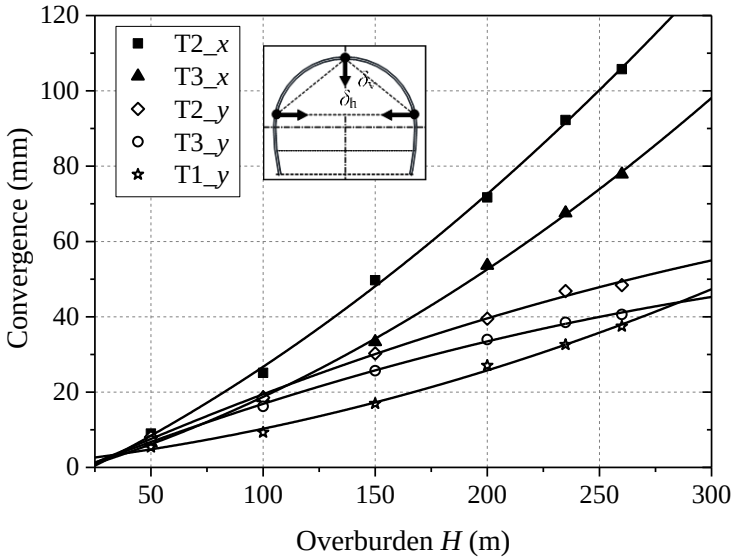

(a) Relationship between convergence and overburden at different positions

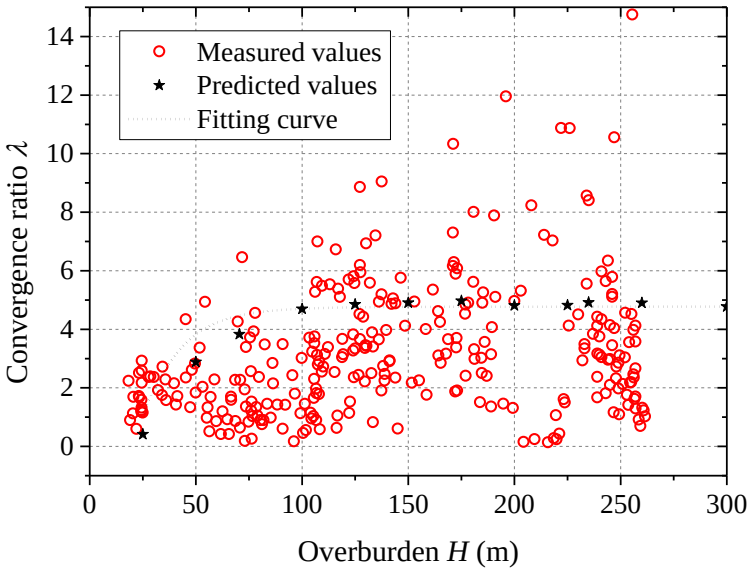

(b) Relationship between convergence ratio and overburden

Fig. 4.23 Effects of overburden on tunnel convergence at different locations.

in λ was not as remarkable. A large overburden depth could lead to large ground stress and eventually result in significant convergence in the ground. It can be concluded that overburden had a direct effect on ground squeezing, and the squeezing behavior occurred in the WS of the Tawarazaka Tunnel when an overburden of 100 m was exceeded (Bilgin et al., 2012 and Steiner, 1996).

4.5 Conclusions

The case study and detailed numerical analysis of the WS of the Tawarazaka Tunnel presented in this paper clearly show how geological conditions such as the initial horizontal stress ratio, bedding joint stiffness, bedding joint internal friction angle, rock modulus and overburden depth impact ground squeezing. On-site investigation results of 296 tunnel profiles in the WS of the Tawarazaka Tunnel were compared to those in the ES and NF, which totaled 1861 tunnel profiles. Moreover, two-dimensional numerical analysis using the originally developed FEM code was performed to investigate the main factors that influence ground squeezing in the WS of the Tawarazaka Tunnel, and the following conclusions were drawn.

Ground squeezing is prone to occur in geologic units with Paleogene mudstones. λ varied from 2 to 10 in the WS due to the deformability of mudstone and from 1 to 5 for tunnels in the NF and ES. A detailed study of the convergence data revealed that ground squeezing was related to the initial horizontal stress ratio K_0, and a larger K_0 led to a greater value of λ. Ground squeezing could be affected by poor ground conditions, such as mudstone with strongly developed slickensides.

The numerical results showed that a larger value of K_0 led to a greater convergence ratio λ, which was consistent with the measured results obtained from the Paleogene and Neogene formations. Ground squeezing was mainly affected by the modulus values of rocks nearby, and the existence of bedding joints had a negligible impact on ground squeezing. Overburden in the WS can be utilized as a reliable basis to alert engineers to implement mitigation measures during tunneling. The convergence values increased with increasing H, and the convergence ratio λ was generally stable after the critical overburden depth of 100 m was exceeded.

References:

Aydan Ö, Akagi T, Kawamoto T. The squeezing potential of rocks around tunnels; theory and prediction. Rock Mechanics and Rock Engineering, 1993, 26(2): 137-163.

Barton N. Shear strength criteria for rock, rock joints, rockfill and rock masses: Problems and some solutions. Journal of Rock Mechanics and Geotechnical Engineering, 2013, 5(4): 249-261.

Barla G. Tunnelling under squeezing rock conditions. Eurosummer-School in Tunnel Mechanics, Innsbruck, 2001: 169-268.

Barla G. Innovative tunneling construction method to cope with squeezing at the Saint Martin La Porte access adit (Lyon-Turin Base Tunnel), ISRM Regional Symposium-EUROCK 2009. International Society for Rock Mechanics, 2009.

Bilgin N, Algan M. The performance of a TBM in a squeezing ground at Uluabat, Turkey. Tunnelling and Underground Space Technology, 2012, 32: 58-65.

Einav I, Puzrin A M. Pressure-dependent elasticity and energy conservation in elastoplastic models for soils. Journal of Geotechnical and Geoenvironmental Engineering, 2004, 130(1): 81-92.

Fakhimi A, Salehi D, Mojtabai N. Numerical back analysis for estimation of soil parameters in the Resalat Tunnel project. Tunnelling and Underground Space Technology, 2004, 19(1): 57-67.

Hamidi J K, Bejari H, Shahriar K, Rezai B. Assessment of ground squeezing and ground pressure imposed on TBM shield. In: Proceedings of the 12th International Conference of International Association for Computer Methods and Advances in Geomechanics, Gao, India, 2008, 3907-3914.

Hejazi Y, Dias D, Kastner R. Impact of constitutive models on the numerical analysis of underground constructions. Acta Geotechnica, 2008, 3(4): 251-258.

Hoek E, Marinos P. Predicting tunnel squeezing problems in weak heterogeneous rock masses. Tunnels and tunnelling international Part 1 (November), 2000a, 32(11): 45-51.

Hoek E, Marinos P. Predicting tunnel squeezing problems in weak heterogeneous rock masses. Tunnels and tunnelling international Part 2 (December), 2000b, 32(11): 33-36.

Hoek E, Guevara R. Overcoming squeezing in the Yacambú-Quibor tunnel, Venezuela. Rock Mechanics and Rock Engineering, 2009, 42(2): 389-418.

Japan Railway Construction, Transport and Technology Agency. Design and construction standard for mountain tunneling, 2009 (in Japanese).

Japan Society of Civil Engineers. Japanese standard for mountain tunneling, 2006 (in

Japanese).

Jardine R J, Potts D M, Fourie A B, Burland J B. Studies of the influence of non-linear stress-strain characteristics in soil-structure interaction. Geotechnique, 1986, 36(3): 377-396.

Jiang Y, Xiao J, Tanabashi Y, Mizokami T. Development of an automated servo-controlled direct shear apparatus applying a constant normal stiffness condition. International Journal of Rock Mechanics and Mining Sciences, 2004, 41(2): 275-286.

Jiang Y, Tanabashi Y, Li B, Xiao J. Influence of geometrical distribution of rock joints on deformational behavior of underground opening. Tunnelling and underground space technology, 2006, 21(5): 485-491.

Jimenez R, Recio D. A linear classifier for probabilistic prediction of squeezing conditions in Himalayan tunnels. Engineering Geology, 2011, 121(3): 101-109.

Kakunai S, Masaki J, Kuroda R, Iwata K, Nagata R. Measurement of apparent Young's modulus in the bending of cantilever beam by heterodyne holographic interferometry. Experimental mechanics, 1985, 25(4): 408-412.

Karakus M. Appraising the methods accounting for 3D tunnelling effects in 2D plane strain FE analysis. Tunnelling and Underground Space Technology, 2007, 22(1): 47-56.

Kitagawa S. Behavior of Tunnel and Geological Property in the Squeezing Ground, Engineering Geology, 2003, Vol. 44(5), 294-302 (in Japanese).

Kitagawa S, Kajiwara Y, Shinji M. The multiplied tunnel support system applied to squeezing ground condition. Journal of Japan Society of Civil Engineers, 2002 (721): 27-39 (in Japanese).

Konda T, Okabayashi N, Noma S. Construction of mountain tunnel. Kajima Institute Publishing Co., Ltd., 1996: 31-32 (in Japanese).

Kovári K, Staus J. Basic considerations on tunnelling in squeezing ground. Rock mechanics and rock engineering, 1996, 29(4): 203-210.

Kulatilake P, Wang S, Stephansson O. Effect of finite size joints on the deformability of jointed rock in three dimensions. International journal of rock mechanics and mining sciences & geomechanics abstracts. Pergamon, 1993, 30(5): 479-501.

Kulatilake P, Park J, Um J. Estimation of rock mass strength and deformability in 3-D for a 30 m cube at a depth of 485 m at Äspö hard rock laboratory. Geotechnical & Geological Engineering, 2004, 22(3): 313-330.

Li Y, Jin X, Lv Z, Dong J H, Guo J C. Deformation and mechanical characteristics of tunnel lining in tunnel intersection between subway station tunnel and construction tunnel. Tunnelling and Underground Space Technology, 2016, 56: 22-33.

Li Z H, Zhu W C, Feng X T, Li S J, Zhou H, Chen B R. Effect of lateral pressure

coefficients on damage and failure process of horseshoe-shaped tunnel. Rock and Soil Mechanics, 2010, 31(2): 434-441.

Mezger F, Anagnostou G, Ziegler H J. The excavation-induced convergences in the Sedrun section of the Gotthard Base Tunnel. Tunnelling and Underground Space Technology, 2013, 38: 447-463.

Nasseri M H B, Rao K S, Ramamurthy T. Anisotropic strength and deformational behavior of Himalayan schists. International Journal of Rock Mechanics and Mining Sciences, 2003, 40(1): 3-23.

Okazaki K, ITO Y, Niwa H, Murayama H, Sasaya K, Obinata A, Kurahashi T. Research of the tunnel soundness diagnostic methods for the time-dependent deformation in tunnel. Engineering geology, 2016, 56(6): 308-315.

Panet M, Guenot A. Analysis of convergence behind the face of a tunnel. In: Tunnelling'82. IMM, London, 1982, 197–203.

Pulko B, Majes B, Logar J. Geosynthetic-encased stone columns: analytical calculation model. Geotextiles and Geomembranes, 2011, 29(1): 29-39.

Saari, K. Analysis of plastic deformation (squeezing) of layers intersecting tunnels and shafts in rock. Ph.D. Thesis, University of California, Berkeley, 1982.

Steiner W. Tunnelling in squeezing rocks: case histories. Rock mechanics and rock engineering, 1996, 29(4): 211-246.

Suzuki S, Furukawa K, Hieida M, Nakagawa K. A proposal on rationalization of experimental design technique under tunnel construction by NATM, Journal of Japan Society of Civil Engineers, 1993, 468, 47-56 (in Japanese).

Tanimoto, C. NATM-1. Morikita Shuppan, 1984, 168-185 (in Japanese).

The ministry of Public Works Research Institute Tunnel Laboratory. : Document Prediction and measurements manuals of ground deformation for tunnel excavation (plan), 1994. (in Japanese)

Urban Development Bureau of Hiroshima. Standard quantity surveying benchmark book of civil engineering, 2013 (in Japanese).

Vardakos S S, Gutierrez M S, Barton N R. Back-analysis of Shimizu Tunnel No. 3 by distinct element modeling. Tunnelling and Underground Space Technology, 2007, 22(4): 401-413.

Wang X, Kulatilake P, Song W. Stability investigations around a mine tunnel through three-dimensional discontinuum and continuum stress analyses. Tunnelling and Underground Space Technology, 2012, 32: 98-112.

Working group report of economic research subcommittee of Shinkansen tunnel: maintenance five, 1983: 38 (in Japanese).

Wu Q, Kulatilake P. REV and its properties on fracture system and mechanical properties, and an orthotropic constitutive model for a jointed rock mass in a dam

site in China. Computers and Geotechnics, 2012, 43: 124-142.

CHAPTER 5

Estimation of Reinforcing Effects of FRP-PCM Method on Degraded Tunnel Linings

5.1 Introduction

Repairing and reinforcing existing concrete structures, which represent a substantial portion of current infrastructure and building stocks, have become a major part of civil engineering activities, especially in the developed countries. Damages such as cracking, spalling, and water leakage occur frequently on degraded tunnels, which would significantly undermine the safety of tunnel operation. Since the degraded lining concrete cannot be easily replaced, in most repair works, reinforcing the tunnel linings requires the addition of external reinforcement materials.

Various types of methods have been developed to improve the integrity of lining concrete, typical ones of which are grouting reinforcement method, fiber reinforced shotcrete (FRS) method (De la Fuente et al., 2012; Chiaia et al., 2009; Chryssanthakis et al., 1997; Jeng et al., 2002; Franzén, 1992), carbon fiber sheet (CFS) method (Lee et al., 2002; Miyauch, 1997), steel board method (Kiriyama et al., 2005), and Fiber reinforcement plastic (FRP) method (Erki et al., 1993; Hensher, 2013; Asakura et al, 2003; Clarke et al., 1996). Comparing to other methods, FRP grids have several favorable properties such as high tensile strength, low weight, easy handling and application, immunity to corrosion, and minimal occupancy of space (Lau and Pam, 2010; Bournas et al., 2015). Past research has indicated that FRP grids bonded to the tensile side of flexural members can help increase the flexural capacity of reinforced concrete (RC) structures (Hensher, 2013). Therefore, in the past a few decades, FRP as a strengthening material for concrete structures has been increasingly utilized in engineering practices.

To fully explore the potential of FRP reinforcement, the reinforcing effect of FRP grids has been extensively investigated. Chen et al. (2003) and Yao et al. (2005) conducted single shear pull tests and used an anchorage strength model to estimate the effective bond length between FRP and concrete. Täljsten (1997) conducted double shear pull test on FRP reinforced concrete and the results showed that the strain limit of the concrete is the governing factor for the debonding failure. Pešić et al. (2003) predicted the load level at which FRP-plated concrete beams fail due to plate-end debonding based on finite element analysis. They found that the extent of strengthening

is limited by the shear capacity of concrete beams. Investigations on flexural capacity of reinforced concrete by FRP have also been reported in literature. Toutanji et al. (2006) developed a moment deflection model to evaluate the load carrying capacity of RC beams. Several other studies showed that the beams strengthened by FRP would avoid the debonding failure when a carefully designed anchorage is applied, resulting in a good flexural performance in terms of strength and ductility (Ceroni, 2010; Esfahani et al., 2007; Chajes et al., 1994; Wang et al., 2006). Arduini et al. (1997) and Buyukozturk (1998) numerically studied the load-deflection behaviors as well as the failure mechanism from ductile to brittle of pre-cracked RC beams. Berg et al. (2006) and Nystrom et al. (2003) focused on the FRP reinforcement on concrete structures from the cost-effective perspective. They concluded that FRP reinforcements could be cost-effective, given the savings in construction time and their potential long-term durability and maintenance benefits in the engineering fields such as bridge decks. Although extensive research efforts have been made to understand the shear and flexural strengthening effect of FRP materials, studies focusing on the reinforcing effects of FRP on degraded tunnel linings have not been reported.

In the present study, an FRP-PCM method was proposed and its applicable condition was estimated experimentally and numerically. First, direct shear tests were performed to determine the mechanical properties of the interface between PCM and concrete, bonded with an FRP layer. Then two-point bending tests and their numerical simulations were conducted to investigate the effects of FRP-PCM method on the bearing capacity of concrete beams. At last, numerical simulations based on Finite Difference Method (FDM) were performed to systematically analyze the reinforcing effects of FRP-PCM method on degraded tunnel linings, taking into account the influences of ground class, loosening pressure, concrete strength, and deterioration degree of lining concrete. Favorable conditions of applying FRP-PCM method to degraded tunnel linings were investigated and discussed.

5.2 Direct shear tests

5.2.1 Experimental setup

Direct shear test is one kind of typical testing methods for investigating the mechanical properties of different engineering materials, which provides direct and reliable estimations on the shear behaviors especially on shear strength of tested materials. In the present study, a digital-controlled shear testing apparatus was adopted to estimate the shear behavior of FRP-PCM reinforcement.

The outline of the fundamental hardware configuration of this apparatus is

described in Fig. 5.1, which consists of three units as follows:

(1) A hydraulic-servo actuator unit. The device consists essentially of two load jacks for applying almost uniform normal stress on the shear plane. Both normal and shear forces are applied hydraulic cylinders through a hydraulic pump which is servo-controlled. The loading capacity is 400 kN in both horizontal and holding arms. The applied normal stress can range from 0 to 20 MPa, which simulates field conditions from ground surface to about 800 m depths.

(2) An instrument package unit. In this system, three digital load cells (tension-contraction types, capacity 200 kN (normal), 400 kN (shear) for measuring shear and normal loads have been set with the rods connected at two sides of shear box (see Fig. 5.1)). Displacements are monitored and measured through LVDTs (linear variation displacement transducers), which are attached on top of the upper shear box.

(3) A mounting shear box unit. As shown in Fig. 5.2, a shear box consists of lower and upper parts, the upper box is fixed and joint is sheared by moving the lower box. The upper box is connected with a pair of tie rods and allows vertical movement and rotation. It is corresponding with the specimen of the different sizes between 100 mm and 500 mm.

This apparatus employed a nonlinear feedback of control and measurement on PC through a multifunctional analog-to-digital, digital-to-analog and digital input/output board (Jiang et al., 2004). This apparatus has been adopted in a great number of shear tests in previous studies, and has helped accurately estimate the shear behaviors of different materials (e.g., Jiang et al., 2004; Jiang et al., 2006). Here, the purpose of conducting direct shear test was to obtain the mechanical properties of the interface between the concrete layer representing the lining concrete of tunnels and the FRP-PCM layer that serves as a reinforcement component.

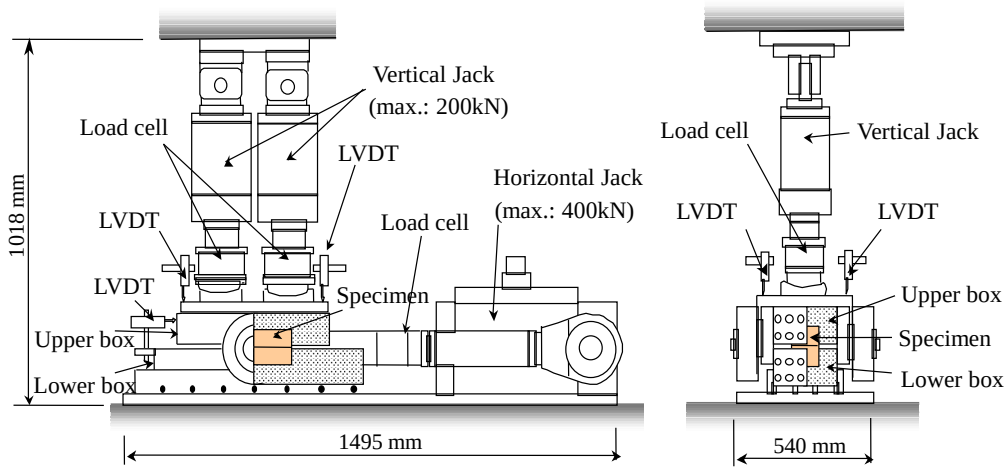

(a) (b)

Fig. 5.1 Digital-controlled shear testing apparatus: (a) side view and (b) front view (LVDT: linear variable differential transformer).

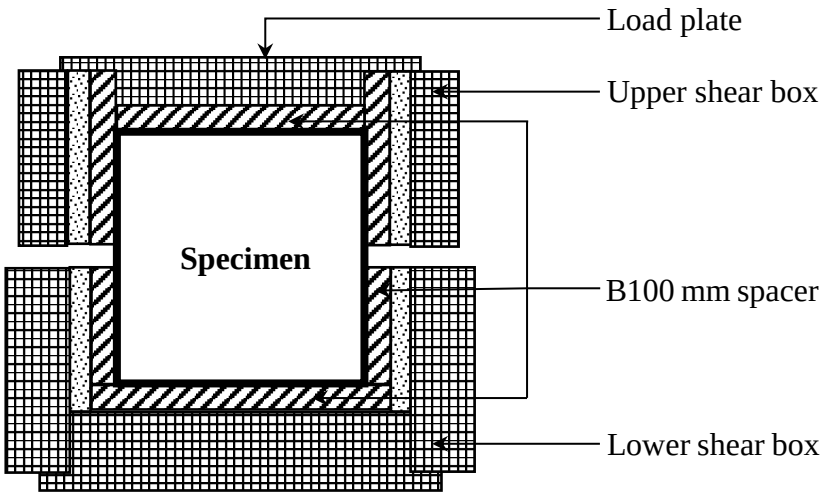

Dimensions: B100 mm × H100 mm

Fig. 5.2 Preparation of specimen for direct shear test.

Table 5.1 Properties of fiber reinforcement plastic grids and PCM material.

		Elastic modulus (MPa)	Compressive strength (MPa)	Tensile strength (MPa)	Cross-sectional area of mesh (mm^2)
FRP grid	CR4	100000	----	1400	6.6
	CR6				17.5
	CR8				26.4
PCM		26000	59.3	4.6	----

Three types of FRP grids (CR4, CR6, and CR8) that were made from identical material but have different cross-sectional areas of meshes were tested as shown in Table 5.1. The material properties of FRP grids and PCM tabulated in Table 5.1 were obtained from the unpublished reports of the manufacturing company of FRP grids. The procedure for sample preparation is as follows. First, concrete specimens with a length of 200 mm, a width of 100 mm, and a depth of 50 mm were manufactured by pouring the mixture of paste and aggregates into a rectangular metal mold along with vibration, and were cured for 14 days. The weight ratio of water, cement, fine aggregate and coarse aggregate is 1:1.70:5.08:3.75. In order to remove the top layer of paste to ensure a good adhesion between the concrete specimens and FRP grids, the top surfaces of concrete specimens were grinded with a sandpaper of type #600 until the aggregate was visible (approximately 1 mm) (Mazzotti et al., 2008). FRP grids with an area of 200 mm × 100 mm were then bonded to the top surfaces of the concrete specimens by

Sikadur-30 epoxy adhesive with a thickness of 1 mm. These specimens were again installed in another rectangular metal mold with the surface bonded with FRP grids facing upwards. PCM was then poured into the mold to accomplish the PCM-concrete specimens sandwiching an FRP layer. An example of specimen is shown in Fig. 5.3. Due to the meshed geometry of FRP grids, parts of PCM were directly bonded with the concrete. The dimension of PCM layer is identical to that of the concrete layer. The specimens were cured in a tank for another 14 days with a constant room temperature and humidity.

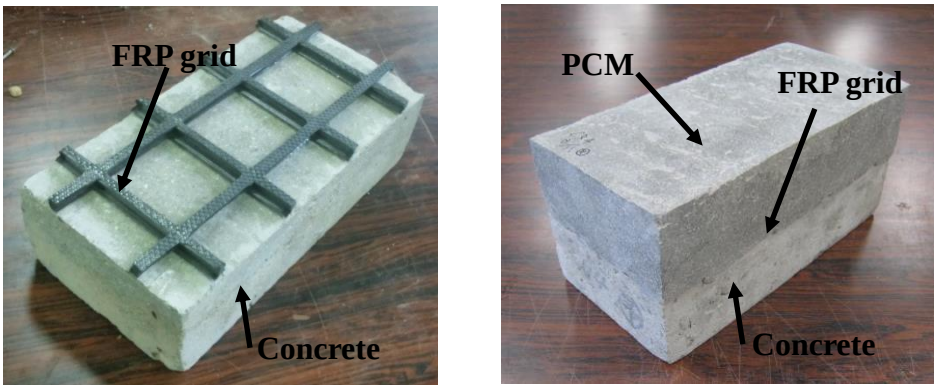

(a) (b)

Fig. 5.3 Photographs of specimen after bonding FRP grid to concrete layer (a), and after constructing the PCM layer (b).

The shear tests were conducted to investigate the overall mechanical properties of interface between the concrete layer and FRP-PCM layer based on orthogonal experimental design (OED) (Wu, 2013). The OED is a multi-factor experiment design method based on the orthogonal array, it selects representative points from full factorial experiment in a way that the points are distributed uniformly within the test range and thus can represent the overall situation, and is highly efficient for the arrangement of multi-factor experiment with optimal combination levels. The OED has the following characteristics: (1) use fractional factorial experiment instead of full factorial experiment; and (2) understand the full experiment through the analysis of fractional experiment (Ying, 2009; Li et al., 1997; Zhang et al., 2005). In the present study, the test cases as summarized in Table 5.2 were conducted. Shear tests were conducted under a constant normal load (CNL) boundary condition with a constant shear rate of 0.5 mm/min until the residual state was reached. In order to reduce the testing errors, each case was tested on 2 or 3 specimens. According to the unpublished reports of the manufacturing company, the shear bonding strength between the PCM-FRP layer and the concrete layer should be larger than 2.0 MPa under a normal stress greater than 2.0

MPa when being used a reinforcing material for tunnel linings (Research society of FRP grid construction method, 2007).

Table 5.2 Test cases.

Normal stress	CR4	CR6	CR8
1 MPa	◯	--	◯
2 MPa	◯	◯	--
3 MPa	--	◯	◯

5.2.2 Results and analysis

An example of the testing results of the cases reinforced with CR4 under the normal stresses of 1 MPa and 2 MPa and the cases reinforced with CR8 under the normal stresses of 1 MPa and 3 MPa is shown in Fig 5.4, which represents the measured relationship between the shear stress and the shear displacement. There were small gaps between the tested specimen and the shear box, resulting in an artificial pre-loading stage during which the gaps were gradually closed along with the increasing shear displacement. After the gaps were fully closed, the shear load then fully acted on the specimen. This pre-loading stage was deleted in Fig. 5.4, which is why the shear stress does not start from 0. The shear stress increases gradually until reaching the peak stress, then undergoes a quick drop after the failure of the bonding surface. The shear stress maintains almost constant value in the residual stage, since the PCM layer was merely sliding on the concrete layer in this stage. The average values of the maximum shear stress were obtained as 2.7 MPa under the normal stress of 2 MPa, and 3.3 MPa under the normal stress of 3 MPa, which are larger than the target value of 2 MPa, indicating that tested FRP grids have sufficient strength to be used for lining reinforcement.

The shear stiffness of bonding surface could be obtained from the following equation:

$$\Delta\tau = k_s \times \Delta u \tag{5.1}$$

where, $\Delta\tau$ is the increment of shear stress, Δu is the increment of shear displacement, k_s is the shear stiffness of bonding surface. Although the shear stiffness of bonding surface increased with the increment of normal confining stress, the normal confining stress acting on tunnel linings was difficult to determine due to the variations of working conditions in practical use, such as loosening pressure acting on tunnel lining, ground class, lining deterioration degree, tunnel health degree, and etc. In order to simplify the calculation, the average values of shear stiffness were obtained as 5.30×10^3, 6.39×10^3, and 7.37×10^3 MPa/m for the reinforcements of CR4, CR6, and CR8, respectively, based

on the shear stress-shear displacement curve before reaching the peak shear stress of each case.

Fig. 5.5 shows the relations between peak and residual shear stresses with normal stress for all cases tested. The value of residual shear stress was taken when the shear stress became constant, which typically happened when the shear displacement were larger than 1.5 mm. Linear regression with the average values of shear stress at each normal stress was applied to obtain the cohesion and frictional angle at peak and residual states as follows:

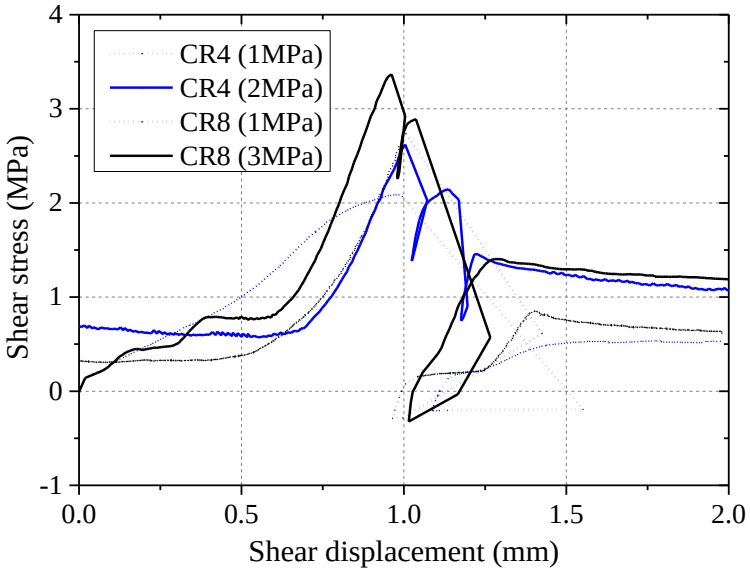

Fig. 5.4 Typical results of shear test.

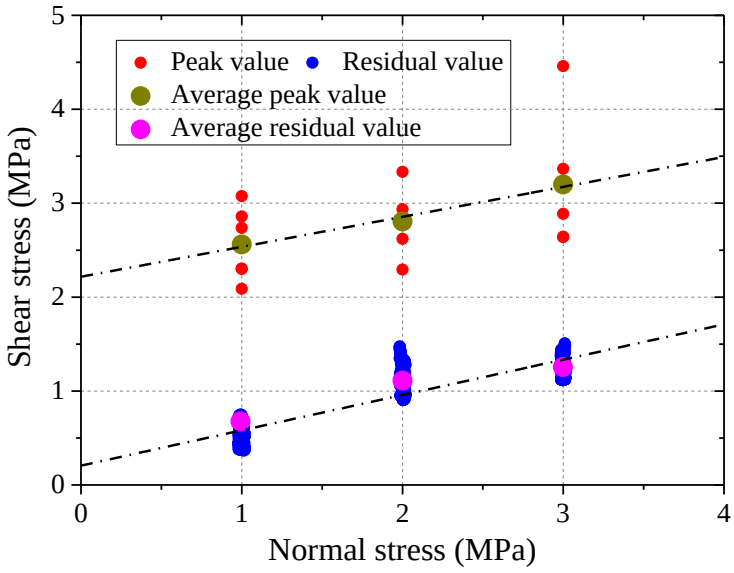

Fig. 5.5 Test results of shear stress and residual stress vs. normal stress.

$$\tau_{peak} = 0.32\sigma + 2.22 \quad (5.2)$$

$$\tau_{res} = 0.29\sigma + 0.43 \quad (5.3)$$

Then, we obtained the cohesion and friction angle at peak and residual states as c_{peak} = 2.22 MPa, φ_{peak} = 17.7°, c_{res} = 0.43 MPa, and φ_{res} = 16.1°. The cohesion of bonding surface diminished dramatically after failure, and the friction angle showed a slight decrease. After failure, the bonding surface of PCM layer and concrete layer became a smooth plane (see Fig. 5.6) between which the cohesion approached 0. These values were later used in the numerical simulations.

Fig. 5.6 Photograph of specimen after failure.

5.3 Bending tests on reinforced beams and related numerical simulations

5.3.1 Experimental setup

Bending tests on concrete beams were carried out to verify the improvement of bearing capacity with FRP-PCM method on concrete structures. The tested beams have a length of 2000 mm, a width of 200 mm and a height of 300 mm. The cross-sectional view of the reinforcements including steel bar and FRP-PCM, and the arrangements of applied loading and supporting positions are shown in Fig. 5.7. Two jacks were installed on the top surface of the beams with a distance of 400 mm, which is 1/5 of their total length. The beams were initially reinforced by 5 main reinforcing steel bars (D10-SD295) placed on the upper part together with regularly spaced hoops (D13-SD345). The FRP-PCM reinforcement was later constructed on the bottom surface of the reinforced beam with a thickness of 15 mm.

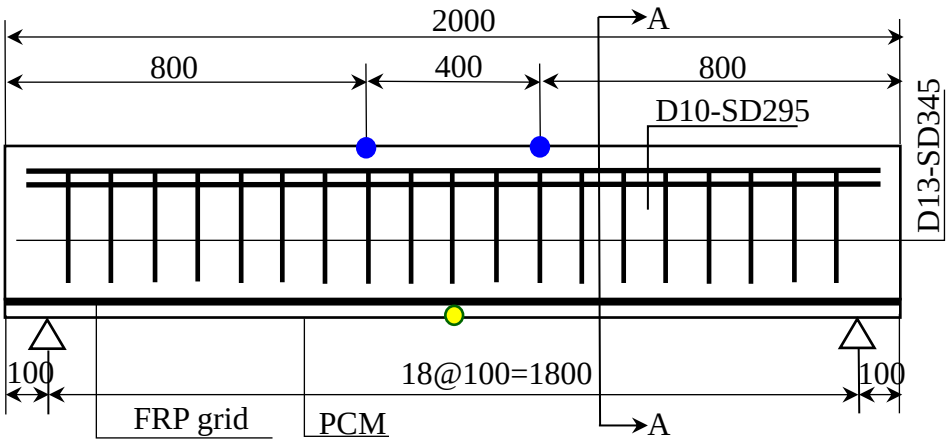

(a) Dimension and reinforcement of tested beams

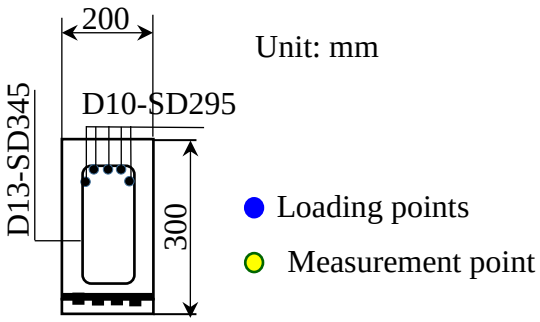

(b) Cross-sectional view of A-A

Fig. 5.7 Structure of tested beams and arrangement of loading and measurement.

A case without FRP-PCM reinforcement, and a case reinforced by CR6 grids, were tested, respectively. The compressive strength and elastic modulus of concrete were obtained from uniaxial compression test as summarized in Table 5.3, and the Poisson's ratio was obtained from the triaxial compression test as tabulated in Table 5.3. The properties of FRP-PCM reinforcement that obtained through the direct shear test as described in the last section are summarized in Table 5.4.

Table 5.3 Property of concrete.

Compressive strength σ_c (MPa)	Tensile strength σ_t (MPa)	Poisson's ratio ν	Elastic modulus E (MPa)
20.8	2.12	0.2	27220

Table 5.4 Property of reinforcement materials.

Reinforcement materials	Internal frictional angle φ_s (deg)	Cohesion c_s (MPa)	Shear stiffness k_s (MPa/m)
CR6+PCM	17.7	2.22	6.39×10^3

5.3.2 Numerical models

Numerical modelling of bending tests on reinforced concrete beams have received extensive practices in literature, focusing especially on the mechanism of failure and cracking process in the beams during loading (Li et al., 2006; Kishi et al., 2005; Martinola et al., 2010; Sumarac et al., 2003). The present study aimed to investigate the reinforcing effect of FRP-PCM method on tunnel linings, therefore, a numerical method that can well reproduce the behavior of reinforcements applied to both bending tests and tunnel linings was required. Here, the finite difference method (FDM) was adopted to simulate the bending tests on concrete beams, in which the Mohr-Coulomb failure criterion was adopted to represent the elastic/plastic deformation behaviors of concrete. The reinforcements with FRP grids and PCM were reproduced by liner element with a composite section that also follow the Mohr-Coulomb failure criterion.

In the Mohr-Coulomb, the tensile strength of materials can be calculated as follows:

In labeling the three principal stresses so that

$$\sigma_1 \le \sigma_2 \le \sigma_3 \tag{5.4}$$

this criterion may be represented in the plane (σ_1, σ_3) as illustrated in Fig. 5.8.

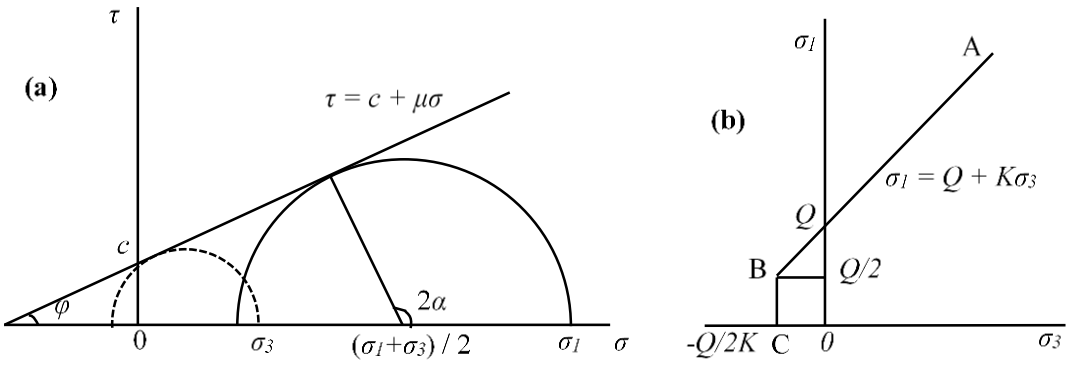

Fig. 5.8 Mohr-Coulomb failure criterion: (a) Shear stress and (b) Principal stress.

In the Mohr-Coulomb failure criterion, the maximum shearing stress τ_s can be determined by cohesion c and internal frictional angle φ as follows:

$$\tau_s = c + \mu\sigma \tag{5.5}$$

where, μ is the internal friction coefficient, $\mu = \tan\varphi$; σ is the normal stress at the failure surface. The failure criterion can be expressed in terms of the relationship between the principal stresses. From the geometry of the Mohr circle as shown in Fig. 5.8(a),

$$sin\varphi = \frac{(\sigma_1 - \sigma_3/2)}{c\cot\varphi + (\sigma_1 + \sigma_3)/2} \tag{5.6}$$

Rearranging,

$$\sigma_1 = \sigma_3\left(\frac{1+\sin\varphi}{1-\sin\varphi}\right) + 2c\frac{\cos\varphi}{1-\sin\varphi} \tag{5.7}$$

Then,

$$\sigma_s = Q + K\sigma_3 \tag{5.8}$$

where,

$$K = \tan^2\alpha \tag{5.9}$$

$$Q = 2c\tan\alpha \tag{5.10}$$

The shear failure envelope is defined from point A to B by the Mohr-coulomb criterion as shown in Fig. 5.8(b).

The minor principle stress in the dashed circle as shown in Fig. 1-1(a) was defined as tensile strength,

$$\sigma_3 = -c\cot\alpha = -Q/(2K) \tag{5.11}$$

The corresponding major principle stress $\sigma_1 = c\tan\alpha = Q/2$, which was corresponded to the point B as shown in Fig. 5.8(b), and the tensile failure envelop was determined from point B to C. when the tensile strength of materials was greater than $\sigma_3 = -c\cot\alpha$, tensile failure occurs. Herein, σ_3 is the tensile strength limit of materials that determined by the Mohr-Coulomb failure criterion (MPa), c is the cohesion of materials (MPa), and α is the internal friction angle of materials (°). This method allows materials undergoing large deformations and provides more realistic representation of behavior of materials (Itasca, 2002). It is also convenient to simulate large-scale structures such as tunnels as presented in Section 5.4. The dimension and boundary condition of numerical models are identical to the experimental models.

5.3.3 Results

Fig. 5.9 shows the photograph of a tested beam during loading process, and Fig.

5.10 shows the photographs of tested beams after failure and the tensile failure zones of these beams obtained from numerical analysis. Herein, it was noted that the photos on the left column of Fig. 5.10 showed the test results at the ultimate failure state, in which, failures of concrete beams occurred at the peak loads of 20.01 kN (unreinforced case) and 27.41 kN (CR6 reinforced case), respectively. Loading was still applied to these beams until the ultimate loads of 27.44 kN (Unreinforced case) and 51.33 kN (CR6 reinforced case) were reached. Since the finite difference method (FDM) is based on a continuous mechanism, only the deformation of concrete beams in the pre-peak stage could be well reproduced in the numerical simulations. The simulation results on the right column of Fig. 5.10 showed the tensile failure zones at the peak failure state, and the corresponding peak loads were 20.10 kN (unreinforced case) and 30.01 kN (CR6 reinforced case), respectively.

Fig. 5.9 An example of concrete beam during loading.

The cracks shown on the numerical models are sketches of the observed cracks on the experimental models. For all cases, two main vertical cracks were generated in the central part of beams after failure, which initiated at the bottom boundary of beams, propagating gradually upwards, and finally leading to the macroscopic failure of beams. Plenty of smaller cracks were also generated near the bottom of the beams. Since the FDM is based on a continuous mechanism, the numerical models can not represent the cracking processes in the beams. As an alternative, it can be confirmed that all of the generated cracks were located within the tensile failure zones predicted by the numerical models (Figs. 5.10(b) and (d)). After failure, the bonding between reinforcement layer and concrete layer was destructed, resulting in the separation between the two layers as shown in Figs. 5.10(a) and (c).

Fig. 5.11 shows the load-deflection curves obtained from tests and simulations. For all cases, the load increased rapidly with the increasing deflection in the initial loading stage (less than 1 mm) until reaching a peak load, followed by a yielding stage during which the load increased at a much smaller gradient comparing to the initial

stage. Sudden drops of load could be observed on the curves obtained from test, due to the propagation of the main cracks. Compared with the unreinforced case, the strength of reinforced beam with CR6 grids was improved by around 40%. Ductility of a concrete beam can be defined as its ability to sustain inelastic deformation without loss in loading capacity, prior to failure. In the present study, the ductility of concrete beams was quantitatively investigated in terms of deformation that obtained from bending tests, and it was defined as the ratio of ultimate deformation to the deformation at the peak load in the mid-span of concrete beams (Grace et al., 1999; Rashid et al., 2005). The results showed that the ductility for the unreinforced case and reinforced case (CR6) were 34.13 and 17.56, respectively. It was revealed that the ductility of reinforced beam by FRP grids was decreased by around 50% (Toutanji et al., 2006).

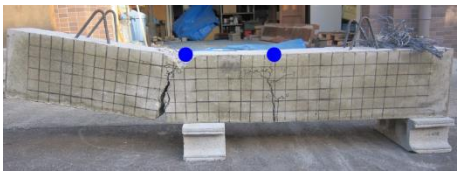

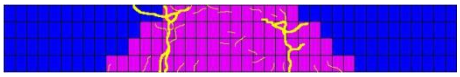

(a) Test (unreinforced)

(Peak load: 20.01 kN, deflection: 0.23 mm)
(Ultimate load: 27.44 kN, deflection: 7.85 mm)

(b) Simulation (unreinforced)

(Peak load: 20.10 kN, deflection: 0.34 mm)

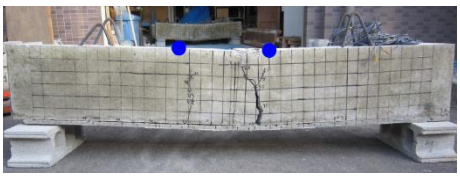

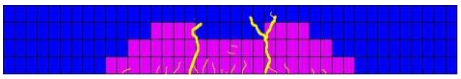

(c) Test (CR6)

(Peak load: 27.41 kN, deflection: 0.54 mm)
(Ultimate load: 51.33 kN, deflection: 9.48 mm)

(d) Simulation (CR6)

(Peak load: 30.01 kN, deflection: 1.35 mm)

Fig. 5.10 Photographs of tested beams and tensile failure zones of these beams obtained from numerical simulation.

The numerical results showed a similar tendency of load – deflection curves with those of the test results, which revealed that the numerical simulation well reproduced the behavior of beams with or without reinforcement in the initial stage until peak load. However, the numerical simulation failed to represent the undulations of curves in the residual stage, since cracking process dominated the failure mechanism in this stage which was not reproduced by the numerical simulation. More sophisticated numerical methods may be required if investigating the cracking processes in beams is the

principal purpose. In the present study, performance of the adopted numerical method is acceptable since the strengthening effect of FRP-PCM method has been well reproduced.

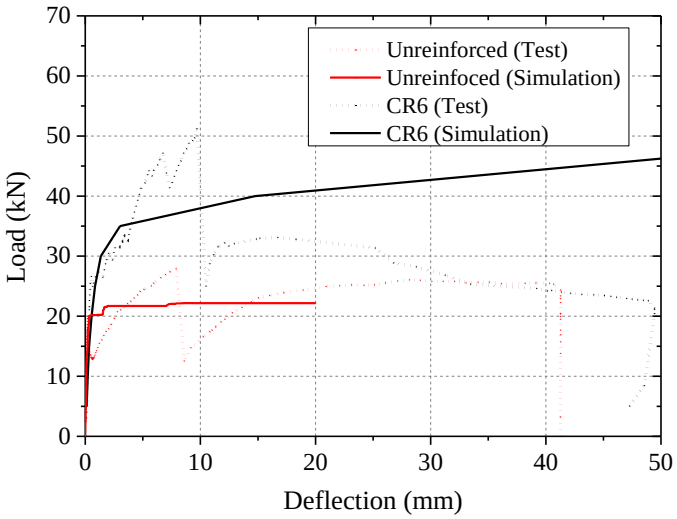

Fig. 5.11 Load-deflection curves of testing and simulation results of bending test on concrete beams.

5.4 Numerical simulation of degraded tunnels reinforced by FRP-PCM method

Tunnels commissioned for many years would suffer damages in different degrees, especially on the lining concrete such as cracking and spalling. In this section, numerical simulation on tunnels reinforced by FRP-PCM method was implemented, in order to analyze the effects of several important influential factors of damages on the integrality of tunnel linings, and to establish applicable conditions for FRP-PCM method.

5.4.1 Numerical Model

The numerical model of a typical tunnel constructed by fore-piling method was established using FDM as shown in Fig. 5.12. Mountain tunnels constructed by fore-piling method typically encounter an unfavorable condition that cavities exist between lining and surrounding rock masses (Asakura et al., 2000; Matsunaga et al., 2005; Uno et al., 2012; Kojima et al., 2014). In light of this, a cavity was presumed to exist on the crown of the model with an arc range of 90° with respect to the center point of the tunnel, with a thickness of 30 cm. Thickness of lining was typically 45 cm, which was

reduced to 15 cm on the central crown due to the existence of the cavity. In addition to FRP-PCM reinforcement, back-filling was also applied to the cavity. The reinforced region by FRP-PCM method covered an arc length of 120° on the upper wall of tunnel as shown in Fig. 5.12. The horizontal distance from the wall of tunnel to the boundary of model was determined as 2*D* (*D* is the excavation diameter of the tunnel that is equal to 10 m), since it has been confirmed that its simulation result is almost identical to a larger model with such horizontal distance of 5*D*. Reducing the distance from 5*D* to 2*D* could remarkably reduce the computational time. The numerical model was constructed by 1978 elements and 4116 nodes. The tunnel lining was reproduced by the finite element mesh that followed the Mohr-Coulomb failure criterion, while the reinforcement effects with FRP grids and PCM were investigated by the liner element with a composite section that also followed the Mohr-Coulomb failure criterion (Itasca, 2002). The left and right sides were roller boundaries, and the bottom boundary was fixed with no rotation and displacement. Three classes of ground (CII, DI and DII) were selected as the host rock masses in the numerical simulations, which are composed by the medium hard and soft rocks typically encountering in tunnel constructions in Japan (The Ministry of Public Works Research Institute Tunnel Laboratory, 1994). Urethane materials were selected as the back-filling materials due to their quick hardening properties and high strength. Properties of ground, lining, and back-filling materials are tabulated in Table 5.5.

Since the target of present study is degraded tunnels, deterioration degree was defined to represent the degraded level of lining concrete comparing to the original strength, which can significantly influence the deformation and failure behaviors of tunnels. The deterioration degrees were selected as 50%, 67% and 80%, representing that the elastic modulus E, the compressive strength σ_c, the tensile strength σ_t, cohesion c and the tangent value of internal frictional angel φ were reduced to 1/2, 1/3, and 1/5 of their original values based on the strength reduction method (Yu et al., 2009; Zhu, 2007), as tabulated in Table 5.6. We also considered another unfavorable condition that due to the existence of the cavity, the rock mass located above the cavity would undergo large deformation that may exert an excessive pressure on the lining. This pressure was defined as loosening pressure, which represented a certain height of rock mass (loosening height) that exerted its self-weight on the lining. Numerical simulation cases are summarized in Table 5.7.

Table 5.5 Properties of ground, lining and back-filling material.

Property	Ground class			Lining	Back-filling material
	CII	DI	DII		
γ (kN/m^3)	22.6	21.6	20.6	24.0	9.8
E (MPa)	980	490	147	24500	12.0
v	0.30	0.35	0.35	0.20	0.13
c (MPa)	0.98	0.49	0.196	6.99	0.50
φ (deg)	40.0	35.0	30.0	40.0	10.0
σ_t (MPa)	0.42	0.19	0.06	3.00	0.20

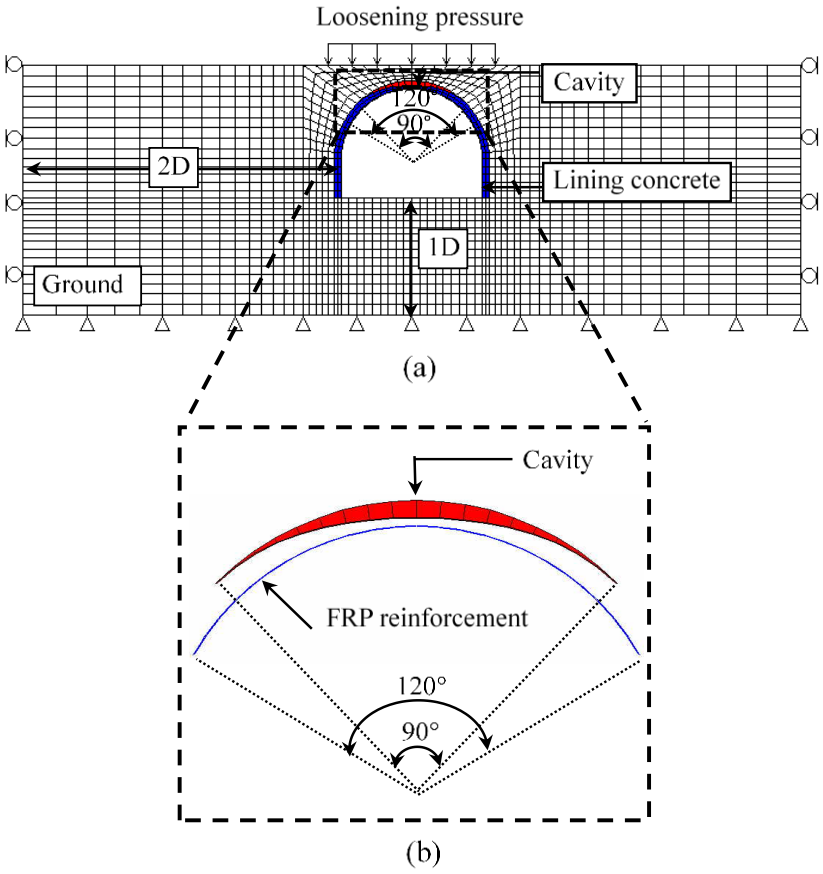

Fig. 5.12 Schematic diagram of numerical model of a degraded tunnel with the existence of a cavity above the crown (D: 10 m): (a) Overview of numerical model, (b) Locations of cavity and FRP reinforcement.

Table 5.6 Property of lining with different deterioration degrees.

Deterioration degree	E (MPa)	σ_c (MPa)	c (MPa)	φ (deg)	σ_t (MPa)
0%	24500	30.0	6.99	40.0	3.0
50%	12250	15.0	3.50	22.76	1.5
66.7%	8166.67	10.0	2.33	15.63	1.0
80%	4900	6.0	1.40	9.53	0.6

Table 5.7 Numerical simulation cases.

Lining thickness	FRP grid	Loosening height	Ground class	Deterioration degree of lining
15.0 cm	Unreinforced	3 m	CII	0%
	CR4	6 m	DI	50%
	CR6	10 m (1D)	DII	66.7%
	CR8			80%

5.4.2 Assessment of reinforcing effects

Both the axial stress that is parallel to the wall of the tunnel and the radial stress that is perpendicular to the tunnel wall have significant influences on tunnel lining deformations. However, according to the numerical simulations in the present study, the axial stress is approximately two orders of magnitude larger than the radial stress. Therefore, the reinforcing effects with FRP-PCM method were analyzed according to the variations of axial stress. In order to estimate the reinforcing effect of FRP-PCM method quantitatively, an axial stress reduction rate R_σ was defined as

$$R_\sigma = \frac{\sigma_{nr} - \sigma_r}{\sigma_{nr}} \times 100\% \tag{5.12}$$

where, σ_{nr} is the axial stress acting on the unreinforced lining (MPa), and σ_r is the axial stress obtained in reinforced cases (MPa). Axial stress is the principal stress oriented parallel to the wall of tunnel, and the axial stress reduction rate represents the degree the axial stress is reduced by reinforcement.

Fig. 5.13 shows simulation results of the axial stress reduction rate for the ground classes of CII and DII. R_σ increased with the increasing loosening height, revealing that the performance of reinforcement was greater when higher loosening pressure was acting on the lining. This improvement seemed to vanish when the loosening height was larger than 1D. Higher grade of FRP grids (i.e., CR8), greater deterioration degree

(i.e., 80%), and higher class of ground (i.e., CII) led to better reinforcing effect. These results confirmed that the FRP-PCM method has good reinforcing effects on degraded tunnel linings.

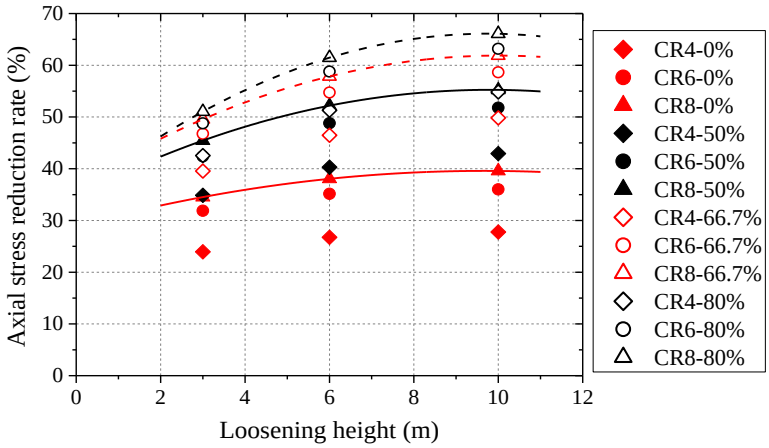

(a) Ground class: CII

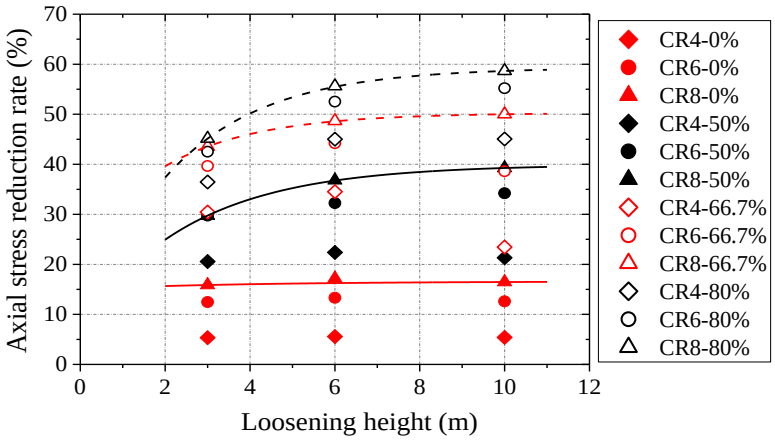

(b) Ground class: DII

Fig. 5.13 Relationship between axial stress reduction rate and loosening height.

Beside axial force, the bonding strength between reinforcement and lining concrete is another important factor that significantly impacts on the performance of reinforcement. Here, a safety factor of bonding surface was defined as

$$f_s = \frac{\tau_{\max}}{\tau_c} \tag{5.13}$$

where f_s is the safety coefficient, τ_c is the calculated value of shear stress acting on bonding surface, and τ_{max} is the theoretical value of shear stress at failure.

As shown in Fig. 5.14, the safety factor of bonding surface decreased with the

increasing loosening height, when the ground classes were CII and DII. This revealed that the reinforcing effect was reduced when greater loosening pressure was acting on the lining. Obviously the deterioration degree also reduced the safety factor in some contents, the influence of which was smaller than that of the loosening height.

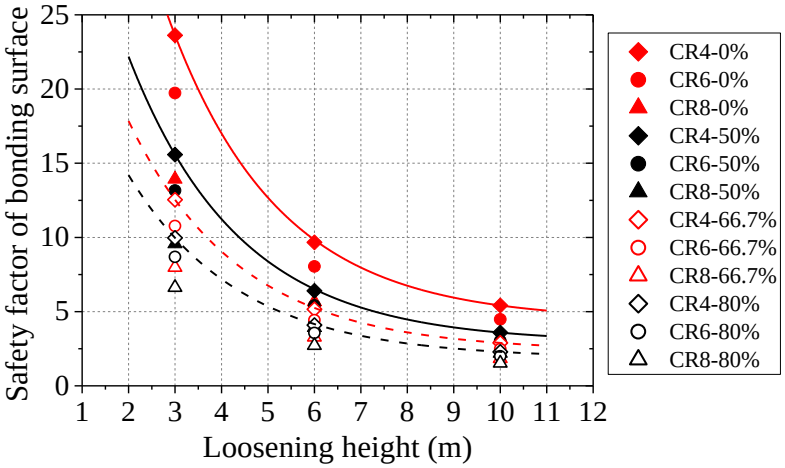

(a) Ground class: CII

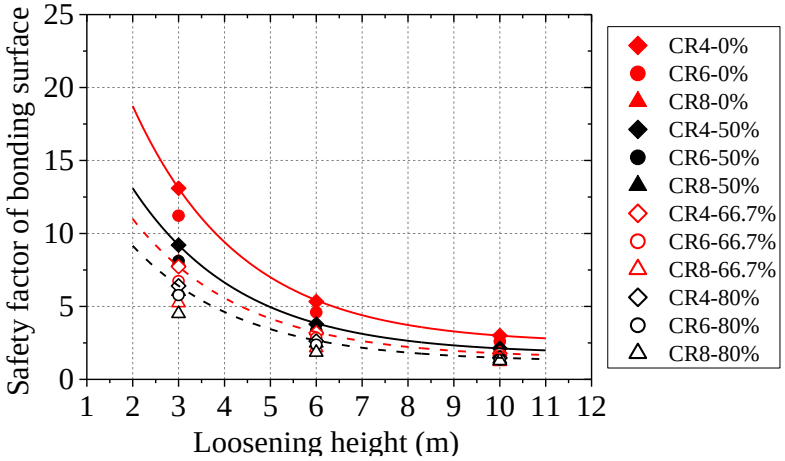

(b) Ground class: DII.

Fig. 5.14 Relationship between safety factor of bonding surface and loosening height.

5.4.3 Assessment of applicable conditions for FRP-PCM method

When the integrity of a tunnel lining drops below some critical values, measures need to be taken to improve the stability and safety of the tunnel. To do so, a guideline is required to help select the right type of reinforcement that could best restore the integrity of damaged linings. In the present study, the critical value of the compressive strength of lining concrete was selected as an indicator for health assessment of tunnel linings according to the design guideline as shown in Table 5.8 (East Nippon

Expressway Company Limited., Central Nippon Expressway Company Limited., West Nippon Expressway Company Limited, 2006). In this table, health degree "AA" indicates that the studied tunnel lining undergoes severe damages that need to be repaired immediately; "A" indicates that the current damage on tunnel lining is limited but has high potential to develop, thus the tunnel needs further monitoring and investigation; "OK" indicates that the tunnel lining is in healthy condition that does not need reinforcement. σ_{ck} is the designed strength of lining concrete, and the critical incremental stress represents the maximum stress increment allowed for a tunnel lining due to the effects of some external unfavorable conditions, such as the impact of loosening pressure on lining and the disturbance of stress state due to a nearby excavation. In the present study, we considered the loosening pressure as the only source of external force that results in the increase of stress acting on tunnel lining. For a tunnel lining with a health degree of "AA", when the incremental stress reaches $0.1\sigma_{ck}$, reinforcement is considered as necessary. Here, a dimensionless stress was defined as:

$$\sigma' = \frac{P_L}{\gamma D} \times \frac{\Delta\sigma_a}{\sigma_{cf}} \tag{5.14}$$

$$\alpha_1 = \frac{P_L}{\gamma D} \tag{5.15}$$

where, σ' is the dimensionless stress, $\Delta\sigma_a$ is the simulation result of incremental axial stress acting on the crown of lining due to the loosening pressure (Pa), σ_{cf} is the critical value of incremental compressive strength that equals to $0.2\sigma_{ck}$ for "A" and $0.1\sigma_{ck}$ for "AA" (Pa), P_L is the loosening pressure (Pa), γ is the unit weight of surrounding rock masses (N/m^3), D is the diameter of tunnel (m), and α_1 is the incremental coefficient of stress resulting from the loosening pressure. In Eq. (5.14), when σ' is larger than α_1, then σ_a becomes larger than σ_{cf}, indicating that reinforcement is required, or a higher level of reinforcement is required for the studied tunnel lining.

Relations between the dimensionless stress and the loosening height for lining deterioration degrees of 0%, and 66.7%, ground classes of CII, DI and DII, health degree of "A", are shown in Fig. 5.15. Unreinforced case was simulated along with reinforced cases using FRP grids CR4, CR6, and CR8. The change of α_1 with the changing loosening height is drawn in a straight line, while the relations between dimensionless stress and loosening height are presented as a series of curves. If the curves are over the straight line, then the studied tunnel lining needs to be reinforced. Greater deterioration degree of lining and larger loosening height lead to larger values of dimensionless stress. Better reinforcing effect could be achieved when an FRP grid with a higher grade (i.e., CR8) is applied to a tunnel with lower class of ground (i.e., DII), as shown in Figs. 15(b), (d) and (f).

By searching for the intersecting points of the straight line and the curves shown in Fig. 5.15, the critical loosening height was obtained for each case. Figs. 5.16 and 17 show the applicable condition for FRP-PCM method to tunnel linings with health degrees of “A” and “AA”. Suitable types of FRP grids can be selected to improve the tunnel linings under various operating conditions in practices according to these figures. For instance, when the health degree is “A”, the rock mass class is DII, the compressive strength of lining concrete is 10 MPa, and the loosening height is 6 m, reinforcement could be applied with a lower grade of FRP grid such as CR4 (Fig. 5.16(c)). In contrast, in the condition that the health degree is “AA”, the rock mass class is DII, the compressive strength of lining concrete is 15 MPa, and the loosening height is 5 m, FRP grid of CR6 and above grade should be selected (Fig. 5.17(c)).

Table 5.8 Critical value of incremental stress acting on lining for different health degrees of tunnel lining (East Nippon Expressway Company Limited., Central Nippon Expressway Company Limited., West Nippon Expressway Company Limited., 2006). σ_{ck} is the strength of lining concrete.

Health degree of tunnel lining	Critical incremental compressive stress (MPa)	Critical incremental tensile stress (MPa)
OK	$0.3\sigma_{ck}$	$0.06\sigma_{ck}$
A	$0.2\sigma_{ck}$	$0.04\sigma_{ck}$
AA	$0.1\sigma_{ck}$	$0.02\sigma_{ck}$

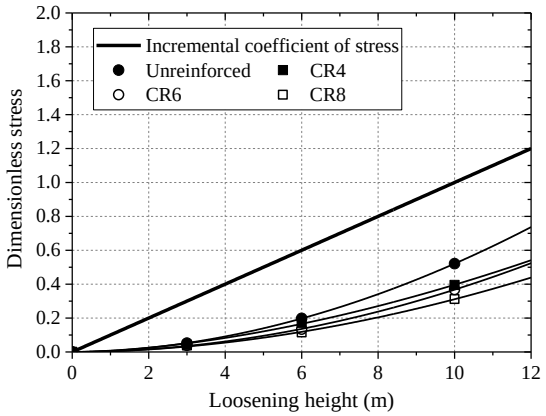

(a) Ground class: CII

Deterioration degree: 0%

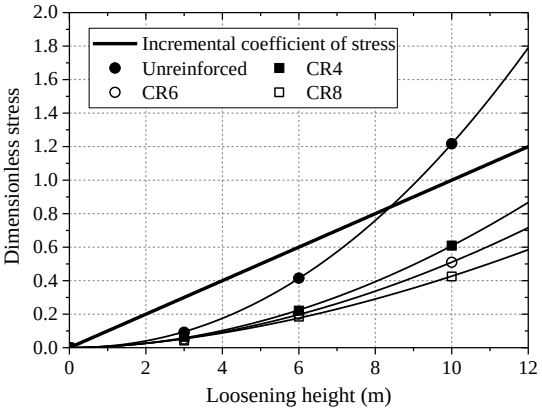

(b) Ground class: CII

Deterioration degree: 66.7%

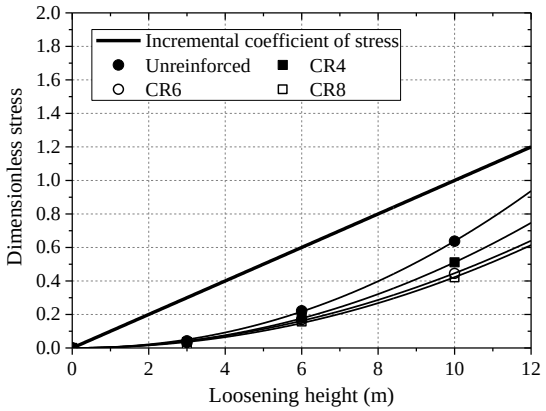

(c) Ground class: DI

Deterioration degree: 0%

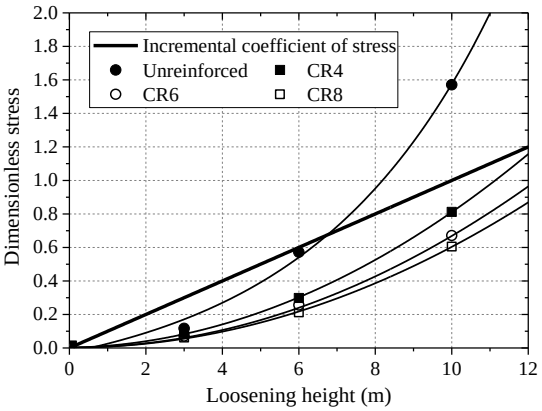

(d) Ground class: DI

Deterioration degree: 66.7%

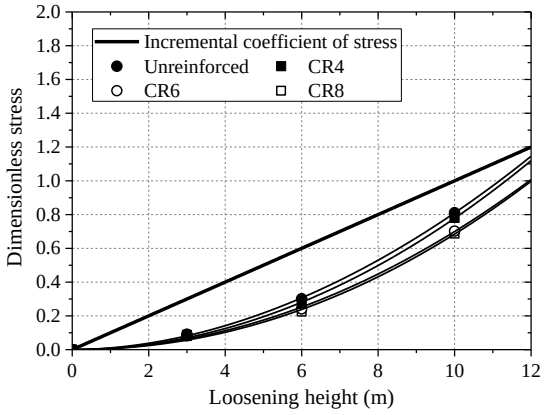

(e) Ground class: DII

Deterioration degree: 0%

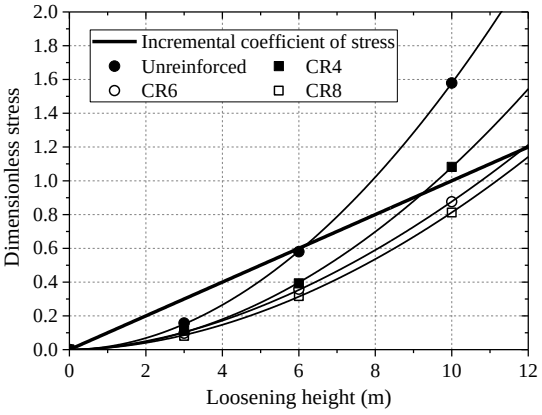

(f) Ground class: DII

Deterioration degree: 66.7%

Fig. 5.15 Relationship between dimensionless stress with loosening height (Health degree: “A”).

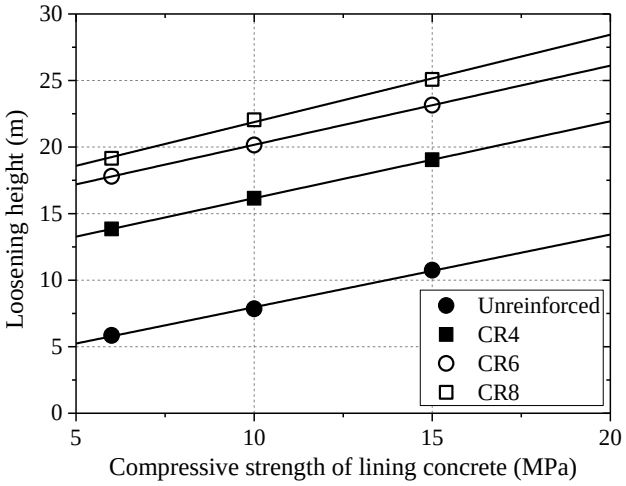

(a) Ground class: CII

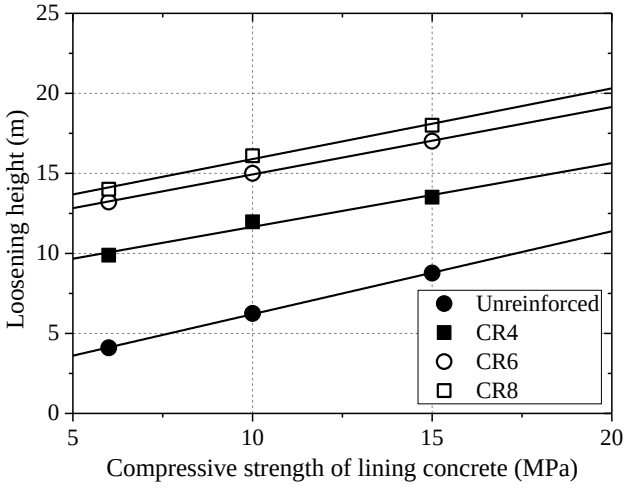

(b) Ground class: DI

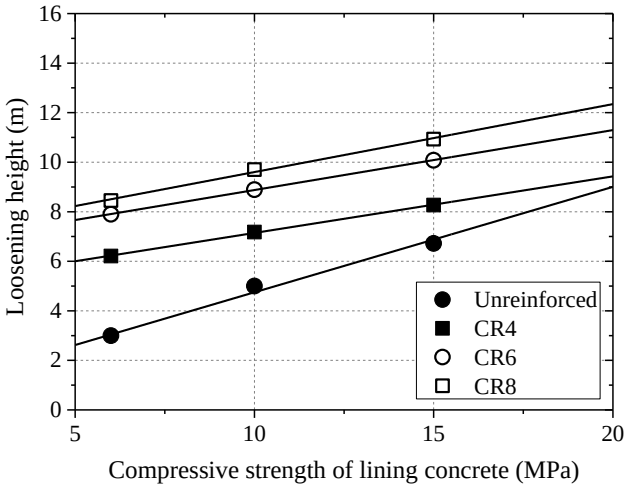

(c) Ground class: DII

Fig. 5.16 Proposed guideline for deciding applicable condition of FRP-PCM method (Health degree: “A”).

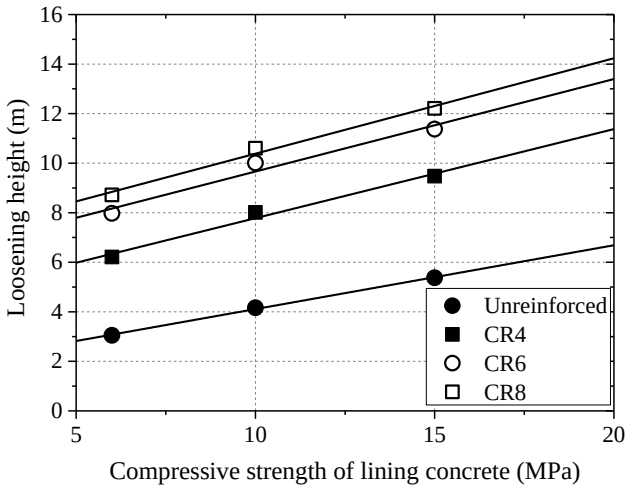

(a) Ground class: CII

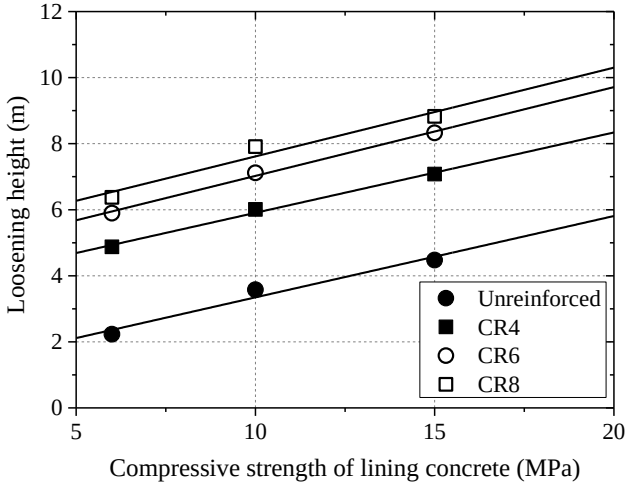

(b) Ground class: DI

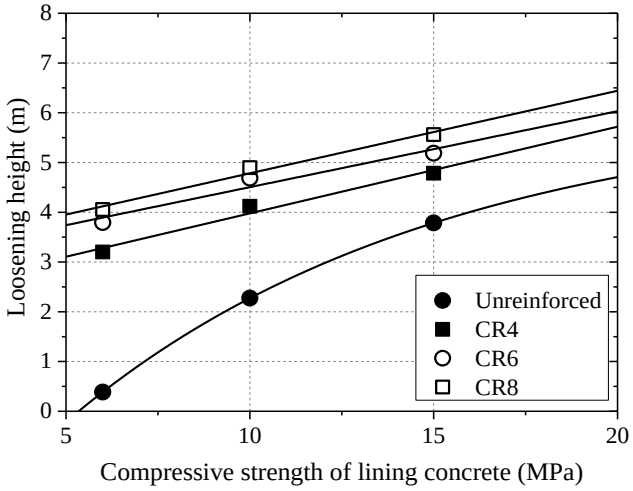

(c) Ground class: DII

Fig. 5.17 Proposed guideline for deciding applicable condition of FRP-PCM method (Health degree: “AA”).

5.5 Conclusions

First, a series of direct shear tests were conducted on PCM-concrete specimens embedded with an FRP layer with different grades, and fundamental mechanical properties of FRP-PCM reinforcement, such as shear stiffness, cohesion, and friction angle were obtained, which were later used in numerical simulations. Then, bending tests were conducted on concrete beams reinforced by FRP-PCM method to directly investigate its reinforcing effects on concrete structures. Finally, numerical simulations on degraded tunnels undergone loosening pressure were implemented, and applicable condition of FRP-PCM method to tunnels with different health degree, ground class, loosening pressure, and concrete strength was investigated.

The performance of different grades of FRP grids was confirmed through the comparison of their direct shear test results, which showed that greater shear strength of FRP-PCM reinforcement could be achieved by using a higher grade of FRP grid. The bearing capacity of concrete beams reinforced with FRP grids (CR6) obtained from bending test was improved by around 40% comparing to the unreinforced beam. These experiments have revealed that the FRP-PCM method has good performance in reinforcing the concrete structures. In the numerical model of tunnels, the existence of cavity above crown was considered which could exert an external loosening pressure originating from the weight of rock mass above the cavity to the tunnel lining. This is one of the commonly observed unfavorable conditions for aged tunnels in Japan constructed by fore-piling method. Simulation results showed that the FRP-PCM method could efficiently reduce the axial stress acting on tunnel lining, and such effect is greater for tunnel linings with larger deterioration degree. Degraded tunnel linings were classified into three health degrees, and reinforcement is required when the increased compressive stress acting on tunnel lining due to the effect of external unfavorable conditions exceeds some critical values. Following this line, applicable conditions for FRP-PCM method taking into account the combinations of different internal (e.g., strength of concrete) and external conditions (e.g., loosening pressure) were proposed, which could help select the most effective type of FRP-PCM reinforcement according to the actual conditions of tunnel linings concerned. Other unfavorable conditions beyond the loosening pressure will be considered in the future exploration of the performance of FRP-PCM reinforcement.

References:

Arduini M, Nanni A. Behavior of precracked RC beams strengthened with carbon FRP sheets. Journal of Composites for Construction, 1997, 1(2): 63-70.

Asakura T, Shiba Y, Matsuoka S, Oya T, Yashiro K. Damage to mountain tunnels by earthquake and its mechanism. Japan Society of Civil Engineers, 2000, 659: 27-38.

Asakura T, Kojima Y. Tunnel maintenance in Japan. Tunnelling and Underground Space Technology, 2003, 18(2): 161-169.

Berg A C, Bank L C, Oliva M G,Russel J S. Construction and cost analysis of an FRP reinforced concrete bridge deck. Construction and Building Materials, 2006, 20(8): 515-526.

Bournas D A, Pavese A, Tizani W. Tensile capacity of FRP anchors in connecting FRP and TRM sheets to concrete. Engineering Structures, 2015, 82: 72-81.

Buyukozturk O, Hearing B. Failure behavior of precracked concrete beams retrofitted with FRP. Journal of composites for construction, 1998, 2(3): 138-144.

Ceroni F. Experimental performances of RC beams strengthened with FRP materials. Construction and Building Materials, 2010, 24(9): 1547-1559.

Chajes M J, Thomson T A, Januszka T F, Finch W W. Flexural strengthening of concrete beams using externally bonded composite materials. Construction and Building Materials, 1994, 8(3): 191-201.

Chen J F, Teng J G. Shear capacity of FRP-strengthened RC beams: FRP debonding. Construction and Building Materials, 2003, 17(1): 27-41.

Chiaia B, Fantilli A P, Vallini P. Combining fiber-reinforced concrete with traditional reinforcement in tunnel linings. Engineering Structures, 2009, 31(7): 1600-1606.

Chryssanthakis P, Barton N, Lorig L, Christianson M. Numerical simulation of fiber reinforced shotcrete in a tunnel using the discrete element method. International Journal of Rock Mechanics and Mining Sciences, 1997, 34(3): 54. e1-54. e14.

Clarke J L, Waldron P. The reinforcement of concrete structures with advanced composites. Structural Engineer, 1996, 74(17).

De la Fuente A, Pujadas P, Blanco A, Aguado A. Experiences in Barcelona with the use of fibres in segmental linings. Tunnelling and Underground Space Technology, 2012, 27(1): 60-71.

Erki M A, Rizkalla S H. FRP reinforcement for concrete structures. CONCRETE INTERNATIONAL-DETROIT-, 1993, 15: 48-52.

Esfahani M R, Kianoush M R, Tajari A R. Flexural behaviour of reinforced concrete beams strengthened by CFRP sheets. Engineering structures, 2007, 29(10): 2428-2444.

East Nippon Expressway Company Limited., Central Nippon Expressway Company Limited., West Nippon Expressway Company Limited. Design code No. 3 Tunnel chapter on tunnel project safety (Neighboring construction), 2006. (in Japanese)

Franzén T. Shotcrete for underground support: a state-of-the-art report with focus on steel-fibre reinforcement. Tunnelling and Underground Space Technology, 1992, 7(4): 383-391.

Grace N F, Sayed G A, Soliman A K, Sakeh K R. Strengthening reinforced concrete beams using fiber reinforced polymer (FRP) laminates. ACI Structural Journal-American Concrete Institute, 1999, 96(5): 865-874.

Hensher D A. Fiber-reinforced-plastic (FRP) reinforcement for concrete structures: properties and applications. Elsevier, 2013.

Itasca Consulting Group, Inc. FLAC3D User's manual, 2002.

Jeng F, Lin M L, Yuan S C. Performance of toughness indices for steel fiber reinforced shotcrete. Tunnelling and underground space technology, 2002, 17(1): 69-82.

Jiang Y, Xiao J, Tanabashi Y, Mizokami T. Development of an automated servo-controlled direct shear apparatus applying a constant normal stiffness condition. International Journal of Rock Mechanics and Mining Sciences, 2004, 41(2): 275-286.

Jiang Y, Tanabashi Y, Li B, Esaki T. Influence of geometrical distribution of rock joints on deformational behavior of underground opening. Tunnelling and underground space technology, 2006, 21(5): 485-491.

Kiriyama K, Kakizaki M, Takabayashi T, Hirosawa N. Structure and construction examples of tunnel reinforcement method using thin steel panels. Nippon Steel Technical Report, 2005, 92: 45-50.

Kishi N, Zhang G, Mikami H. Numerical cracking and debonding analysis of RC beams reinforced with FRP sheet. Journal of Composites for Construction, 2005, 9(6): 507-514.

Kojima Y, Ohta T. Basic ideas on countermeasures of mountain tunnel deformation due to earth pressure. Journal of Japan Society of Engineering Geology. 2014, 54(6): 251-263.

Lau D, Pam H J. Experimental study of hybrid FRP reinforced concrete beams. Engineering Structures, 2010, 32(12): 3857-3865.

Lee J K, Lee J H. Nondestructive evaluation on damage of carbon fiber sheet reinforced concrete. Composite structures, 2002, 58(1): 139-147.

Li L J, Guo Y C, Liu F, Bungey J H. An experimental and numerical study of the effect of thickness and length of CFRP on performance of repaired reinforced concrete beams. Construction and Building Materials, 2006, 20(10): 901-909.

Li S P, Wu D X, Xie W H, Li Y S, Wu Z Y, Zhou G, Zhao H Y. Effect of confining

presurre, pore pressure and specimen dimension on permeability of Yinzhuang Sandstone. International Journal of Rock Mechanics and Mining Sciences, 1997, 34(3): 175. e1-175. e11.

Martinola G, Meda A, Plizzari G A, Rinaldi Z. Strengthening and repair of RC beams with fiber reinforced concrete. Cement and Concrete Composites, 2010, 32(9): 731-739.

Matsunaga T, Kumasaka H, Kojima Y, Asakura T. A study on prediction and reinforcement of tunnel deformation considering the time degradation of the rock mass strength. Japan Society of Civil Engineers, 2005, 799: 75-88.

Mazzotti C, Savoia M, Ferracuti B. An experimental study on delamination of FRP plates bonded to concrete. Construction and Building Materials, 2008, 22(7): 1409-1421.

Miyauchi K. Estimation of strengthening effects with carbon fiber sheet for concrete column. Proceedings of the 3rd International Symposium on Non-Metallic (FRP) Reinforcement for Concrete Structures. Japan Concrete Institute, 1997: 217-224.

Nystrom H E, Watkins S E, Nanni A, Murray S. Financial viability of fiber-reinforced polymer (FRP) bridges. Journal of Management in Engineering, 2003, 19(1): 2-8.

Pešić N, Pilakoutas K. Concrete beams with externally bonded flexural FRP-reinforcement: analytical investigation of debonding failure. Composites Part B: Engineering, 2003, 34(4): 327-338.

Rashid M A, Mansur M A. Reinforced high-strength concrete beams in flexure. ACI Structural Journal, 2005, 102(3): 462-471.

Research society of FRP grid construction method. Design and construction manuals of reinforcement for concrete structure by FRP grid thicken or lining method (plan), 2007. (in Japanese)

Sumarac D, Sekulovic M, Krajcinovic D. Fracture of reinforced concrete beams subjected to three point bending. International Journal of Damage Mechanics, 2003, 12(1): 31-44.

Täljsten B. Defining anchor lengths of steel and CFRP plates bonded to concrete. International Journal of Adhesion and Adhesives, 1997, 17(4): 319-327.

The Ministry of Public Works Research Institute Tunnel Laboratory. Document: Prediction and measures manuals of ground deformation for tunnel excavation (plan), 1994. (in Japanese)

Toutanji H, Zhao L, Zhang Y. Flexural behavior of reinforced concrete beams externally strengthened with CFRP sheets bonded with an inorganic matrix. Engineering Structures, 2006, 28(4): 557-566.

Uno Y, Kimura S. Characteristic evaluation of exfoliation risk variation model in case of road tunnel. Japan Society of Civil Engineers, F4 (Construction management),

2012, 68(2): 92-108.

Wang W W, Li G. Experimental study and analysis of RC beams strengthened with CFRP laminates under sustaining load. International journal of solids and structures, 2006, 43(6): 1372-1387.

Wu H. Application of orthogonal experimental design for the automatic software testing. Applied Mechanics and Materials. Trans Tech Publications, 2013, 347: 812-818.

Yao J, Teng J G, Chen J F. Experimental study on FRP-to-concrete bonded joints. Composites Part B: Engineering, 2005, 36(2): 99-113.

Ying, G. Research on the corona aging properties of silicone rubber material based on orthogonal test method. Thesis of North China Electric Power University, 2009.

Yu S, Chen Z, Wang Y, Duan Q, Jia Z. Analysis on the deep anti-sliding stability of concrete gravity dam foundation by FLAC strength reduction method. Hydrogeology & Engineering Geology, 2009, 3: 016.

Zhang H, Wu X G, Zeng W H. Study on tunneling experiment and mathematical model of EPB shield. Chinese Journal of Rock Mechanics and Engineering, 2005, 24(A02): 5762-5766.

Zhu B F. Finite element whole course simulation and sequential strength reduction method for safety appraisal of concrete dam. Water Resources and Hydropower Engineering, 2007, 1: 1-6.

CHAPTER 6

Study on Reinforcing Effects of FRP-PCM Method under Seismic Load

6.1 Introduction

Fast population growth in urban areas has resulted in a significant shortage of aboveground spaces and led to increase underground structures. Different types and underground spaces and structures including underground utility tunnels, subway tunnels, subway stations, subway shelters, culverts, etc. may exist in any large city.

Although the seismic behavior of underground structures, such as tunnels, is assumed to be better than that of surface structures, some existing tunnels were severely damaged by earthquakes in recent years (Suzuki 1996; Yoshida 1999; O'Rourke et al. 2001; Wang 2001 and Kontogianni et al. 2003). Cracking, spalling and water leakage occurring during earthquakes would significantly affect the safety of tunnel operation. Repairing and reinforcing the existing concrete underground structures have become a major part of civil engineering activities.

A series of methods have been adopted to effectively improve the integrity of concrete structures in existing tunnels, typical ones of which are grouting reinforcement method, fiber reinforced shotcrete (FRS) method (De la Fuente et al. 2012; Chiaia et al. 2009; Jeng et al. 2002 and Franzén 1992), carbon fiber sheet (CFS) method (Lee et al. 2002 and Miyauchi 1997), steel board method (Kiriyama et al. 2005) and fiber reinforcement plastic (FRP) method (Erki et al. 1993; Hensher 2013 and Asakura et al. 2003).

Due to the favorable properties such as high strength, low weight, easy handling and application, immunity to corrosion and etc., FRP as a strengthening material for the reinforcement concrete (RC) structures has become commonly used in engineering fields. In recent years, extensive researches have been carried out to investigate the reinforcing effects of FRP grids under seismic load. Sheikh et al. (2002) conducted an experimental program in which 12 column specimens were tested under constant axial load and cyclic lateral load that were used to simulate the earthquake loads, and found that the strength, ductility and energy absorption capacity of columns can be improved by utilizing FRP. Zou et al. (2007) proposed an optimization technique for the performance-based seismic FRP retrofit design of RC building frames, and the effectiveness of this proposed procedure was discussed and certified by a numerical

example. Antoniades et al. (2003) conducted cyclic tests on seismically damaged reinforced concrete walls strengthened with FRP reinforcement, and the test results showed that the strength of specimen reinforced by FRP strips increases up to approximately 30% with respect to a conventional repair method. Lam et al. (2006) experimentally studied the behaviors of FRP-confined concrete under cyclic compression test, and a number of significant conclusions were drawn, including the existence of an envelope curve and the cumulative effect of loading cycles. Zhu et al. (2006) conducted a series of constant axial load and pseudo static lateral load test on the concrete-filled fiber reinforced polymer tubes (CFFT) to investigate the seismic performance of CFFT for bridge substructure, and found that the CFFT columns exhibited significant improvement over traditional RC columns in both ultimate strength and ductility. Balsamo et al. (2005) assessed the seismic repair effects of FRP composites on reinforced concrete structures with a full-scale dual system that subjected to pseudodynamic tests in the ELSA laboratory, and compared the original structure with the repaired structure in terms of global and local performance. Mamalis et al. (2006) adopted the LS-DYNA3D explicit finite element code to investigate the compressive properties and crushing response of square carbon FRP tubes with static axial compression and impact testing, and found that the collapse modes ranged from mid-length unstable collapse model-which was the predominant collapse mode, to local tube-wall buckling and stable progressive end crushing with tube wall splaying which was the model of collapse featured by the higher crash energy absorption.

Despite a large amount of researches on the behavior of RC structures reinforcing with FRP were put forward, few researches were conducted on the reinforcing effects of FRP-PCM method on tunnel lining under seismic load. In the present study, the seismic resistance of tunnel lining reinforcing with FRP-PCM method was estimated numerically. First, the mechanical behaviors of interface between PCM and concrete specimens were determined based on the test in Chapter 5. Then, numerical simulations based on finite difference method (FDM) were performed to quantitatively analyze the reinforcing effects of FRP-PCM method on tunnel linings under seismic load, taking into accounts the influences of cavity position and construction method, and those analytic results could provide valuable guidance for the reinforcing of underground structures.

6.2 Objective earthquake

6.2.1 Introduction of Chuetsu earthquake

The Chuetsu earthquakes occurred in Niigata Prefecture, Japan, at 17:56 local time

(08:56 UTC) on Saturday, October 23, 2004. The Japan Meteorological Agency (JMA) named it the "Heisei 16 Niigata Prefecture Chuetsu Earthquake". Niigata Prefecture is located in the Hokuriku region of Honshu, the largest island of Japan. The initial earthquake had a magnitude of 6.6 and caused noticeable shaking across almost half of Honshu, including parts of the Tōhoku, Hokuriku, Chūbu, and Kantō regions.

This severe earthquake with a magnitude of 6.8 and a maximum tremor intensity level of 7 according to the Japanese 7-stage seismic scale occurred in and around the Chuetsu Area, Niigata Prefecture. Approximately 100000 people took refuge (49 killed, 4794 injured), approximately 120000 houses were damaged (including 3185 completely destroyed), and the damage amounted to > ¥ 3 trillion (as of 16 September 2005). Because of the sustained occurrence of aftershocks and delayed reconstruction of community lifelines, 9160 people who lost their houses were still living in temporary shelter as long as 1 year after the earthquake (Toyabe et al., 2006, Hikima et al., 2005; Yashiro et al., 2007; Wang et al., 2007 and Chigira et al., 2006). Figs 6.1-6.2 show the shindo intensity and maximum acceleration distributions of Chuetsu earthquake that obtained from Japan Meteorological Agency (JMA).

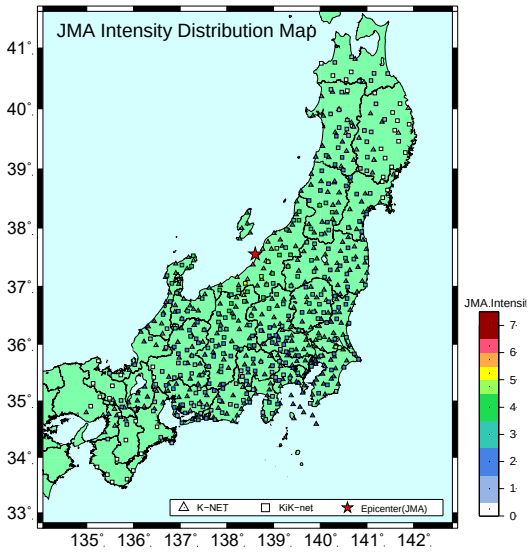

Fig. 6.1 Magnitudes distribution.

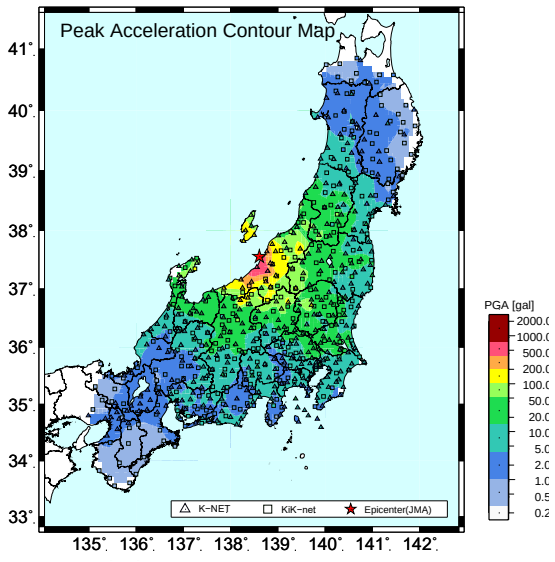

Fig. 6.2 Peak accelerations distribution.

6.2.2 Observation of ground motion (N/G019 Ojiya city)

The observation of the aftershocks was conducted in Ojiya city, the Niigata prefecture, central Japan as shown in Fig. 6.3. In the present study, one of the aftershocks that observed by the National Research Institute for Earth Science and Disaster Resilience, strong-motion seismograph networks (K-Net), at July 16, 2007, were adopted during the numerical simulation.

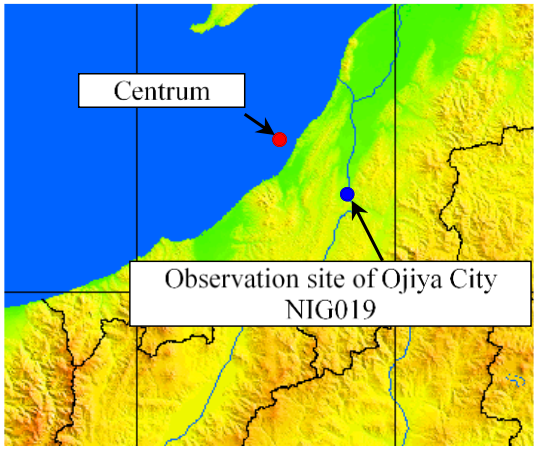

Fig. 6.3 Positions of the observation point and the centrum.

Since the three component accelerometers were selected during the observation of ground motion, the observed accelerations were divided into three components: *NS*, *EW*, *UD* components. Herein, *NS*, *EW*, *UD* refer to the ground motion in north and south direction, east and west direction, up and down direction, respectively. The observed ground accelerations in these three directions that expressed by the waveform processing software WAVEANA3.0 are shown in Fig. 6.4. The peak accelerations in *NS*, *EW* and *UD* directions are 390.5 gal (cm/s), 454.7 gal (cm/s) and 116.5 gal (cm/s), respectively.

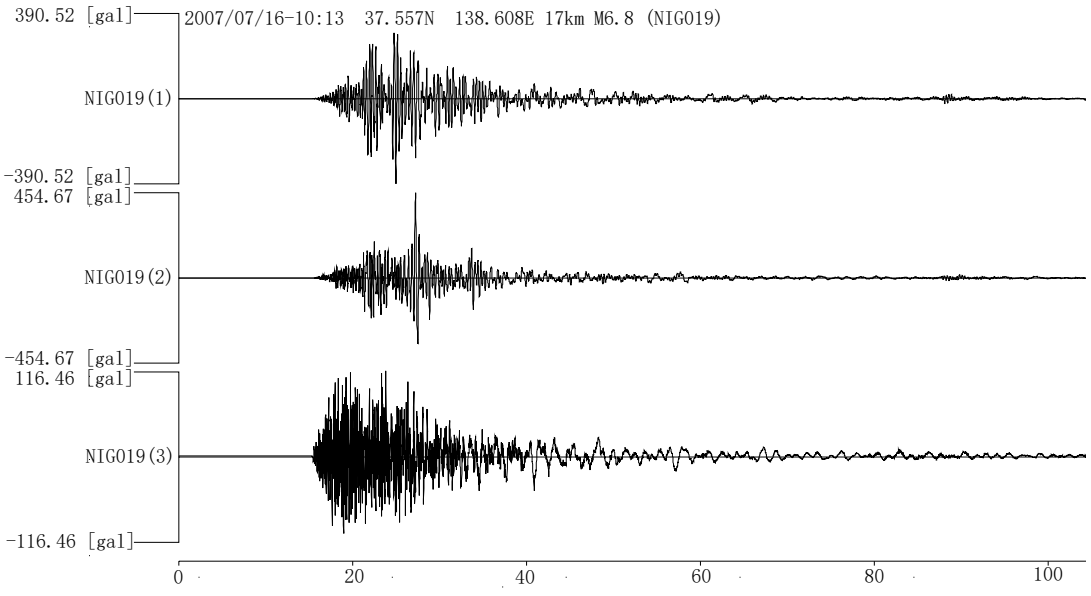

Fig. 6.4 Acceleration waves measured at the Ojiya observation site during the Niigata earthquake (data from K-NET, the National Research Institute for Earth Science and Disaster Prevention of Japan).

6.2.3 Investigation of seismic wave at the deep rock formation

The seismic records obtained from observation sites during an earthquake represent the seismic motions of the ground surface. When earthquake occurs, seismic waves propagate from the deep rock formation to the ground surface. To reproduce such a process in numerical simulations, it is necessary to investigate the seismic motion at the deep rock formation, which can be input onto the bottom boundary of the foundation model. In this study, the code of k-SHAKE developed by the Structure and Planning Institute of Japan (2005a) on the basis of the theory of repeated seismic reflection was utilized to investigate the seismic wave at the deep rock formation with a certain depth. The theory of repeated seismic reflection, the model of back-calculation, and the calculation results are present as follows:

(1) Theory of repeated seismic reflection

The theory of repeated seismic reflection assumes that rock (or soil) layers distribute horizontally in an infinite half space, which are constituted by homogenous and isotropic geomaterials, as shown in Fig. 6.5. The origins of local coordinates are located at the upper surface of each layer, with the positive direction of the x-axis going downward perpendicularly. During the upward propagation of simple harmonic waves, the horizontal displacement of rock particles $u(x, t)$ induced by the shear wave, which

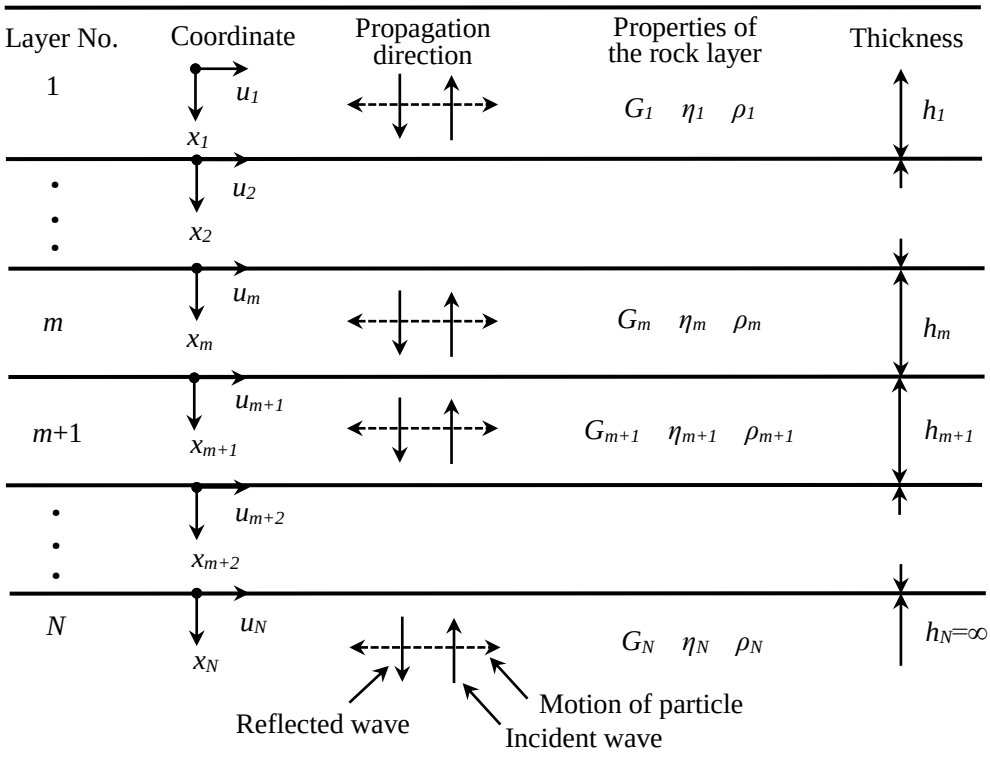

Fig. 6.5 Theory of repeated seismic reflection for investigating the seismic motions at the deep rock formation (after Structure and Planning Institute of Japan, 2005a)**.**

depends on the coordinate x and the time t, should satisfy the one-dimensional equation of motion, as expressed by

$$\rho \frac{\partial^2 u(x,t)}{\partial t^2} = G \frac{\partial^2 u(x,t)}{\partial x^2} + \eta \frac{\partial^3 u(x,t)}{\partial x^2 \partial t} \tag{6.1}$$

where ρ is the density of rock; G is the shear modulus of rock and η is the viscosity coefficient. The general solution of the equation of motion can be written as

$$u(x,t) = Ee^{i(kx+\omega t)} + Fe^{-i(kx-\omega t)} \tag{6.2}$$

where k is the wave number; ω is the angular frequency; E is the amplitude of incident wave which propagates upwards; F is the amplitude of reflected wave that propagates downwards; and i is the imaginary unit.

The velocity $v(x, t)$ and the acceleration $a(x, t)$ of particles can be obtained by calculating the first-order and second-order partial derivatives of the displacement with respect to time, as given by Eq. (6.3). Additionally, the shear stress $\tau(x, t)$ and the shear strain $r(x, t)$ can also be derived based on the elastic theory, in the form of Eq. (6.4).

$$v(x,t) = \dot{u}(x,t) = \frac{\partial u}{\partial t}, \quad a(x,t) = \ddot{u}(x,t) = \frac{\partial^2 u}{\partial t^2} \tag{6.3}$$

$$\tau(x,t) = G \frac{\partial u}{\partial x} + \eta \frac{\partial^2 u}{\partial x \partial t}, \quad r(x,t) = \frac{\partial u}{\partial x} \tag{6.4}$$

For any layer (e.g., the mth layer), the displacements and the shear stresses at the upper and lower boundaries ($x = 0$ and $x = h_m$) of the layer can be expressed as

$$u_m(x=0) = (E_m + F_m)e^{i\omega t}, \quad u_m(x=h_m) = \left(E_m e^{ik_m h_m} + F_m e^{-ik_m h_m}\right)e^{i\omega t} \tag{6.5}$$

$$\tau_m(x=0) = ik_m G_m^* (E_m - F_m)e^{i\omega t}, \quad \tau_m(x=h_m) = ik_m G_m^* \left(E_m e^{ik_m h_m} + F_m e^{-ik_m h_m}\right)e^{i\omega t} \tag{6.6}$$

where $G_m{}^*$ is the complex shear modulus ($G_m{}^* = G_m + i\omega\eta_m$). The compatibility conditions of displacement and stress on interfaces between adjacent layers need to be satisfied. For example, at the interface between the mth and $(m+1)$th layers, the boundary conditions can be given as: $u_m(x=h_m) = u_{m+1}(x=0)$, $\tau_m(x=h_m) = \tau_{m+1}(x=0)$. Then the relation of wave amplitudes between two adjacent layers can be given by

$$\begin{bmatrix} E_{m+1} \\ F_{m+1} \end{bmatrix} = \frac{1}{2} \begin{bmatrix} (1+\alpha_m)e^{ik_m h_m} & (1-\alpha_m)e^{-ik_m h_m} \\ (1-\alpha_m)e^{ik_m h_m} & (1+\alpha_m)e^{-ik_m h_m} \end{bmatrix} \begin{bmatrix} E_m \\ F_m \end{bmatrix} \tag{6.7}$$

where α_m represents the impedance of the mth layer, with the complex form of

$$\alpha_m = \frac{k_m G_m^*}{k_{m+1} G_{m+1}^*} = \left(\frac{\rho_m G_m^*}{\rho_{m+1} G_{m+1}^*} \right)^{1/2} \tag{6.8}$$

As shown in Fig. 6.6, the seismic amplitudes at any layer can be derived from those of the adjacent layers. Therefore, if the wave amplitudes at the ground surface is known ($E_1 = F_1$, due to the fact that the shear stress on the ground surface is zero), the amplitudes in all layers can be derived, and the displacement function can be solved.

It should be noted that the expressions mentioned above are derived with the assumption of harmonic waves. When considering the real seismic waves, the situation will become much more complicated. In this case, the real seismic waves need to be firstly translated into the superposition form of multiple harmonic waves by performing the Fourier transform. Seismic waves after the Fourier transform are in the frequency-domain form, which can be translated back into the time-domain form through the inverse Fourier transform. The seismic motions at every layers caused by the real seismic waves can be obtained by superposing all the motions caused by the componential harmonic waves.

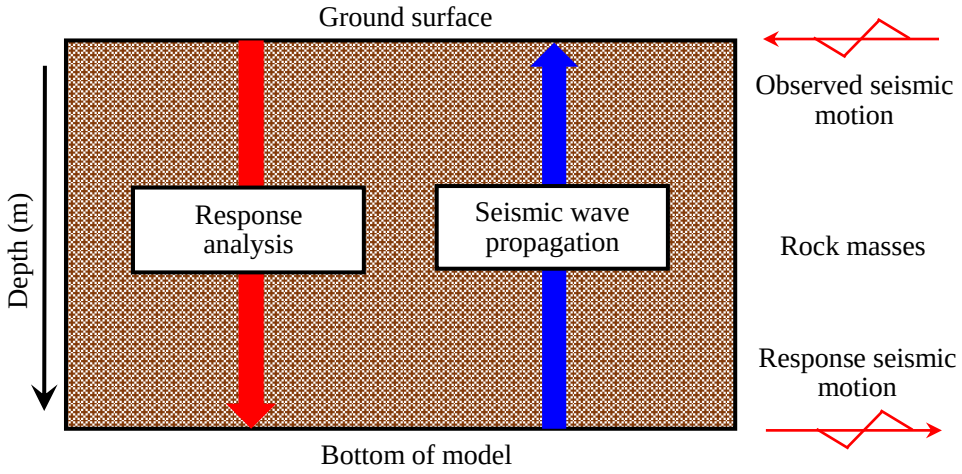

Fig. 6.6 Numerical model for investigating the seismic wave at the bottom of model.

(2) Simulation of seismic wave at the deep rock formation

The code of *k*-SHAKE was utilized to investigate the seismic motion at the deep rock formation under the nuclear power plant, with the numerical model shown in Fig. 6.6. The lateral boundaries of model were assumed to be semi-infinite rock regions. For geomaterials, the damping ratio generally falls into the range from 2% to 5% (Biggs, 1964). In this study, the damping ratio of the rock mass was set as 3%.

6.3 Numerical simulation with FRP-PCM method under seismic load

Although the seismic behavior of mountain tunnels is assumed to be better that of surface structures, cracking and spalling may be induced to some tunnels when encountered with earthquakes. In this section, numerical simulations on tunnels that reinforced with FRP-PCM method was performed to analyze the impacts of tunnel shapes and cavity positions on the reinforcing effects.

6.3.1 Numerical models

The numerical models of tunnels, which were constructed by the Fore-piling Method (FM) and the New Austrian Tunneling Method (NATM), were established based on FDM, as shown in Fig. 6.7. The tunnels constructed by FM are shown in Figs. 6.7(a)-(c), while the one by NATM is shown in Fig. 6.5(d). Mountain tunnels constructed by FM typically encounter an unfavorable condition that cavities exist between lining and surrounding rock masses. In order to investigate the impacts of cavity positions on the reinforcing effects of FPR-PCM method, a cavity was presumed to exist on the crown (see Fig. 6.7(a)) or at the right shoulder (see Fig. 6.7(b)) of the numerical models with an arc angle of 60° and a thickness of 30 cm. In Figs. 6.7(a)-(b), the thickness of lining was typically 45 cm, which was reduced to 15 cm at the central position of the cavity. The thickness of shotcrete and secondary lining was selected as 15 cm and 30 cm as in Fig. 6.7(d), respectively. The reinforcement region with FRP-PCM method for all the four cases covered an arc length of 180° on the upper wall of tunnel as shown in Fig. 6.8, and the back-filling was conducted to the tunnels with cavities. The tunnel lining and cavities were reproduced by the finite element mesh, while the reinforcement effects of FRP-PCM method were investigated by the liner element (Itasca 2002). The horizontal distance from the wall of tunnel to the boundary of model was determined as 2D (D is the excavation diameter of the tunnel that is equal to 10 m), since it has been confirmed that its simulation result is almost identical to a larger model with such horizontal distance of 5D. Reducing the distance from 5D to 2D could remarkably reduce the computational time.

6.3.2 Boundary conditions

In the static analysis stage, the left and right sides were roller boundaries, and the bottom boundary was fixed with no rotation and displacement. In the seismic analysis stage, the free-field boundary as shown in Fig. 6.9 was selected. A shear wave was applied on the bottom boundary as shown in Fig. 6.9, and the lateral boundaries in the vertical directions were fixed. The lateral boundaries of the main grid are coupled to

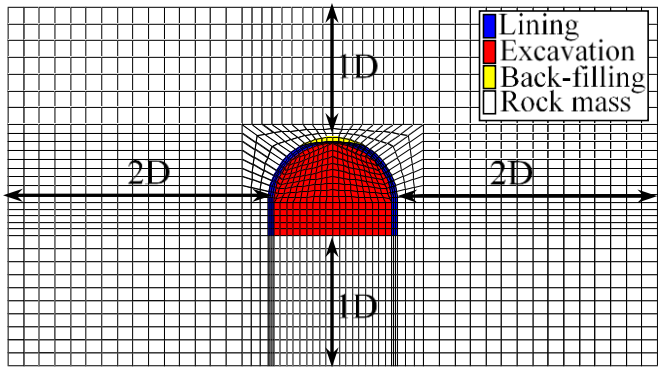

(a) FM (Cavity: crown)

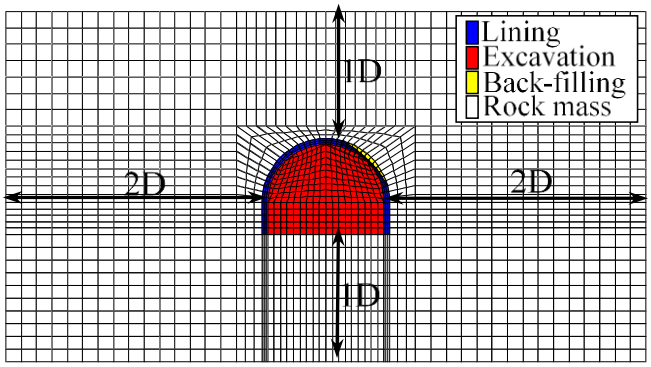

(b) FM (Cavity: shoulder)

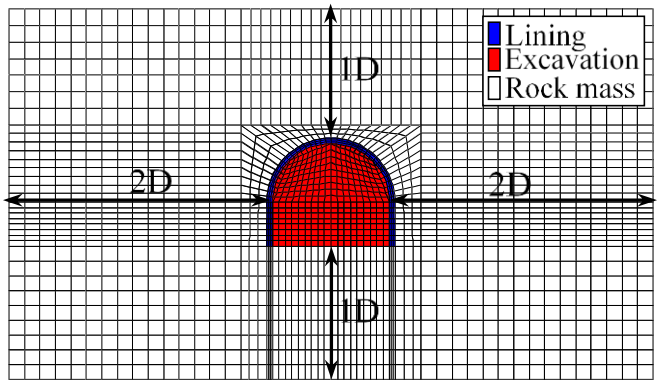

(c) FM (No cavity)

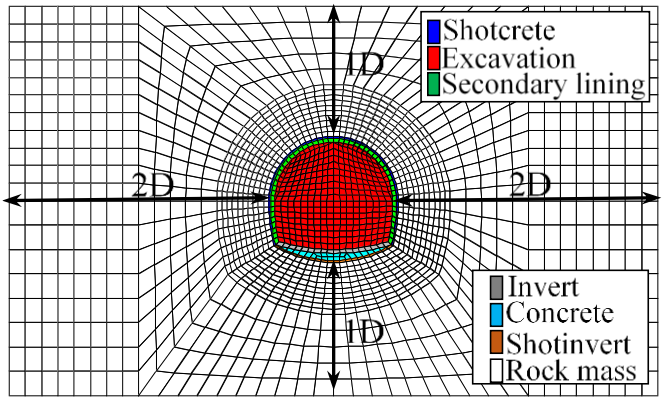

(d) NATM

Fig. 6.7 Numerical models.

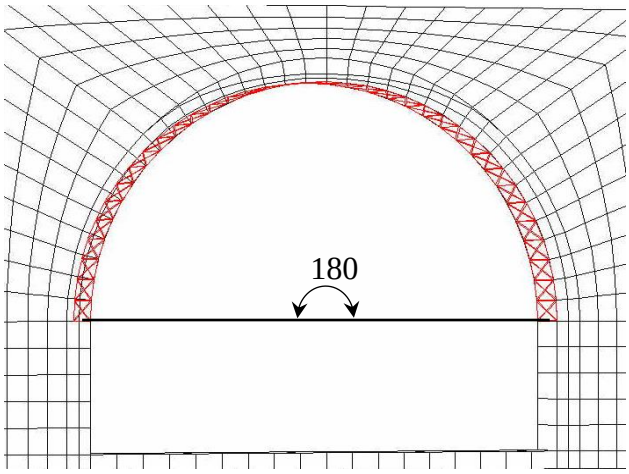

Fig. 6.8 Reinforced region with FRP-PCM method.

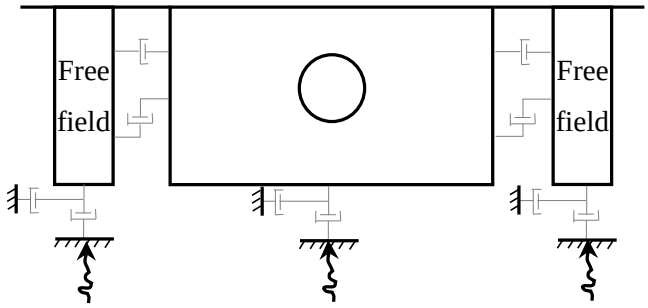

Fig. 6.9 Free-filed boundary for seismic analysis.

the free-field grid by viscous dashpots to simulate a quiet boundary (see Fig. 6.9), and the unbalanced forces from the free-field grid are applied to the main-grid boundary. Both conditions are expressed in Eqs. (6.9), (6.10) and (6.11), which apply to the free-field boundary along one side boundary plane with its normal in the direction of the *x*-axis. Similar expressions may be written for the other sides and corner boundaries.

$$F_x = -\rho C_p (v_x^m - v_x^{ff}) A + F_x^{ff} \tag{6.9}$$

$$F_y = -\rho C_s (v_y^m - v_y^{ff}) A + F_y^{ff} \tag{6.10}$$

$$F_z = -\rho C_s (v_z^m - v_z^{ff}) A + F_z^{ff} \tag{6.11}$$

where, ρ = density of material along vertical model boundary;

C_p = *p*-wave speed at the side boundary;

C_s = *s*-wave speed at the side boundary;

A = area of influence of free-field gridpoint;

v_x^m = *x*-velocity of gridpoint in main grid at side boundary;

v_y^m = *y*-velocity of gridpoint in main grid at side boundary;

v_z^m = z-velocity of gridpoint in main grid at side boundary;

F_x^{ff} = free-field gridpoint force with contributions from the σ_{xx}^{ff} stresses of the free-field zones around the gridpoint;

F_y^{ff} = free-field gridpoint force with contributions from the σ_{xy}^{ff} stresses of the free-field zones around the gridpoint;

F_z^{ff} = free-field gridpoint force with contributions from the σ_{xz}^{ff} stresses of the free-field zones around the gridpoint;

In this way, plane waves propagating upward suffer no distortion at the boundary because the freefield grid supplies conditions that are identical to those in an infinite model.

6.3.3 Mechanical properties

Two classes of ground (CI and CII) were selected as the host rock masses in the numerical simulations, which are typical ground encountered in tunnel constructions in Japan (The Ministry of Public Works Research Institute Tunnel Laboratory 1994). Since the quick hardening properties and high strength, the urethane materials were selected as the back-filling materials, and the mechanical properties of ground, lining and back-filling materials are shown in Table 6.1. The mechanical properties of interface between PCM and concrete sandwiching an FRP grid were determined in Chapter 5 as tabulated in Table 6.2. The numerical analysis cases are summarized in 6.3.

Table 6.1 Properties of ground, lining and back-filling material.

Property	Ground class		Lining	Back-filling material
	CI	CII		
γ (kN/m3)	23.5	22.6	24.0	9.8
E (MPa)	1960	980	24500	12.0
v	0.3	0.30	0.20	0.13
c (MPa)	1.96	0.98	6.99	0.50
φ (deg)	45	40.0	40.0	10.0
σ_t (MPa)	0.39	0.42	3.0	0.20

Table 6.2 Mechanical properties of reinforcement materials

	Young's modulus E (MPa)	Tensile strength σ_t (MPa)	Cohesion c (MPa)	Internal frictional angle φ (°)	Shear stiffness k_s (MPa/m)
CR8	100000	1400	2.22	17.7	7.37×10^3
PCM	26000	4.6			----

Table 6.3 Analysis cases.

Simulation case	Construction method	FRP grid	Ground class	Cavity
1	FM	----	CI	Crown
2	FM	----	CI	Shoulder
3	FM	----	CI	----
4	FM	----	CII	Crown
5	FM	----	CII	Shoulder
6	FM	----	CII	----
7	FM	CR8	CI	Crown
8	FM	CR8	CI	Shoulder
9	FM	CR8	CI	----
10	FM	CR8	CII	Crown
11	FM	CR8	CII	Shoulder
12	FM	CR8	CII	----
13	NATM	----	CI	----
14	NATM	----	CII	----
15	NATM	CR8	CI	----
16	NATM	CR8	CII	----

6.3.4 Input motion

The input motion was recorded at the observation site of Ojiya City during the Chuetsu-Oki earthquake occurred on July 16, 2007 in Niigata Province, Japan. The history of acceleration applied at the bottom boundary of the numerical model was obtained based on the one-dimensional response analysis as shown in Fig. 6.10. The maximum acceleration was observed at about 27.8 s, with a value about 330 Gal. Since the stability of underground tunnel is mainly controlled by the maximum acceleration during the earth-quake, in order to reduce the computational time, the input motion at the interval from 20.8 s to 30.8 s was extracted and utilized in the numerical analysis.

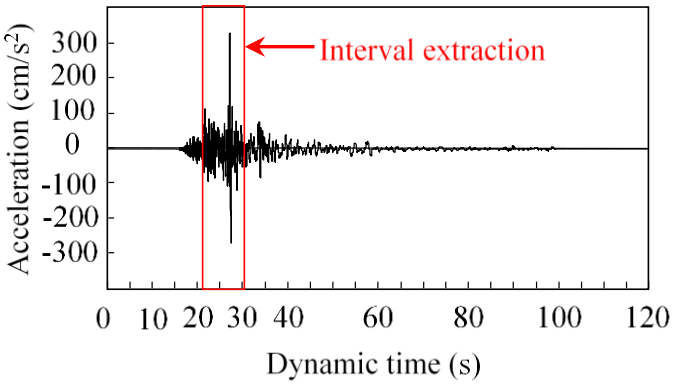

Fig. 6.10 Input motion during seismic analysis.

6.4 Results and discussions

6.4.1 Comparison of accelerations in various depth

The acceleration time histories obtained from the numerical models in various depth can be selected to verify the accuracy of calculation results. Herein, the results of tunnel constructed by NATM were selected as an example to show the variation of acceleration with the depth. The observation points are shown in Fig. 6.11, and the comparisons among the input acceleration histories and observed ones during the simulation are depicted in Fig. 6.12. Corresponding to the earthquake signal, a mall time window was plotted as representative of the maximum value of acceleration histories. As the depth of observation point increased, the maximum response of the acceleration decreased, and the maximum value of acceleration occurred with respect to the input motion.

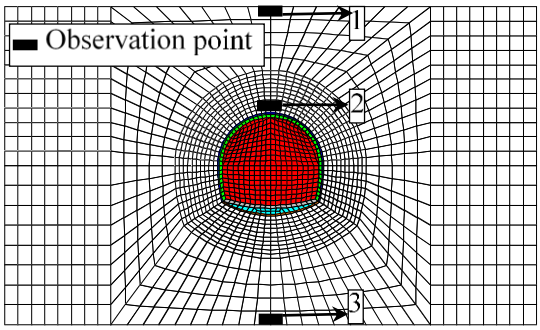

Fig. 6.11 Positions of the observation points and the centrum

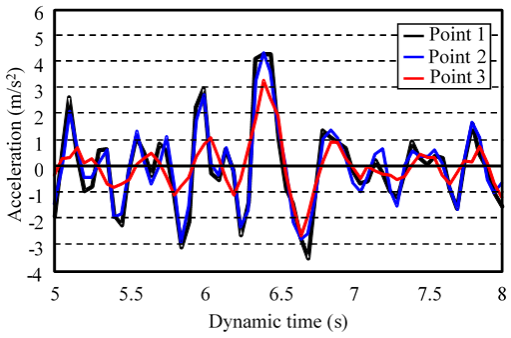

Fig. 6.12 Observed acceleration histories

6.4.2 Reinforcing effects of lining deformation

Figs. 6.13-14 show the simulation results of lining deformation for the ground class type of CI and CII in the cases of unreinforced and reinforced with the CR8 grids, respectively. The lining concrete in rock class type of CI shows almost no damage during the seismic analysis (see Fig. 6.13). However, for tunnels constructed with FM in rock

class type of CII as shown in Figs. 6.14(a), (c) and (e), the plastic failure occurred at the shoulder of tunnels, regardless the position of cavities. However, the tunnel with a cavity on the right shoulder exhibited an extremely larger failure regions. Since the existence of cavity, the cross section of tunnel lining was decreased, which resulted in the stress concentration at the location of cavity. All these failure regions almost occurred at the inner side of tunnel linings.

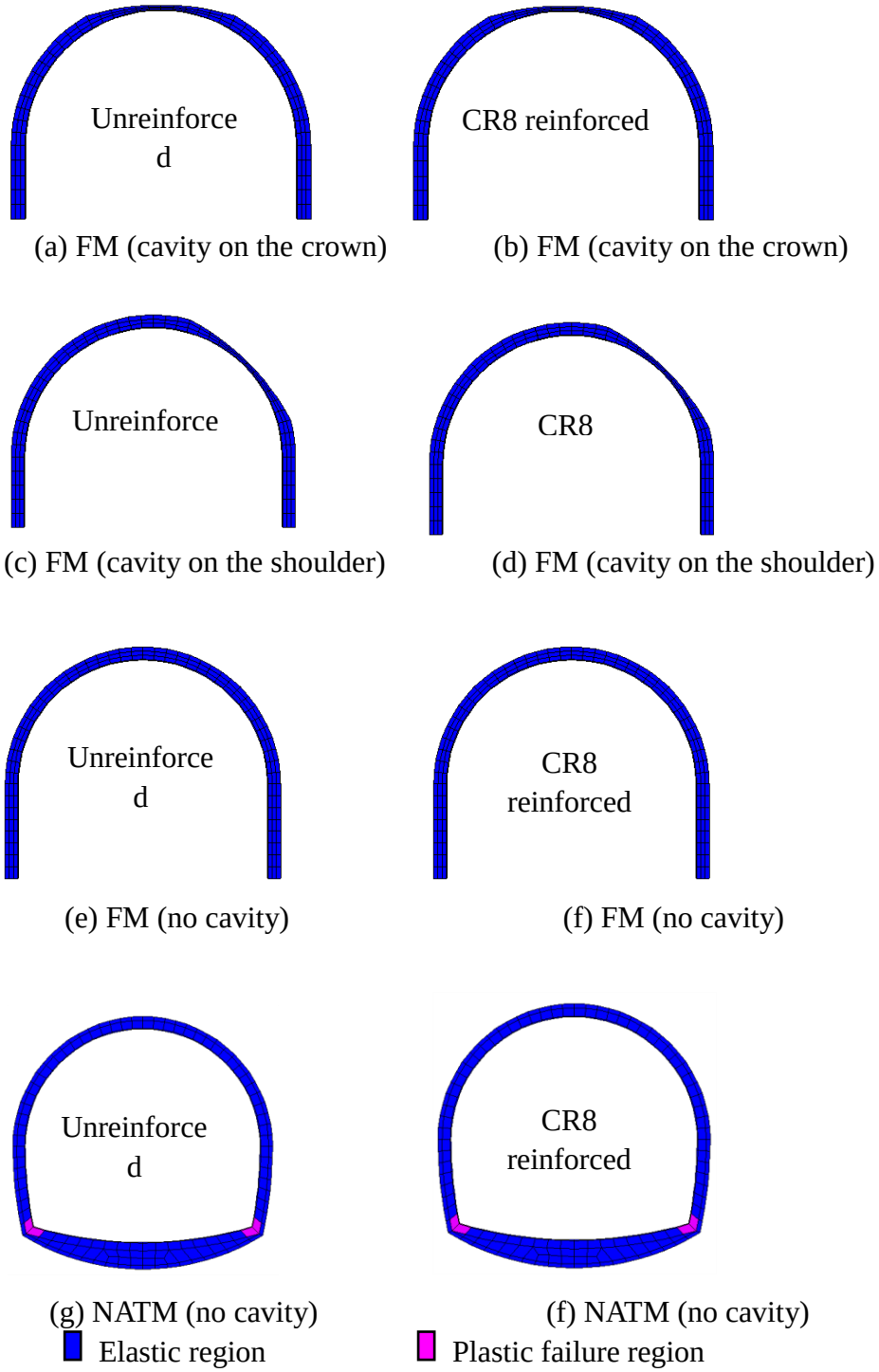

Fig. 6.13 Lining deformation for ground class of CI.

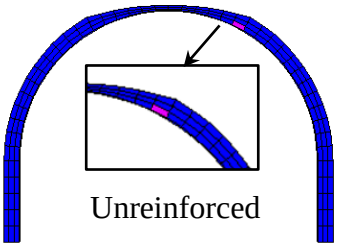

(a) FM (cavity on the crown)

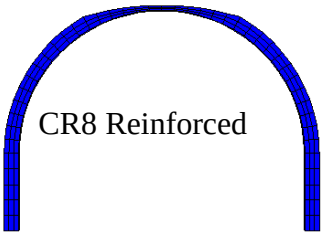

(b) FM (cavity on the crown)

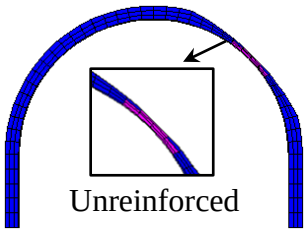

(c) FM (cavity on the shoulder)

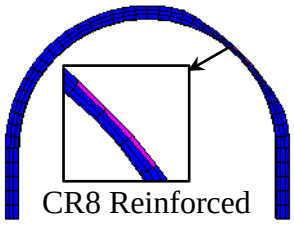

(d) FM (cavity on the shoulder)

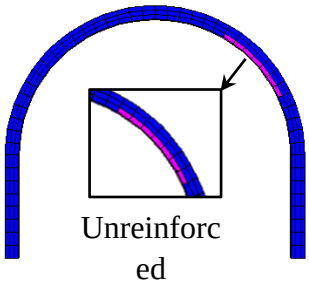

(e) FM (no cavity)

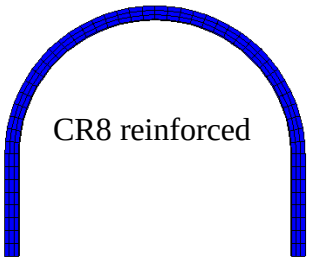

(f) FM (no cavity)

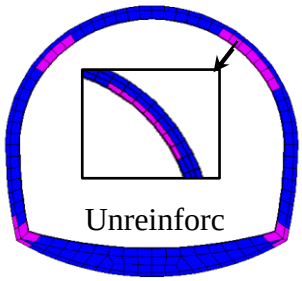

(g) NATM (no cavity)

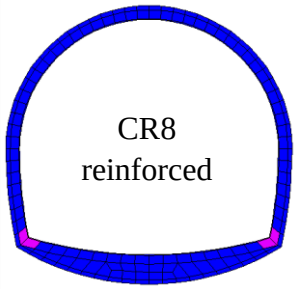

(f) NATM (no cavity)

Elastic region Plastic failure region

Fig. 6.14 Lining deformation for ground class of CII.

The reinforcement effects with CR8 grids are plotted on the right column of Fig. 6.14. For tunnels constructed in FM, plastic failure only occurred in the case with the cavity on the right shoulder of lining as shown in Fig. 6.14(d). Due to the reinforcement with FRP grids, the flexural stiffness at the inner side of the lining increased, which led to the failure occurring on the outside of lining concrete. For the one in NATM, failure region decreased dramatically, revealing that a good reinforcing effect was obtained with CR8 grids.

6.4.3 Axial stress distribution on lining concrete

Since almost no plastic failure region on lining concrete was occurred for tunnels in rock class type of CI, only axial force distribution on tunnel lining in the ground type of CII was discussed in this section. Figs. 6.15-6.16 depict the axial stress distribution on lining concrete in the cases of unreinforced and reinforced with CR8 grids for the ground classes of CII. In these figures, the positive denotes the compression stress, while the negative denotes the tensile stress. A great compression stress occurred at the inner side of lining concrete, regardless the position and existence of cavities, tunnel shapes. Tunnel with cavity on the right shoulder showed a larger compression stress comparing with the other twos constructed in FM. Compared with FM, the lining concrete in NATM showed a great bending capacity, which was generally improved by the closure of invert.

In order to estimate the reinforcing effect of FRP-PCM method quantitatively, an axial force reduction rate R_σ was defined as

$$R_\sigma = \frac{\sigma_{\mathrm{nr}} - \sigma_r}{\sigma_{nr}} \times 100\% \tag{6.12}$$

where, σ_{nr} is the axial stress acting on the unreinforced lining (MPa), and σ_r is the axial stress obtained in the reinforced cases (MPa). The axial stress is the principal stress oriented parallel to the wall of the tunnel lining, and the axial force reduction rate represents the degree the axial force is reduced by reinforcement.

Fig. 6.17 shows the axial stress with various ground class types and position of cavities. The axial force reduction rates for the cases of cavities on the crown and shoulder of tunnel linings with ground class of CII are 27% and 52%, respectively, revealing that the performance of reinforcement was greater with a cavity on the shoulder.

Fig. 6.18 shows the axial stress with various ground class types and construction methods. The axial force reduction rates for the cases constructed by the FM and NATM are 31% and 49%, respectively, indicating that a greater reinforcement effects could be obtained for tunnels in NATM.

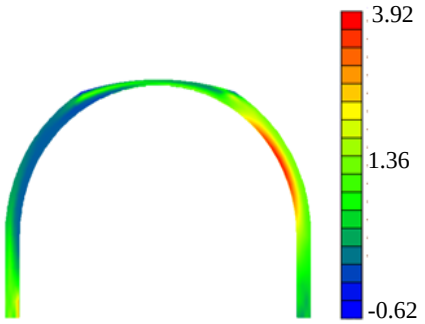

(a) FM (cavity on the crown)

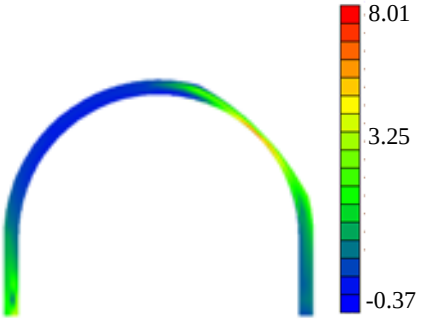

(b) FM (cavity on the shoulder)

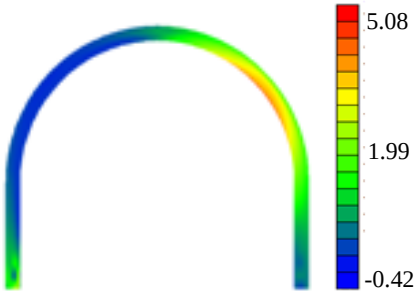

(c) FM (no cavity)

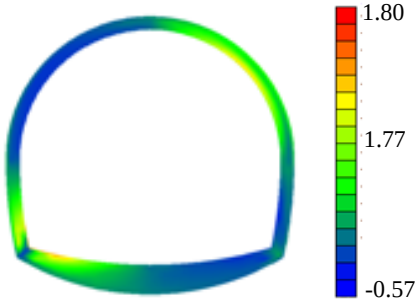

(d) NATM (no cavity)

Fig. 6.15 Axial sterss distribution on lining concrete for unreinforced cases (unit: MPa).

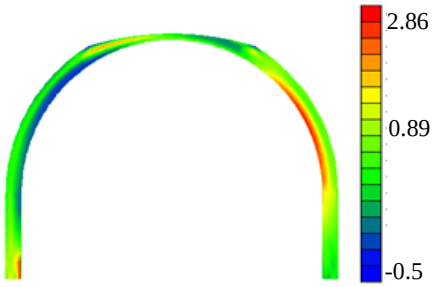

(a) FM (cavity on the crown)

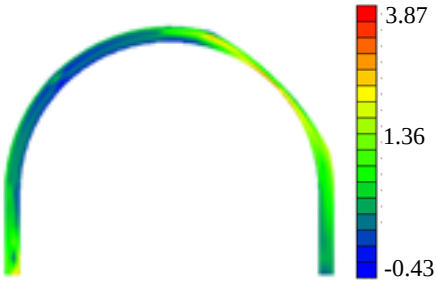

(b) FM (cavity on the shoulder)

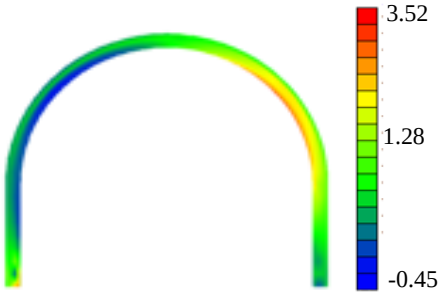

(c) FM (no cavity)

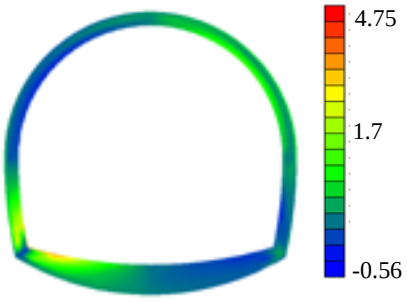

(d) NATM (no cavity)

Fig. 6.16 Axial stress distribution on lining concrete reinforced with CR8 grids (unit: MPa).

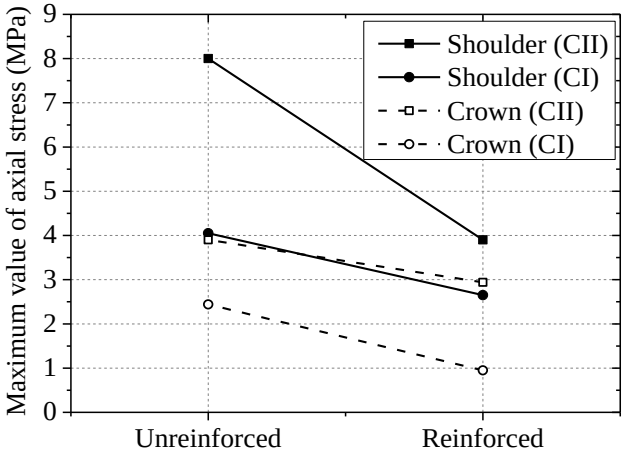

Fig. 6.17 Axial stress with various ground class types and position of cavities.

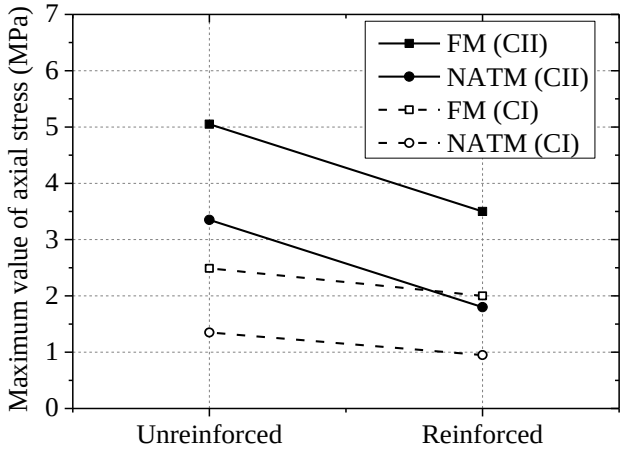

Fig. 6.18 Axial stress with various ground class types and construction methods.

6.5 Conclusions

In this section, numerical simulations under seismic load based on the FDM method were performed, taking into accounts the cavity positions (cavity on the crown and shoulder), the construction methods (FM and NATM) and types of ground class (CI and CII). Based on the numerical analysis, the following conclusions are drawn:

(1) The lining concrete in rock class type of CI showed no damage during the seismic analysis. For tunnels in rock class type of CII, the plastic failure zones almost occurred on the shoulder of tunnel linings, especially for tunnels constructed by FM.

(2) A good reinforcement performance was observed for the cases reinforced with CR8 grids. For the case with cavity on the shoulder of tunnel, the failure zones in the inner surface of lining were greatly improved. Better reinforcing effects were obtained in the case of cavity on the shoulder of tunnel, comparing with the one on the crown.

(3) The axial stress on tunnels that constructed by FM was greater than those by NATM, and the axial stress acting on tunnel linings was greatly decreased with FRP-PCM method. Although tunnels constructed in NATM showed a better bearing capacity comparing with the one in FM, a greater reinforcing effect was obtained for tunnels in NATM.

References:

Antoniades K K, Salonikios T N, Kappos A J. Cyclic tests on seismically damaged reinforced concrete walls strengthened using fiber-reinforced polymer reinforcement. Structural Journal, 2003, 100(4): 510-518.

Asakura T, Kojima Y. Tunnel maintenance in Japan. Tunnelling and Underground Space Technology, 2003, 18(2): 161-169.

Balsamo A, Colombo A, Manfredi G, Negro P, Prota A. Seismic behavior of a full-scale RC frame repaired using CFRP laminates. Engineering Structures, 2005, 27(5): 769-780.

Biggs J.M. Introduction to structural dynamics. McGraw-Hill Companies, New York, USA, 1964.

Chiaia B, Fantilli A P, Vallini P. Combining fiber-reinforced concrete with traditional reinforcement in tunnel linings. Engineering Structures, 2009, 31(7): 1600-1606.

Chigira M, Yagi H. Geological and geomorphological characteristics of landslides triggered by the 2004 Mid Niigta prefecture earthquake in Japan. Engineering Geology, 2006, 82(4): 202-221.

De la Fuente A, Pujadas P, Blanco A, Aguado A. Experiences in Barcelona with the use of fibres in segmental linings. Tunnelling and Underground Space Technology, 2012, 27(1): 60-71.

Erki M A, Rizkalla S H. FRP reinforcement for concrete structures. CONCRETE INTERNATIONAL DETROIT, 1993, 15: 48-52.

Franzén T. Shotcrete for underground support: a state-of-the-art report with focus on steel-fibre reinforcement. Tunnelling and Underground Space Technology, 1992, 7(4): 383-391.

Hensher D A. Fiber-reinforced-plastic (FRP) reinforcement for concrete structures: properties and applications. Elsevier, 2013.

Hikima K, Koketsu K. Rupture processes of the 2004 Chuetsu (mid‐Niigata prefecture) earthquake, Japan: A series of events in a complex fault system. Geophysical research letters, 2005, 32(18).

Itasca Consulting Group, Inc. (2002) FLAC3D User's manual.

Jeng F, Lin M L, Yuan S C. Performance of toughness indices for steel fiber reinforced shotcrete. Tunnelling and underground space technology, 2002, 17(1): 69-82.

Jiang Y J, Xiao J, Tanabashi Y, Mizokami T. Development of an automated servo-controlled direct shear apparatus applying a constant normal stiffness condition. International Journal of Rock Mechanics and Mining Sciences, 2004, 41(2): 275-286.

Jiang Y J, Tanabashi Y, Li B, Esaki T. Influence of geometrical distribution of rock joints

on deformational behavior of underground opening. Tunnelling and underground space technology, 2006, 21(5): 485-491.

Kiriyama K, Kakizaki M, Takabayashi T, Hirosawa N. Structure and construction examples of tunnel reinforcement method using thin steel panels. Nippon Steel Technical Report, 2005: 45-50.

Kontogianni V A, Stiros S C. Earthquakes and seismic faulting: effects on tunnels. Turkish Journal of Earth Sciences, 2003, 12(1): 153-156.

Lam L, Teng J G, Cheung C H, XIAO Y. FRP-confined concrete under axial cyclic compression. Cement and Concrete composites, 2006, 28(10): 949-958.

Lee J K, Lee J H. Nondestructive evaluation on damage of carbon fiber sheet reinforced concrete. Composite structures, 2002, 58(1): 139-147.

Mamalis A G, Manolakos D E, Ioannidis M B, Papapostolou D P. The static and dynamic axial collapse of CFRP square tubes: finite element modelling. Composite structures, 2006, 74(2): 213-225.

Miyauchi K. Estimation of strengthening effects with carbon fiber sheet for concrete column. Proceedings of the 3rd International Symposium on Non-Metallic (FRP) Reinforcement for Concrete Structures, 1997: 217-224.

O'Rourke T D, Goh S H, Menkiti C O, Mair R J. Highway Tunnel Performance during the 1999 Duzce Earthquake. Proc. of 15th International Conf on Soil Mechanics and Geotechnical Eng., 2001: 1365-1368.

Sheikh SA, Yau G. Seismic behavior of concrete columns confined with steel and fiber-reinforced polymers. ACI Structural Journal, 2002, 99(1): 72-80.

Structure and Planning Institute of Japan. User manual of the seismic response analysis program for stratified soil layers: *k*-SHAKE. Tokyo, Japan, 2005a.

Suzuki T. Damages of urban tunnels due to the Southern Hyogo Earthquake of January 17, 1995 and the evaluation of seismic isolation effect. CD-ROM of the 11WCEE, Acapulco, Mexico, 1996.

The Ministry of Public Works Research Institute Tunnel Laboratory, Document: Prediction and measures manuals of ground deformation for tunnel excavation (plan), 1994. (in Japanese)

Toyabe S, Shioiri T, Kuwabara H, Endoh T, Tanabe N, Someya T, Akazawa K. Impaired psychological recovery in the elderly after the Niigata-Chuetsu Earthquake in Japan: A population-based study. BMC Public Health 2006; 6:230

Wang J N, Munfakh G A. Seismic design of tunnels. WIT Transactions on the Built Environment, 2001: 57.

Wang H B, Sassa K, Xu W Y. Analysis of a spatial distribution of landslides triggered by the 2004 Chuetsu earthquakes of Niigata Prefecture, Japan. Natural Hazards, 2007, 41(1): 43-60.

Yashiro K, Kojima Y, Shimizu M. Historical earthquake damage to tunnels in Japan and

case studies of railway tunnels in the 2004 Niigataken-Chuetsu earthquake. Quarterly Report of RTRI, 2007, 48(3): 136-141.

Yoshida N. Ungerground and Buried Structure, Earthquake Geotechnical Engineering. Proc. of 2nd International Conf on Earthquake Geotechnical Eng., 1999: 987-992.

Zhu Z, Ahmad I, Mirmiran A. Seismic performance of concrete-filled FRP tube columns for bridge substructure. Journal of Bridge Engineering, 2006, 11(3): 359-370.

Zou X K, Teng J G, De Lorenzis L, Xia S H. Optimal performance-based design of FRP jackets for seismic retrofit of reinforced concrete frames. Composites Part B: Engineering, 2007, 38(5): 584-597.

CHAPTER 7

Conclusions and future researches

7.1 Conclusions and discussions

In the present study, the deformation behaviors of rocks around underground structures and the corresponding control methods in complex geological conditions were discussed. In the first part of this thesis (Chapter 3 to 4), experimental and numerical sturdies were carried out to investigate the cracking process and squeezing deformation of rocks or rock-like materials, aiming to improve the understanding of mechanical and deformation behaviors of jointed soft rock masses. In the second part of this thesis (Chapter 5 to 6), a series of model test and numerical simulations were performed to investigate the reinforcing effects of PFC-PCM method on tunnel lining, taking into accounts the degradation of lining concrete, seismic load. The main results of this thesis are summarized in this chapter.

(1) Researches on the deformation behaviors of underground structures in excavation

The main propagation direction of newly generated cracks are approximately perpendicular to the joint dip angles. For the brittle rock with a low joint dip angle (α = 30°), the failure of host rock masses is given rise to the flexing and creaking of layer blocks, and the deformation and failure around the underground openings are generally governed by the tensile strength of host rock masses. Besides, for a moderate (α = 45°) or high joint dip angle (α = 60°), sliding of rock masses also plays an important role on the deformation of rock masses. (2) The remote cracks are initiated at a certain distance of 1.5 – 2.0 D from the edge of underground opening with a low (α = 30°) or moderate (α = 45°) joint dip angle, where D is the diameter of circular underground opening. When a joint angle of 60° is exceeded, no remote crack could be observed around the underground opening. The maximum displacement at the left shoulder of tunnel is almost 1.8 - 2 times of the minimum displacement at the right side wall of underground opening. (3) When the joint spacing is equal to or larger than 0.5 times of diameter of circular opening, the deformation around the underground openings is negligibly small. (4) The influence of opening shapes on the main propagation direction of newly generated cracks could be negligible. Compared with the circular/horseshoe opening, a larger area of tensile failure zones are observed around the square opening due to the existence of sharp corners. For a moderate joint dip angle, the displacement around the square opening is remarkable due to the stress concentration at the sharp corners and

the overlay of tensile and slipping failures. (5) The main propagation direction of newly generated cracks is influenced by the tensile strength of rock-like materials. For a low (α = 30°) or moderate joint dip angle (α = 45°), the obtuse angle between the main propagation direction of newly generated cracks and the horizontal decreases with the increment of tensile strength. While for a high joint dip angle (α = 60°), the effects of tensile strength on the main propagation direction of newly generated cracks could be negligible.

The case study and detailed numerical analysis of the WS of the Tawarazaka Tunnel presented in this paper clearly show how geological conditions such as the initial horizontal stress ratio, bedding joint stiffness, bedding joint internal friction angle, rock modulus and overburden depth impact ground squeezing. On-site investigation results of 296 tunnel profiles in the WS of the Tawarazaka Tunnel were compared to those in the ES and NF, which totaled 1861 tunnel profiles. Moreover, two-dimensional numerical analysis using the originally developed FEM code was performed to investigate the main factors that influence ground squeezing in the WS of the Tawarazaka Tunnel, and the following conclusions were drawn.

Ground squeezing is prone to occur in geologic units with Paleogene mudstones. λ varied from 2 to 10 in the WS due to the deformability of mudstone and from 1 to 5 for tunnels in the NF and ES. A detailed study of the convergence data revealed that ground squeezing was related to the initial horizontal stress ratio K_0, and a larger K_0 led to a greater value of λ. Ground squeezing could be affected by poor ground conditions, such as mudstone with strongly developed slickensides.

The numerical results showed that a larger value of K_0 led to a greater convergence ratio λ, which was consistent with the measured results obtained from the Paleogene and Neogene formations. Ground squeezing was mainly affected by the modulus values of rocks nearby, and the existence of bedding joints had a negligible impact on ground squeezing. Overburden in the WS can be utilized as a reliable basis to alert engineers to implement mitigation measures during tunneling. The convergence values increased with increasing H, and the convergence ratio λ was generally stable after the critical overburden depth of 100 m was exceeded.

(2) Researches on the deformation behaviors of underground structures in operation

First, a series of direct shear tests were conducted on PCM-concrete specimens embedded with an FRP layer with different grades, and fundamental mechanical properties of FRP-PCM reinforcement, such as shear stiffness, cohesion, and friction angle were obtained, which were later used in numerical simulations. Then, bending tests were conducted on concrete beams reinforced by FRP-PCM method to directly investigate its reinforcing effects on concrete structures. Finally, numerical simulations

on degraded tunnels undergone loosening pressure were implemented, and applicable condition of FRP-PCM method to tunnels with different health degree, ground class, loosening pressure, and concrete strength was investigated. The performance of different grades of FRP grids was confirmed through the comparison of their direct shear test results, which showed that greater shear strength of FRP-PCM reinforcement could be achieved by using a higher grade of FRP grid. The bearing capacity of concrete beams reinforced with FRP grids (CR6) obtained from bending test was improved by around 40% comparing to the unreinforced beam. These experiments have revealed that the FRP-PCM method has good performance in reinforcing the concrete structures. In the numerical model of tunnels, the existence of cavity above crown was considered which could exert an external loosening pressure originating from the weight of rock mass above the cavity to the tunnel lining. This is one of the commonly observed unfavorable conditions for aged tunnels in Japan constructed by fore-piling method. Simulation results showed that the FRP-PCM method could efficiently reduce the axial stress acting on tunnel lining, and such effect is greater for tunnel linings with larger deterioration degree. Degraded tunnel linings were classified into three health degrees, and reinforcement is required when the increased compressive stress acting on tunnel lining due to the effect of external unfavorable conditions exceeds some critical values. Following this line, applicable conditions for FRP-PCM method taking into account the combinations of different internal (e.g., strength of concrete) and external conditions (e.g., loosening pressure) were proposed, which could help select the most effective type of FRP-PCM reinforcement according to the actual conditions of tunnel linings concerned. Other unfavorable conditions beyond the loosening pressure will be considered in the future exploration of the performance of FRP-PCM reinforcement.

Numerical simulations under seismic load based on the FDM method were performed, taking into accounts the cavity positions (cavity on the crown and shoulder), the construction methods (FM and NATM) and types of ground class (CI and CII). The lining concrete in rock class type of CI showed no damage during the seismic analysis. For tunnels in rock class type of CII, the plastic failure zones almost occurred on the shoulder of tunnel linings, especially for tunnels constructed by FM. A good reinforcement performance was observed for the cases reinforced with CR8 grids. For the case with cavity on the shoulder of tunnel, the failure zones in the inner surface of lining were greatly improved. Better reinforcing effects were obtained in the case of cavity on the shoulder of tunnel, comparing with the one on the crown. The axial stress on tunnels that constructed by FM was greater than those by NATM, and the axial stress acting on tunnel linings was greatly decreased with FRP-PCM method. Although tunnels constructed in NATM showed a better bearing capacity comparing with the one in FM, a greater reinforcing effect was obtained for tunnels in NATM.

7.2 Future researches

The recent cooperative researches about the stability and deformation control measures of underground structures in complex geological conditions will be continued in the future two years researches. At present, most of former studies are focused on the deformation mechanisms of tunnels in sand or clay formations after excavation under seismic load by the centrifuge tests. However, the deformation and failure mechanisms of underground structures in soft rocks are not clear enough, especially when a fault or bedding joints are encountered. In the future, a series of dynamic centrifuge tests and their corresponding numerical analysis will be conducted to investigate the deformation and failure mechanisms of underground structures in soft jointed rocks, regarding the effects of input motion amplitude, frequency and duration on the seismic behavior with different underground shapes.